CHARACTERIZATION OF FUNDAMENTAL AND RETICULATED BIOMEDICAL POLYMER STRUCTURES FABRICATED BY THREE DIMENSIONAL PRINTING

by

SCOTT W. BORLAND

B.S. Materials Science and Engineering, University of Arizona (1992)

Submitted to the Department of Chemical Engineering in
Partial Fulfillment of the Requirements for the Degree of

MASTER OF SCIENCE

in Chemical Engineering
at the

Massachusetts Institute of Technology

June 1995

Signature of Author _____
Department of Chemical Engineering
March 17, 1995

Certified by _____
Linda Griffith Cima
Karl Van Tassel Assistant Professor of Chemical Engineering
Thesis Supervisor

Accepted by _____
Robert E. Cohen
Chairman, Committee for Graduate Students

CHARACTERIZATION OF FUNDAMENTAL AND RETICULATED BIOMEDICAL POLYMER STRUCTURES FABRICATED BY THREE DIMENSIONAL PRINTING

by

SCOTT W. BORLAND

Submitted to the Department of Chemical Engineering
on March 17, 1995 in partial fulfillment of the requirements
for the Degree of Master of Science in Chemical Engineering

ABSTRACT

Matrix device fabrication plays a crucial role in tissue engineering. Typical processes for constructing these polymeric matrices do not allow for sufficient control over device structure. However, solid free-form fabrication techniques are quite amenable to fabrication of very intricate and complex structures. The most flexible and versatile of these techniques, Three Dimensional Printing, has been successfully applied to a wide variety of materials, geometries, and applications. This process had never been used in processing polymeric materials prior to this study.

Biodegradable polyesters often used in tissue engineering applications were used to fabricate primitive features and determine the important issues in polymeric 3D Printing. A new powder bonding mechanism in which the polymer particles composing the powder bed were at least partially dissolved by a solvent binder component and then recast as solid structure was examined. A theoretical equation describing the anticipated feature size of single line polymer primitives was developed. This theoretical description was used to determine the processes dominating feature formation behavior. Basic three dimensional devices were fabricated. The desired structural control needed for tissue engineering applications was successfully demonstrated.

Many factors affect the structure of features fabricated by this process as with other 3D Printing applications,. The binder per unit line length, powder bed density and composition, binder composition, binder saturation, and final line density all significantly impact the feature size. Binder evaporation also plays a critical role in fabrication of 3D objects.

Thesis Supervisor: Linda G. Cima

Title: Karl Van Tassel Assistant Professor of Chemical Engineering

ACKNOWLEDGMENTS

I would like to thank my advisor, Professor Linda Cima, for her guidance and advice during my time at MIT, without which this document, and the work associated with it, would not have been possible.

I would also like to extend my gratitude to Professor Michael Cima for his advice, suggestions, and ideas.

All members of the 3D Printing group deserve thanks, as they've all contributed in one way or another. In particular, I'd like to extend thanks to Jim Bredt his help in the early days and to Satbir Khanuja for lots of "warped" discussions.

Without a doubt, this work would not be a complete story without the contributions of Ben Wu. Thanks for all your help, support, pictures, and data!

My office/lab mates made life here a little better every day. Without Mark Powers, Stephanie Lopina, Ann Park, Phil Kuhl, Sue Hobbs, and Jeff Sperinde around to provide their listening ears, the great lunch company, and moral support, I'm not sure this would have gotten done. Thanks.

I'd like to thank all of the other people of the CPRL lab. It was nice to know there were some other people who read the sports section around here.

Thanks to all the people who've patiently shared the computer room with. In particular, thanks to Eric Scharin. Without his expertise, it would have been impossible to make these pages reflect the work behind them.

Thanks to John Centorino and Lenny Rigione for making everything work all the time.

To my niece Allison and her mom and dad, thanks for constantly reminding me of what is really important.

To my mom, thanks for letting me know when Saturday rolls around. Thanks for always being there.

To my dad, I hope I've made you proud.

And to Lisa, I passionately dedicate this thing to you. Thanks for putting up with all the time and crap in general that it took to do this. You turn my nightmares into fairy tales, and, like I've said for a long time, you make me happy when skies are gray. Your support, attention, and love have always kept me going. I look forward to doing the same for you in the future. You are the mostest bestest.

CONTENTS

LIST OF FIGURES

LIST OF TABLES

1. INTRODUCTION

Tissue Regeneration and Matrix Devices

Tissue regeneration can be achieved by cell transplantation from an outside source and/or by cell migration from neighboring tissues. In cell transplantation, a small number of donor cells is harvested from healthy tissue, cultured and grown in vitro, and then reimplanted. This therapy is often autographic (self-donor). Thus, problems such as tissue rejection and disease transmission associated with allografts and xenografts (non-self cell sources) are avoided. In cell migration approaches, cells migrate from the surrounding healthy tissue into the defect region in order to regenerate the desired tissue. Cells require a temporary matrix substrate in both approaches that guides the three dimensional organization and growth of the tissue. This matrix substrate or device must inherently be porous in order to provide space for cells to adhere, migrate, and proliferate.

Tissues exhibit several levels of organization and devices for tissue regeneration must likewise contain structural features on several scales. The first level of structure is the overall macroscopic three dimensional shape of the device, which may be up to several centimeters in size. The precise shape of a device may directly affect the success or failure of the application, as demonstrated in previous efforts to regenerate human ear cartilage[1]. In those studies, the cartilage was successfully regenerated, but the macroscopic shape of the "ear" only roughly resembled the structure desired. The second level of structure is the placement and orientation of channels within the device. Channels a few hundred microns in size would provide a direct, non-tortuous path for cell migration from outside and within the device. Finally, the most basic structural level is interconnected microporosity within the device, involving a feature size up to a few tens of microns. Such microporosity would provide a large surface area to allow for the

formation of an interconnected three dimensional cell-extracellular matrix tissue. Thus, an ideal tissue matrix device would be characterized by a complex reticulated structure that would reflect these multiple levels of structure.

A major challenge in tissue engineering is fabrication of such complex devices with control over all levels of structure. No approach has yet been developed which offer precise control over the structure over several scales. Control over one or two individual structural levels has been demonstrated. Solvent casting-particulate leaching techniques and fiber meshes and fabrics have been used to achieve interconnected microporosity in a device[1,2]. Although the average pore size can be controlled, the size and shape of individual pores can not. Attempts to combine microporosity with a controlled complex three dimensional shape have been less successful. For example, the molding of fibers and fabrics and the lamination of a series of carved contour layers have resulted in three dimensional shapes which do not duplicate the desired model[3,4]. In addition, no one has investigated the effect on tissue regeneration of having precisely oriented voids or channels within a three dimensional matrix device, due to fabrication limitations.

A wide variety of biomedical materials might be considered in fabricating tissue matrix devices. While numerous possible natural and synthetic polymers (see Table 1.1) are commonly used in biomedical applications[5], the polyester family of is particularly attractive. Poly(lactic acid (PLA), polyglycolic acid (PGA), and their copolymers, have been extensively used as implantable materials[6,7,8]. They are widely used as sutures, fracture fixation devices, and controlled drug delivery formulations. This family of materials has a range of mechanical properties, depending on the exact material composition.

Implantation of synthetic engineered devices can cause a destructive long term immune response to the implanted materials. This reaction may be mitigated if the non-biological components of the matrix are removed once the tissue is

deemed to be viable. However, extraction of the device may be complex and difficult, particularly if it has lost structural integrity. Device biodegradability is a viable alternative to extraction, particularly if the degradation products are native to the body or are very efficiently excreted from the body. The synthetic materials are removed from the body once they have performed their function in this approach. In addition, the degrading synthetic device gradually exposes the growing tissue to more stress until the device completely degrades and the tissue bears all the forces.

The polyester polymers are also attractive in that they readily degrade in physiological conditions. PLA (structure shown in Figure 1.1) degrades by hydrolysis to lactic acid, which is a natural metabolite of the body. The time scale for degradation of this material ranges from several weeks to a few months, depending on the specific properties of the material. Because of the high cost of PLA ($1000 per kilogram and higher), another biodegradable polyester, polycaprolactone (PCL), was selected as a model material. PCL is similar to PLA in structure, as shown in Figure 1.2 and is also used as a medical material. Degradation of PCL occurs by hydrolysis and by enzymatic mechanisms. The time scale of degradation of PCL is on the order of months to years.

Table 1.1 Polymers typically used in biomedical applications[5]

Poly(lactic acid)	Poly(amino acids)
Poly(glycolic acid)	Poly(ethylene oxide)
Poly(orthoesters)	Poly(ethylene terephthalate)
Poly(anhydrides)	Poly(phosphagene)
Poly(hydroxybutyrate)	Nylon
Poly(ester imides)	Polyurethanes
Poly(cyanoacrylates)	Collagen
Poly(methyl methacrylate)	Poly(dimethyl siloxane)
Poly(hydroxyethyl methacrylate)	

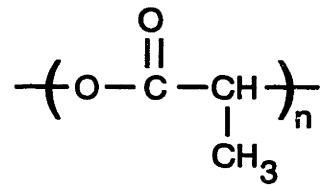

Figure 1.1 Structure of Poly(Lactic Acid) (PLA)

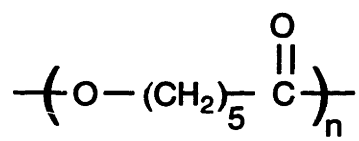

Figure 1.2 Structure of Polycaprolactone (PCL)

Other materials may be included in tissue regeneration devices. For example, bone material may be incorporated for bone regeneration applications. Such structures can be fabricated by placing powdered bone in the powder bed

with the polymeric materials. Leachable components may also be incorporated in tissue matrix devices. Microstructure in the devices can be created by initially including water-soluble components in the structure of a device and then later removing these materials by leaching in water, as in solvent casting/particulate leaching processes described earlier. While the viability of all of these materials for tissue engineering applications has been demonstrated, much untapped potential exists in the field of device construction and processing.

Solid Free-form Fabrication

A group of processing techniques has been developed for building very complex structures which may be applicable to fabricating tissue matrix devices from biodegradable polymers. These techniques, collectively known as solid free-form fabrication (SFF) techniques, are rapid prototyping processing methods that are amenable to the construction of highly complex three dimensional objects. High degrees of complexity are obtainable due to two fundamental characteristics of these techniques: construction by a laminated building process involving sequential stacking of thin, nearly two dimensional slices and use of computer-aided design (CAD) representations of the desired objects guide construction of the complex shapes[9,10]. These attributes simplify the fabrication task. Reduction of the object to be constructed into "2D" layers simplifies the structure of even highly complex 3D objects. The CAD representation is a blueprint of the structure to be constructed and, as such, allows for precise control of fabrication throughout the device, as well as within each of these "2D" layers.

The most common of the SFF techniques are Stereolithography (SLA), Selective Laser Sintering (SLS), Ballistic Particle Manufacturing (BPM), and Three Dimensional Printing (3DP). These technologies are detailed elsewhere[11]. While

all of the SFF techniques have common fundamental characteristics, they represent a diverse set of fabrication techniques. Each is amenable to specific applications involving specific materials. For example, the SLA process involves polymerizing liquid photopolymers using a UV laser. The SLS process uses a CO_2 laser to selectively sinter powdered material. The BPM technique uses liquidized wax to print on to a movable solid substrate. Three Dimensional Printing employs a binder material that is printed into a powder bed, sticking the powder particles together in order to form a solid object. While originally developed for constructing ceramic casting molds, 3D Printing is perhaps the most flexible of all the SFF techniques and, therefore, the most amenable for development as a method for processing biomedical polymers. Almost any material can be processed by the 3D Printing approach because the only requirement is that the primary material be in the form of a powder and virtually all materials can be processed to such a form. In addition, almost any geometry can be fabricated using Three Dimensional Printing.

Based on the tremendous flexibility afforded by 3D Printing for fabricating three dimensional objects with complex geometries, this process was selected for constructing tissue regeneration devices. Three Dimensional Printing has previously been used only with ceramic and metal materials. In this work, 3D Printing was tailored for polymeric applications, with the selection of appropriate powders, binder materials, and printing parameters. This thesis discusses the development of 3D Printing for processing polymeric materials, characterization of printed structures, and fabrication of prototype devices for tissue regeneration.

2. BACKGROUND

Three Dimensional Printing

Like other SFF techniques, the 3D Printing fabrication process constructs objects by sequentially building thin "2D" layers on top of one another[12,13,14]. A CAD picture or other 3D model of the defect, object, or device to be constructed is necessary. This model is then sliced into a stack of thin layers as shown in Figure 2.1. The information about the structure of each layer contained in this sliced model can then be delivered to the 3D Printing machine in the appropriate sequence.

The key elements of the 3D Printing machine, shown in cross-section in Figure 2.2, are the piston, the powder bed, the powder spreader, and a printhead mounted on an X-Y positioning system. The piston supports a plate which forms the base of the powder bed. This piston can be moved vertically in small increments (typically 150 μm). The piston and the four walls around it define the powder bed. Each layer of powder in the bed is spread using the powder spreader, a cylindrical rod that is mounted on the top of the powder bed. Loose powder is piled in front of the rod and then spread across the bed as the spreader rod moves across the piston. The printhead and the X-Y positioning system are mounted over the powder bed to allow printing to take place. The printhead is connected to and controlled by a computer using the CAD structural information. Not shown in Figure 2.2 is the system for delivery of binder to the printhead. The printhead is directly connected to a binder reservoir. Pressurized nitrogen gas forces the binder to flow from the reservoir to the printhead.

The 3D Printing process consists of a set of repeated steps (Figure 2.3). A layer of powder is spread over the powder bed using the powder spreader. The individual 2D layers are constructed by passing the printhead over the bed of

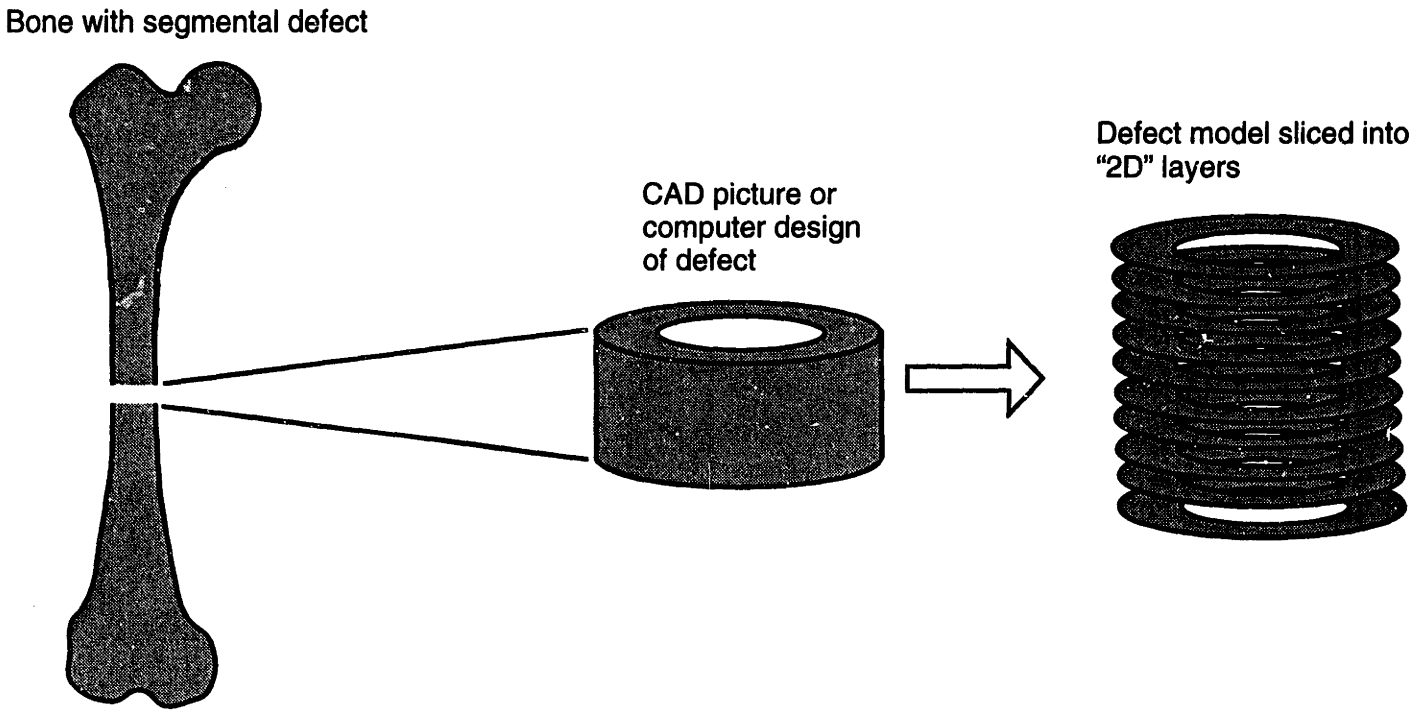

Figure 2.1 Slicing of Device model into "2D" layers

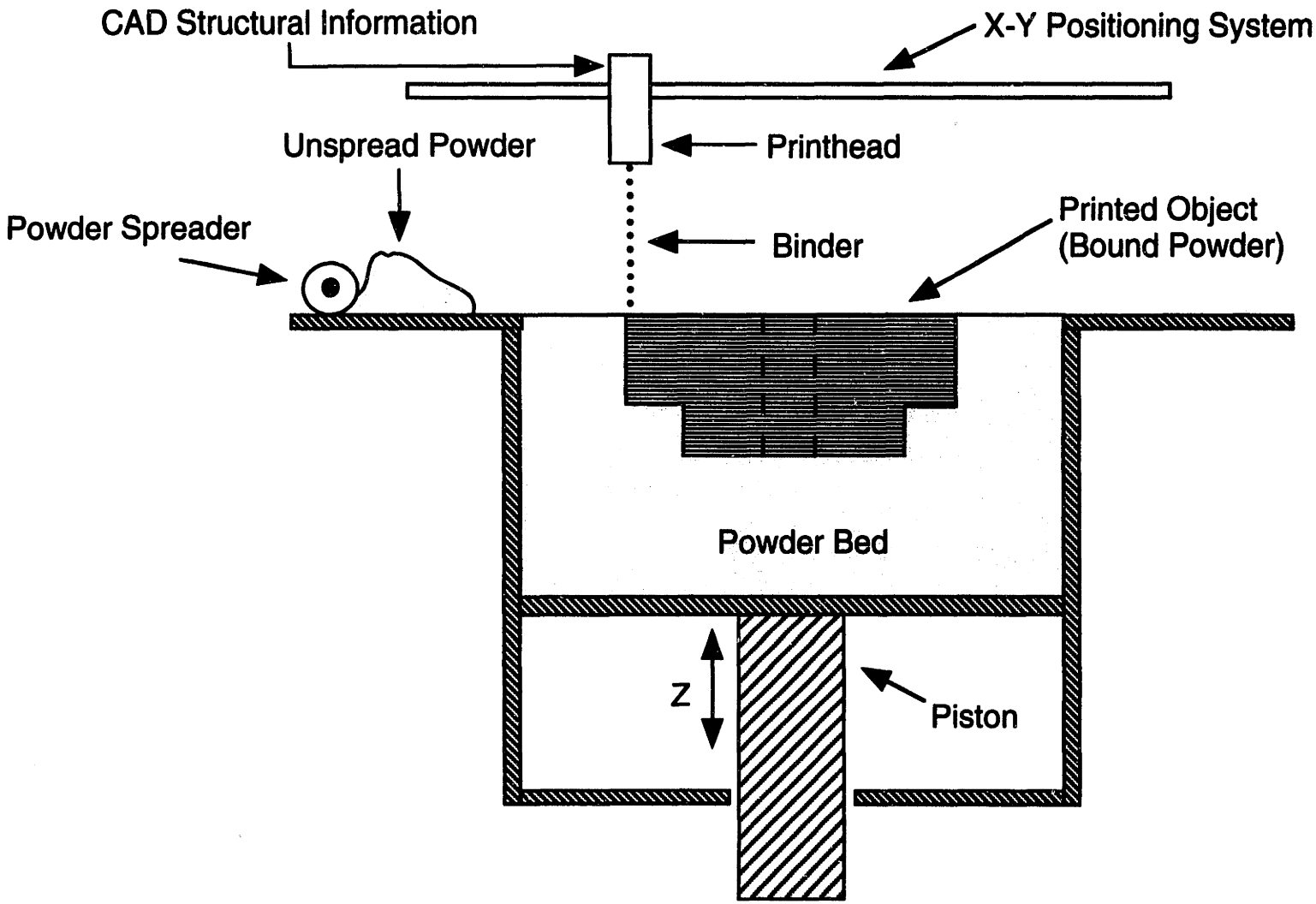

Figure 2.2 Key elements of a 3D Printing machine (in cross section)

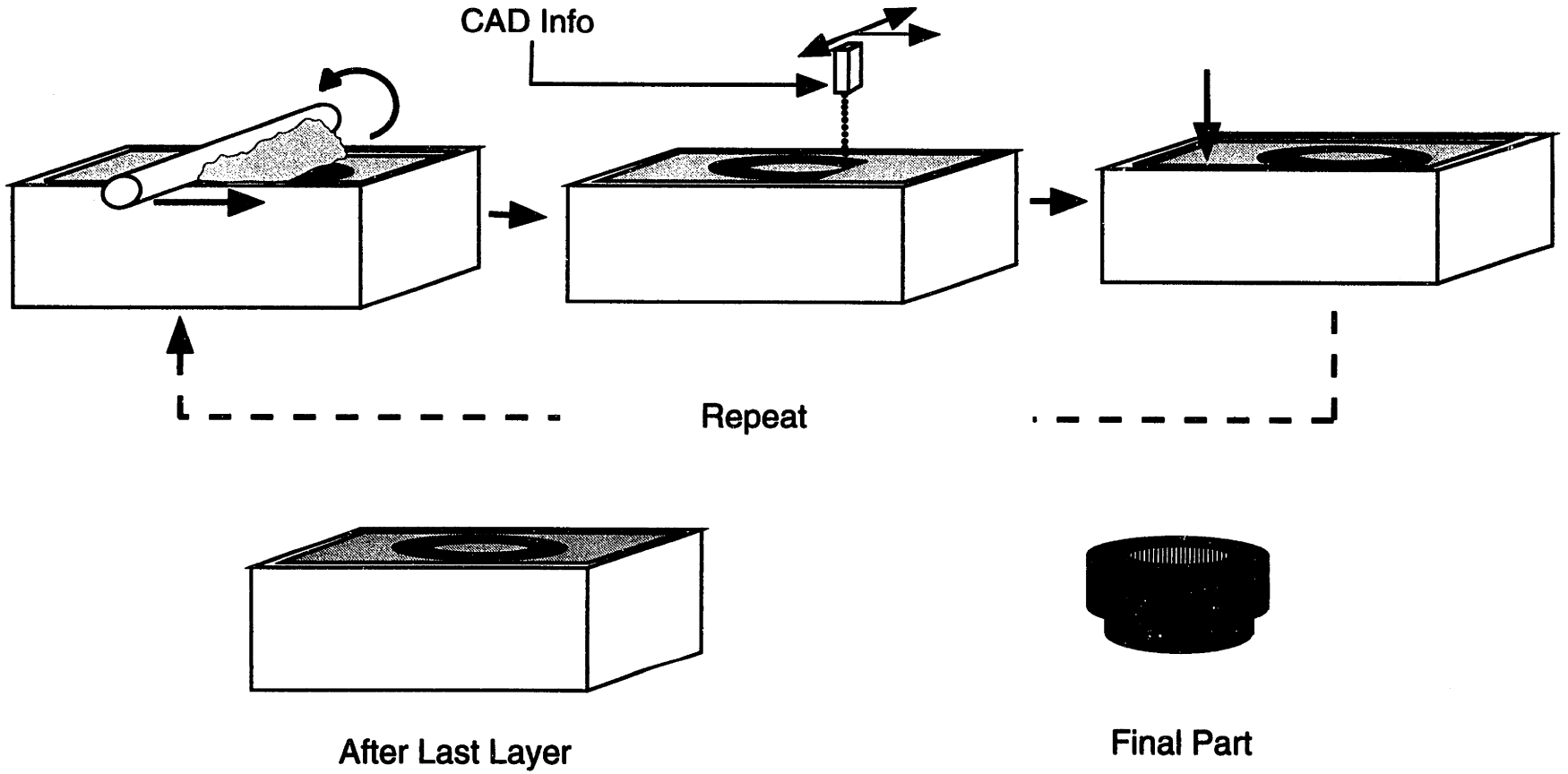

Figure 2.3 The 3D Printing process

powder material. This printhead delivers a "jet" of binder to the powder bed wherever solid structure, as indicated by the sliced CAD model, is desired in the final device. The binder acts as a "glue" and sticks the powder together wherever the jet impacts the powder bed,. Conversely, where the binder is not delivered, the powder is not glued together. Once a given layer is printed, the piston is lowered and the process is repeated until the final layer of the device is completed. The unbound powder may be removed, leaving solid material wherever the binder was delivered after some post-processing, such as drying or heat treatment,.

Printing Methods

The 3D Printing machine must move the printhead over the entire surface of the powder bed via the X-Y positioning system. Two distinct approaches to achieving this movement are possible: raster printing and vector printing. In raster printing, the speed of travel along the two directions of the bed are very different. The printhead moves very quickly across the entire length of the bed in the "fast" direction (call this the X direction). Next, the printhead moves a small step in the perpendicular direction (the "slow" or Y direction). Then the printhead then moves back across the entire length of the powder bed in the (negative) X direction, takes another small step in the Y direction, and repeats this process across the entire powder bed. In this case, changes in direction, starts, and stops occur beyond the printing area, so the uniform printing is produced. Most common office computer printers operate in this fashion.

In contrast, the printhead speed in vector printing is comparable for both the X and Y directions over the powder bed. The printhead is moved to any location on the powder bed to print a specific structure. An entire contiguous structure is fabricated before moving on to the next structure, regardless of the proximity of the latter. In this case, changes in direction, starts, and stops may

occur over the powder bed, which increases the complexity of maintaining control of binder delivery. Many common computer plotters operate in this mode.

Printing in vector fashion can speed the printing process in some cases. For example, a line to be printed perpendicular to the X axis could be done in a single movement in vector printing. In raster printing, the line would be assembled from several segments the length of the small Y step and the printhead would have to travel across the entire powder bed. Nonetheless, printing in raster form can be very fast for many applications if the fast axis printhead speed is very fast. This mode of printing does not require the high accelerations necessary in vector printing to assure uniform delivery of the printed material. In addition, raster printing can also easily employ multiple jet or printhead printing, which dramatically increases the print rate.

Two types of printhead delivery methods can be implemented in 3D Printing. In continuous jet printing, the binder jet runs continuously. The jet may be turned "off" where no binder is desired by deflecting the continuous binder stream to a catcher, which prevents it from hitting the powder bed. Such drops are discarded or recirculated. A key step in this process is the generation of individual binder drops. The binder stream is acoustically broken into drops using piezoelectric devices. This insures that drops are uniform in size with no associated "satellite" drops. In addition, drop formation can then be synchronized with the charging voltage, so the timing of individual drop formation is known. The binder jet is deflected by selectively charging the drops and passing them through an oriented electric field.

Another approach to printhead operation is drop-on-demand (DOD) printing. In this case, binder drops are generated only when needed. As a result, the printhead only forms and delivers binder drops in the "on" sections of the powder bed and forms no drops in the "off" sections. Less binder is needed for this type of printing, since drops are only formed when necessary and none are

discarded or recirculated. The DOD drops have a lower velocity than continuous jet drops, so disruption of the printing surface (in this work, the powder bed) by those drops is much less significant. However, DOD methods operate at much slower rates (~10 kHz) than continuous jet methods (60-80 kHz).

Binding Mechanism

Previous work in 3D Printing involved printing onto ceramic or metal powders. In all of these systems, a temporary structure is formed by the binder to hold the powder particles in place until some further processing can be done. This temporary structure is typically formed in the powder bed by gelation of the binder upon contacting the powder particles. As a result, no change in the size or shape of the powder particles is produced by the activity of delivering binder with the 3D Printing machine. Instead, the powder particles are merely held in a particular location. The solid structure is formed in a post-processing step (typically a sintering process) in which the powder particles are permanently fused together and the temporary structure is burned away or otherwise removed. While this approach has been very effective for several metal and ceramic materials systems, it relies on post processing to actually form the desired object. In these examples, the 3D Printing aspect of the construction entails only the determination of what material will be included in the final object.

In contrast, polymers are highly amenable to a 3D Printing fabrication approach in which bonding of powder particles during the process of printing is produced by a physical change in the particle structure. Many polymers are readily soluble in common solvents. A solvent-based binder will fully or partially dissolve polymer powder particles. After the solvent portion of the binder evaporates, the particles are effectively "glued" together by recasting of the

dissolved polymer. The resulting solid structure can easily be removed from the powder bed without further processing.

This type of binder-powder interaction in the implementation of 3D Printing with polymeric materials is fundamentally different from other 3D Printing binding systems. The formation of an immediate and permanent bond during the printing process is a novel implementation of the 3D Printing concept. Many biomedical polymers are suitable for use in this type of binder-powder interaction because they are, in many cases, soluble in organic solvents. In these applications, the polymer powder particles are bound together using binders partially or completely composed of common solvents. The resulting solid structure will consist of the polymer material alone following evaporation of the solvent component of the binder.

3. MATERIALS AND METHODS

Materials

The materials involved in the 3D printing process fall into two categories: those in the powder bed and those in the binder. The choice of binders is often dependent on the choice of structural powder materials. For example, in order to explore the novel powder binding mechanism described above, the binder material must dissolve the powder material.

Powder Bed Materials

Since these structural materials are intended to compose a powder bed, obviously they must be obtained in a powder form. Poly(lactic acid) (PLA) and polycaprolactone (PCL) are not commercially available in that form. Such polymers are typically provided in the form of pellets or spheres. For this work, PLA was received from Ethicon in pellet form (width = 3-5 mm) in three different molecular weights: 53,000, 132,000, and 312,000 (lot #'s ELX-XX3, ELX-XX7, and ELZ-XX3). The molecular weight information was supplied by Ethicon. PLA was received in vacuum-sealed cans and was stored in that state until needed. After the polymer was removed from this initial packaging, it was stored in vacuum ovens at all times in order to limit its exposure to moisture.

PCL was received in pellets (width = 1-5 mm) and in spheres (diameter = 1-5 mm) from Polysciences (lot #'s 412038 and 434850, respectively) and in spheres (diameter = 1-5 mm) from Eastech Chemical/Union Carbide (lot #'s 2139 and 2799). Both Polysciences lots had molecular weights of 23,000, according to GPC. For the Eastech Chemical lots, GPC indicated a molecular weight of 68,000. PCL was stored in plastic bottles in the lab before and after milling.

Mineralized bone material was incorporated into some devices. Bovine bone was used as a model for this bone material given its availability and ease of use. Cortical bone (primarily mid-femur) samples were obtained from a local grocer. Laboratory grade sodium chloride (NaCl) obtained from Fisher Scientific was used as a leachable entity in several experiments.

Powder Preparation

Due to the lack of commercial availability of these polymers in powder form, it was necessary to mill them into the desired powders. Cryogenic processing is necessary for milling polymers with low glass transition temperatures (T_g). The T_g of PCL is -62°C. While the T_g of PLA is higher (60°C), it is still low enough to flow with little heating, so cryogenic processing is also useful for that polymer. Powders were classified using sieve screens and a sieve shaker (Fisher Wheeler). Screens with mesh sizes 100, 200, 325, and 635 (opening size 150, 75, 45, and 20 μm, respectively) were used. Several batches of polymer (100-200 g) were combined and shaken for 30-45 minutes. The PLA materials showed a tendency to stick to the sides and screen, while the PCL did not.

PCL was initially milled with a blender mill (Waring). The spheres or pellets were frozen in liquid nitrogen (LN) for at least 30 minutes prior to milling. In addition, enough LN was added to the blender container to completely submerge the polymer. Additional LN was added during milling. The blender was run for up to 4 minutes with each batch, which consisted of about 50 grams of polymer. After milling, the powder was removed from the blender and placed in a bottle to warm to room temperature to prevent condensation of water onto the polymer surface. (PLA was not milled using this blender due to its high cost. However, in later implementations the PLA bottles were immediately placed in a

vacuum oven in order to prevent hydrolytic degradation of the PLA by condensing water.)

Typical yields from the blender mill of particle sizes less than 150 μm for the PCL pellets were about 6% in the range 75-150 μm, about 4% 45-75 μm and less than 1% less than 45 μm. However, the yields dropped dramatically in milling PCL spheres of a similar molecular weight. Less than 5% of the polymer milled fell in these "useable" ranges (about 2%, 1%, and 0% for the above ranges). PCL was available as pellets only at the outset of this work. All other later sources supplied the polymer in the spherical form. Repeated processing of the large powders (150-1000 μm) was more difficult, as the material would easily fly out of the blender. The yield for the reprocessed powders was lower in all cases than the yields mentioned above.

In order to improve powder yields, an alternative milling process using an Ultra Centrifugal Mill (Glen Mills/Retsch) was developed. A cross-sectional schematic of this mill is shown in Figure 3.1. The functional unit of the mill is a spinning rotor that crushes particles against a screen with a slightly larger diameter than the rotor. The size of the screen opening determines if the material is passed to a collection bin or reprocessed. A range of screen sizes were used: 80 μm, 120 μm, 250 μm, 500 μm, 1000 μm, and 4000 μm. Once again, the polymers were frozen in LN for at least 30 minutes prior to milling. In addition, enough LN was added to cover the bottom of the catch pan prior to milling and small amounts of LN were added with the polymer during milling. Despite the presence of LN in the mill and around the material, the milling process generated heat, which the caused the materials to melt and flow. This resulted in the polymers sticking to the screen and rotor. Adding the pellets and spheres very slowly (one at a time) reduced, but did not eliminate, this problem. Nonetheless, higher yields of polymer powder less than 150 μm were achieved. The highest yields (15-20%)

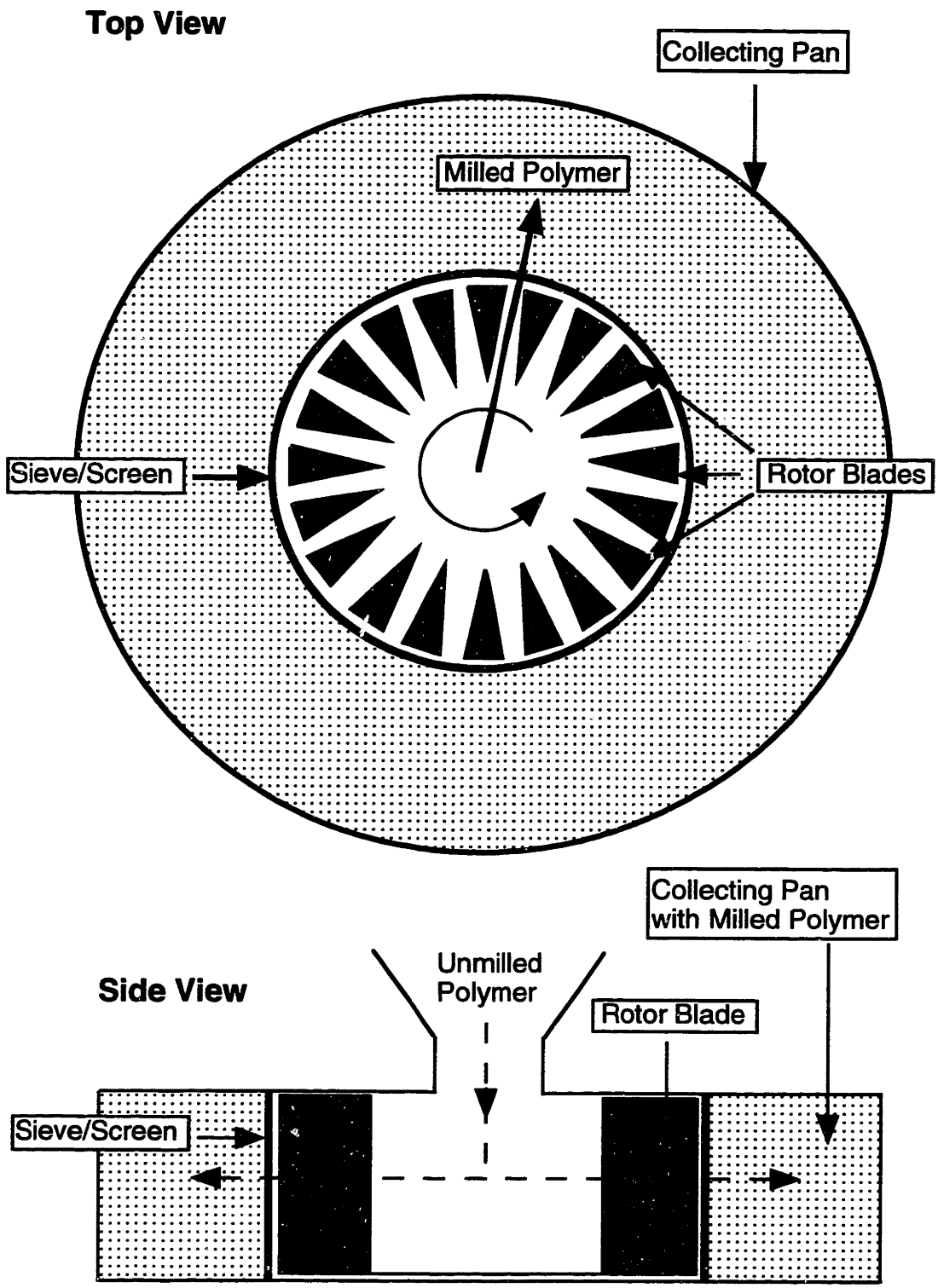

Figure 3.1 Schematic of the Glen Mills Ultra Centrifugal Mill

were achieved in milling PCL in pellet form using a single pass through the 250 μm screen.

Improvements of this process were still necessary, however, since repeated processing of powder greater than 150 μm in size was largely unsuccessful due to the material blowing out the top of the mill and melting/flowing onto the screens and rotor. The mill was modified to allow for the constant delivery of liquid nitrogen directly at the base of the screen and rotor. The LN was delivered through a spritz cone mounted on the inside of the collection pan. Thus, the mill interior could be constantly cooled during the milling process.

The polymers were still frozen in LN for at least 30 minutes prior to milling. In addition, the interior of the mill was pre-chilled with LN for about 3 minutes prior to milling. The constant delivery of LN allowed for faster delivery of the pellets and spheres to the mill and reduced the problems with the polymers sticking to the screen and rotor. In addition, smaller screens could be used on the first pass of the material through the mill.

The mill modification resulted in higher yields of powder in the desirable (less than 150 μm) range. PCL was processed from beads through the 120 μm screen in one pass. After sieving, 14% of the material was less than 45 μm, 32% was between 45 and 75 μm, and 54% was between 75 and 150 μm. PLA was processed from pellets through the 250 μm screen in one pass. After sieving, 5% of the PLA was less than 45 μm, 19% was between 45 and 75 μm, 35% was between 75 and 150 μm, and 42% was between 150 and 250 μm. While it was anticipated that the PLA would be easier to process than PCL given its much higher glass transition temperature, surprisingly, attempts at using the 120 μm screen with the PLA were unsuccessful, as the polymer stuck to the screen very quickly.

Further improvements can be made in the polymer milling process. For example, the impact of the geometry of the starting materials was not explored. The surface area to volume ratio for the starting materials (beads and pellets) is quite low. If that ratio were increased by, for example, casting or melting the polymers into thin sheets, the milling yields might be improved.

Other powder bed materials such as NaCl and bovine bone were easily processed in the Ultra Centrifugal mill. The NaCl was milled through the 80 μm screen in one pass. Liquid nitrogen was not necessary to process the salt. The bovine bone was milled from large chunks to less than 120 μm with two passes using the 4000 μm screen and 120 μm screen. LN was used in conjunction with the bone milling to avoid changing the structure of the bone by heating.

Spreading of all the powders, except the bone powder, was accomplished without significant complications. Occasionally, powder adhered to the spreader rod. This adhesion was dramatically reduced by counter-rotating (rotating in the direction opposite travel across the powder bed) the spreader rod. Press rolling (rotating in the same direction as travel across the bed) resulted in non-uniform powder beds. The counter-rotating approach produced a bed largely uniform in density. The 100% bone powders could not be spread uniformly due to significant cohesion of the powder to itself and the spreader rod. Mixtures of polymer and bone were spreadable, but not as uniformly as polymer alone.

"Tap density" is an approximation of the bed density and is calculated by measuring the weight and volume of powders placed in a graduated cylinder and tapped on the benchtop 5-10 times. Tables 3.1 and 3.2 show the tap densities for many of the powders used in these experiments. Note that these densities are always less than the theoretical solid densities for all materials. In addition, the densities decrease with decreasing powder size. This phenomenon is due to an increasing cohesive sticking with decreasing powder sizes. Thus, rather than

falling into void spaces, smaller powders tend to stick together more than larger ones. This results in a lower density powder bed.

Table 3.1 Tap Densities for structural powder bed polymers

Powder	Tap Density (g/cm^3)
PLA (theoretical solid density = 1.1 g/cm^3)	
ELX-XX7 M_w = 132,000	
< 45 μm	0.25
45-75 μm	0.32
75-150 μm	0.47
ELZ-XX3 M_w = 312,000	
< 45 μm	0.42
45-75 μm	0.47
75-150 μm	0.50
PCL (theoretical solid density = 1.1 g/cm^3)	
434850	
< 45 μm	0.32
45-75 μm	0.34
75-150 μm	0.41
2139	
< 45 μm	0.33
45-75 μm	0.35
75-150 μm	0.46

Table 3.2 Tap Densities for non-polymeric (and polyethylene oxide) powder bed materials

Powder		Tap Density (g/cm^3)
Cadaver Bone		
	< 80 μm	0.79
	125-250 μm	0.97
Bovine Bone		
	< 120 μm	0.59
	< 250 μm	0.83
	< 45 μm	0.32
Sodium Chloride (theoretical solid density = 2.165 g/cm^3)		
	< 75 μm	0.81
	75-150 μm	0.97
Polyethylene Oxide (contains a flowing agent) (theoretical solid density = 1.0 g/cm^3)		
	45-75 μm	0.50
	75-150 μm	0.49

Binders

A means of fabricating polymeric devices is by printing a solvent which at least partially dissolves and then bonds the polymer powder particles together, as described earlier. Among commonly used organic solvents, PLA is soluble to a significant degree only chloroform and methylene chloride. PCL exhibits solubility in a greater number of solvents. Table 3.3 shows a list of some common laboratory solvents, their vapor pressures, and qualitative measures of the solubility of PCL in those solvents. Low vapor pressure solvents might be more useful as binder components since they would tend to remain in the powder bed longer before evaporating. However, these solvents may also be more difficult to completely remove from the device because they have to be removed by extraction or vacuum drying. In addition, high solubility of the polymer in the solvent might be advantageous in achieving more complete dissolution of the powder particles.

Binders can either be one of these solvents or a polymer-solvent solution. Analytical reagent grade methylene chloride and chloroform (Mallinckrodt) were chosen as binder solvents based on their shared ability to dissolve PCL and PLA. The polymeric components of the polymer solution binders were those materials used as powder bed materials. In addition, an acid-modified form of PCL (proprietary structure) received from Eastech Chemical/Union Carbide with a molecular weight of 10,000 (determined by GPC) was used to prepare some solutions with a high polymeric content.

The binders were prepared by dissolving 0-15 weight percent (wt%) of the "powder bed" polymers in the solvents for 2-24 hours. Acid-modified PCL was also used in binder solutions containing 0-30 wt % polymer. Polymeric solutions with viscosity greater than 70 cP were difficult to jet through the printhead. See Table 3.4 for sample binder viscosity data.

Table 3.3 Vapor pressures and PCL solubilities of potential binder solvents

Solvent	Vapor Pressure (mm Hg at 25°C)	Solubility (of PCL)
methylene chloride	400	Very High
acetone	229	Low
chloroform	199	High
tetradyrofuran	176	Low
benzene	100	High
methyl ethyl ketone	100	Low
ethyl acetate	100	Low
carbon tetrachloride	91	High
toluene	30	Low
cyclohexanone	5	Low
dimethylformamide	3 (at 20°C)	Low
dimethyl sulfoxide	0.4 (at 20°C)	None

Table 3.4 Viscosities for solvent and polymeric solution binders

Binder	Polymer Molecular Weight	Binder Viscosity(cP)
100 % Chloroform ($CHCl_3$)	-	0.58
5 wt% PCL in $CHCl_3$	23,000	3
10 wt% PCL in $CHCl_3$	23,000	15
15 wt% PCL in $CHCl_3$	23,000	63
30 wt% acid-modified PCL in $CHCl_3$	9000	42

Methods

3D Printing Machines

The use of organic solvents as binders necessitates venting of the 3D Printing machine in a chemical fume hood. This requirement inherently limited the sophistication of these experiments, as it precluded the use of the sophisticated Alpha and Proto 3D Printing machines. The Alpha machine is a fully automated 3D Printing machine developed and used for ceramic and metals applications. Three dimensional CAD pictures are inputted to the machine, sliced into layers automatically, and sent to the printhead immediately. The powder bed height, delivery of loose powder to the powder bed, and powder spreading are executed by the machine. Positioning and on/off control of the continuous, multiple jet printhead is automatic. In addition, drop placement is constantly checked using

time-of-flight measurements. However, this stand-alone machine is not outfitted with an exhaust system and it is larger than a fume hood.

The Proto machine is also a stand-alone model used for ceramic and metals investigations. The machine is outfitted with a PC-based control system that uses simple programs for positioning the printhead. The height of the powder bed and powder spreading are automated, but loose powder must be delivered to the bed surface by hand. On/off control of the printhead is automatic, but only single jet printheads can be used. This machine does not have the capacity to check drop placement or otherwise check for printing errors. The Proto machine also does not have an exhaust system or other fume hood capacity.

The Pre-Proto Machine had previously been used for testing various ceramic and metal powders and printing techniques on a smaller scale than would be required with the larger machines. The control system for this machine is key pad-based. In contrast to the more sophisticated 3D Printing machines, the processes of powder delivery, powder spreading, and powder bed height adjustment must all be executed by hand. The machine has no on/off printhead controls. The electronics necessary for generating uniform drops using piezoelectric device are not available on this machine. The Pre-Proto machine is not outfitted with an exhaust system, but this bench top machine fits in a standard chemical fume hood. Thus, the Pre-Proto Machine was selected for this work.

Pre-Proto Machine Modifications

While both types of printing described earlier are being explored for various 3D Printing applications, all of this work has been done using raster printing. The changes in direction involved in vector printing could make control of binder delivery difficult. The Pre-Proto machine was modified prior to these experiments to operate in raster mode only.

Many of the binder delivery system components on the Pre-Proto machine are polymer-based. These components are unaffected by the water-based binders used in "traditional" 3D Printing applications (ceramics and metals). The organic solvents used in this work are good solvents not only for the polymers of interest, but also for a great number of others, including many of the standard components of the binder delivery mechanism. Thus, the machine had to be adapted for use in conjunction with these solvents. Cole Parmer compatibility tables (Cole Parmer Catalog) were used as a guideline to indicate what materials could safely be used in conjunction with methylene chloride and chloroform. Flexible Viton® tubing (Greene Rubber) was selected to replace the polyurethane binder delivery tubing originally on the machine. The polypropylene filters were replaced with in-line stainless steel filters (Nupro), with a filter size of 7 μm. Teflon® tubing connectors (Cole Parmer) replaced the polycarbonate connectors used with the water-based binders. Binder and rinse reservoirs constructed of polypropylene were replaced with glass bottles placed in aluminum pressure vessels fabricated in house. Polyurethane tubing connecting the pressure tanks to both the binder and rinse vessels was replaced with the same material since the binder materials do not directly contact those lines.

Printhead Modifications

Printing of these solvents and polymeric solutions was an initial concern, since the process and the binder materials to be used with these printheads were unique from other 3D Printing binder materials. Drop-on-demand methods in 3D Printing typically employ prefabricated printheads. However, DOD printheads compatible with the solvents to be used as binders are not commercially available. Conversely, the continuous printhead used with the water-based binders is amenable, with some modification, to printing the solvents of interest. Thus,

continuous jet printing was selected as the binder delivery method for these experiments.

However, the solvents to be considered for the binders in this work are unlike water in that they are not polar or ionizable. As a result, they are difficult to charge and deflect. In addition, some of the potential solvents/binders are somewhat flammable, which is added cause for concern in charging these materials. Finally, since the Pre-Proto Machine was not outfitted with the proper electronics for charging the printheads. As a result, these experiments are done with this printhead operating continuously, but without the charge and deflect "on/off" feature. This limits the printed structures to be composed of continuous straight lines across the powder bed. Also, printing in this way necessitated rotating the powder bed so that printed lines would be uniform in both directions.

The body of the printhead to be used in these experiments was fabricated specifically for 3D Printing applications and is composed of stainless steel. Small bore tubes connect the Viton® tubing to the channels within the steel body. The channels deliver the binder to an opening at the bottom of steel body that is covered with an electroformed nickel orifice plate. This plate contains an orifice hole of diameter 45 μm. The binder is forced through the orifice by pressurized nitrogen. Thus, the orifice plate is critical to the formation of the stream of binder drops to be delivered to the powder bed. Both the orifice plate and the small bore tubes were attached to the steel body using Red RTV 106 silicone rubber (General Electric) previously. This material was incompatible for use with organic solvents, as demonstrated in the failure of the bond between the orifice plate and the printhead body after only a few minutes of actual printing. The connection between the small bore tubes and the printhead body also eventually failed, but at much longer times than the orifice plate bond.

The printhead itself also required some modification. These adaptations were the most difficult. First, the silicone rubber used in bonding the orifice plate

and the tubes was replaced by a chemically inert epoxy. A two component epoxy (Epo-Tec) offered only a modest improvement. The orifice plate-epoxy bond was adequate to withstand one hour of printing, but failed soon after. In contrast, the tubing bond was durable enough to withstand several hours of continuous printing.

Next, an alternative orifice plate bonding mechanism was attempted using hot polyethylene. Sections from polyethylene sandwich bags (Glad) were melted onto the orifice plate surface of the stainless steel body of the printhead, which was heated on a hot plate. The orifice plate was then applied to the surface and clamped until cooled to room temperature. If the polyethylene was heated too high, it degraded and did not form a tough bond. If it was cooled too quickly, a tough bond was not formed. This process was much more difficult and was nearly impossible to characterize for consistency; as a result, only one in five attempts resulted in a viable bond. The small bore tubes were still attached using the Epo-Tec epoxy, which had to be done prior to the polyethylene bonding. Repeated heating of the epoxy resulted in premature failure of that bond as well. Nevertheless, the viable bonds were an improvement over the epoxy attempts, as the printheads could be used for up to four hours before the bond would fail.

Finally, a viable epoxy bonding material for the orifice plate was obtained. Morton Epoxy A-701 is a single step (no mixing of hardener and resin) epoxy that is cured for 2 hours at 200°C. This bond is quite durable. The orifice plate has failed only once in hundreds of hours of operation since this epoxy was employed. This epoxy was also successfully used to bond the small bore tubes to the printhead body. This bond has not failed. Obviously, since these bonds do not dissolve, much care must be taken in applying the epoxy. However, once applied and a steady stream is obtained, the printheads are largely maintenance free. Printheads can be prepared months in advance of use.

4. FUNDAMENTALS OF BINDER-POWDER INTERACTIONS

Initial investigations in processing polymeric materials by 3D Printing required characterization of the bonding interaction between binder and powder. Bonding of polymeric powders is inherently different from bonding of ceramic powders because the solvent binders can dissolve the polymer particles. The primary interaction phenomena are dissolution (and bonding) of the polymer and evaporation of the solvent component of the binder from the powder bed. If dissolution is too slow and/or evaporation is too fast, powder particle bonding may not occur. In addition, understanding what other phenomena influence the structure and resolution of polymer features created by 3D Printing is critical for the design and fabrication of more sophisticated devices.

Single Drop "1D" Primitives

The most basic event in the 3D Printing process is a single droplet of binder impacting the powder bed. The key issues that differentiate the polymer fabrication process from ceramic and metal fabrication processes can be determined from simple experiments in which a single drop of solvent binder impinges on the powder bed.

Experimental Procedure

The single drop experiment was performed using a 26 gauge (internal diameter = 400 μm) intradermal beveled syringe to deliver a single droplet of 100% methylene chloride binder to a powder bed of PCL (powder size = 75-150 μm). The size of the droplet produced by the syringe is about 2300 μm in diameter, which is larger than the syringe internal diameter due to the syringe bevel

and die swell. Die swell is also observed with the actual printhead, as the binder jet is about 75 μm in diameter, which is 2/3 larger than the orifice itself. As described in Appendix A, the jet yields droplets about 142 μm in diameter. Despite the dramatic difference in the size of the printhead droplets and the syringe drops, this experiment is a useful first step in the examination of the interaction between the binder and the powder material.

Results

The Scanning Electron Microscope (SEM) micrographs in Figures 4.1a and 4.1b show the results of this single drop experiment. The powder particles are completely dissolved and have formed a dense polymer feature following solvent evaporation on the top of the polymer "ball", as shown in Figure 4.1a. The desired particle-to-particle bonding obtained in this example indicates that sufficient polymer dissolution occurs prior to the evaporation of the solvent. These results constitute a successful demonstration of particle bonding, which is integral to 3D Printing, achieved by powder dissolution and recasting.

Also important to note from this experiment is the character of the outer edges of the ball. Figure 4.1b shows that partially dissolved polymer particles dominate the sides and bottom surface of the feature. Such incomplete powder dissolution may be due to capillary wicking of binder within the powder bed. Partially dissolved adherent particles compromise fine resolutions, as they produce an increase in the size of those features. As a result, the initial size of the powder also impacts resolution, since use of a larger powder size would result in larger particles adhering to the surface. Furthermore, partially dissolved particles attached to feature surfaces could promote entrapment of otherwise unbound loose powder.

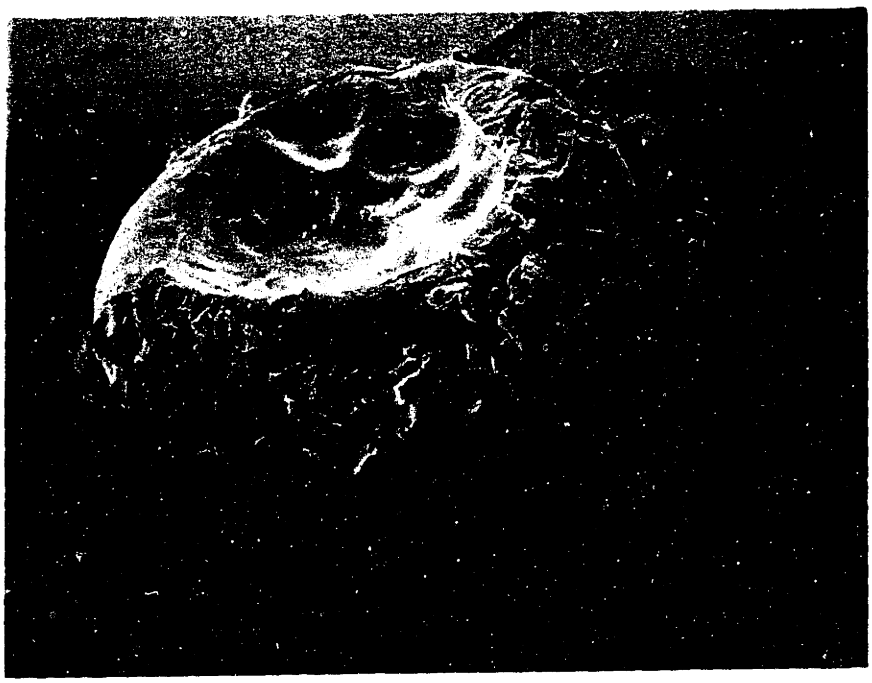

Figure 4.1 (a) Polymer "Ball" formed by a single drop from a syringe; (b) Surface of Polymer Ball

Single Line "2D" Primitives

The next level of development is a single line. Complex shapes are constructed by the sequential stacking of printed layers, each of which is composed of many single lines. Thus, the line "primitive", a stand-alone single line printed into a powder bed using the 3D Printing machine, can be considered the fundamental feature in 3D Printing. Single line primitives may be used to characterize the size of features that can be printed using specific printing conditions. The "feature size" of a line primitive is the line width measured from the outermost edges of particles forming the line. The feature size is determined by photographing representative lines and measuring the width of the lines.

The size of line primitives is dependent on many variables, including powder size and composition and the amount and composition of binder delivered. The size of powder particles impacts the feature size, as discussed above in relation to partially dissolved adherent particles. Similarly, the amount of binder delivered can also influence the size of the line feature. For example, construction of a line with a large diameter would require more binder than a thinner line simply because more material would be involved in the larger feature. The amount of binder delivered to the powder bed, in turn, is dependent on two parameters: binder flow rate and printhead speed. Binder flow rate is the volumetric or mass flow rate out of the printhead. Printhead speed is the linear velocity at which the printhead moves over the powder bed. For a constant printhead speed, a high binder flow rate would result in the delivery of more binder than a low binder flow rate. For a constant binder flow rate, a high printhead speed would result in the delivery of less binder than a low printhead speed because the printhead would spend less time over the powder bed.

Thus, the important measure of binder delivery is the binder flow rate to printhead speed ratio, or "binder per unit line length" (β). This single parameter

accounts for variability in both binder flow rate and printhead speed and is defined by

$$\beta = \frac{F}{152.4\, v_p\, \rho_b} \tag{4.1}$$

where F = binder flow rate (g/sec)

v_p = printhead speed (cm/sec)

ρ_b = binder density (g/cm^3).

This parameter makes it possible to compare binder delivery rates for different printing conditions, as illustrated in Figure 4.2. For example, the binder per unit line length is clearly higher for a high flow rate/low printhead speed condition (Fig 4.2a) compared to a low flow rate/high printhead speed set-up (Fig 4.2b). However, low flow rate/low printhead speed and high flow rate/high printhead speed scenarios might yield the same binder delivery rate, as shown in Figures 4.2c and 4.2d, respectively. Thus, binder per unit line length serves as a good quantitative measurement for comparing how much binder is delivered during printing for all conditions.

Experimental Procedure

Experiments were performed to define the relationships between powder composition, powder size, binder composition, binder per unit line length, and feature size. Single line primitives were fabricated by printing straight lines separated by at least 5 mm. Ten lines were printed at 5 or 6 binder per unit line length levels for each binder/powder pair. After printing, the lines were harvested from the powder bed using tweezers and placed in a sample box. Solvent

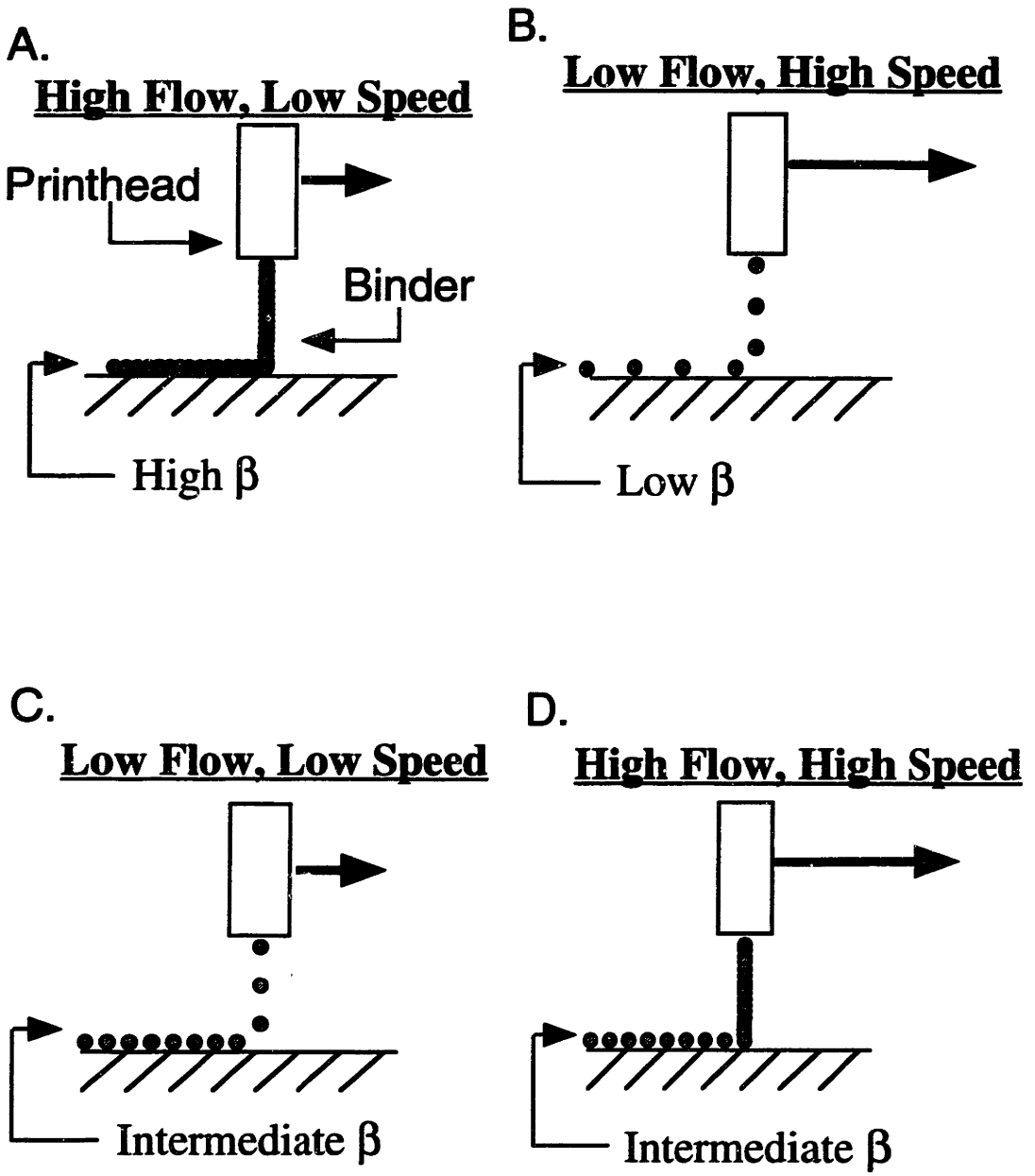

Figure 4.2 Binder per unit line length levels for different printing conditions

evaporation was fast enough that the single lines could be removed from the powder bed without deformation within two minutes after printing was completed. Each sample box was left open in the hood for at least 10 more minutes to allow residual binder solvent to evaporate. Two 1 centimeter segments from two different lines for every binder-powder pair at each binder per unit line length level were examined. Each sample was gold-coated using normal currents but short coating times (15-20 seconds at 40mA) in order to prevent distortion of the structures during the coating process. These segments were then examined for uniformity using the SEM. Single line primitive diameters were determined from SEM micrographs.

The eight binder-powder pairs used for fabricating single line primitives are summarized in Table 4.1. In particular, single line primitives were constructed from PCL (lot# 434850 with M_w= 23,000) and PLA (lot# ELX-XX7 with M_w= 132,000), each with powder sizes of 45-75 μm and 75-150 μm. Experiments using powders smaller than a printed binder droplet (particle sizes less than 45 μm) were also of interest, since the feature size of lines constructed with such powders would likely be governed by the size of the binder droplet rather than the size of the powder particles. However, due to the milling limitations discussed above, insufficient amounts of such powders were available.

All four of these powders were used to construct line primitives with a 100% chloroform solvent binder. In addition, two different polymeric solution binders were printed on the PCL powders: a 10 weight percent (wt%) solution of PCL (M_w = 23,000) in chloroform and a 26.5 wt% solution of acid-modified PCL (M_w = 10,000) in chloroform. Solutions of chloroform and PLA were not used as binders because, even at low concentrations (<5 wt%) of the available molecular weights of PLA, the solutions were too viscous to print due to clogging of the printhead.

Table 4.1 Binder-powder combinations used in single line primitive experiments (X = used, - = not used)

Powder		Binder: 100% $CHCl_3$	Binder: 10 wt% PCL in $CHCl_3$	Binder: 26.5 wt% acid modified PCL in $CHCl_3$
PCL	75-150 μm	X	X	X
	45-75 μm	X	X	X
PLA	75-150 μm	X	-	-
	45-75 μm	X	-	-

Results

Polycaprolactone

Disjointed line segments, rather than contiguous lines, were often formed at binder per unit line length levels less than 2.0×10^{-4} cm^3/cm, particularly with the 45-75 μm powders. When line segment formation was observed, the above printing procedure was repeated, the powder bed was rotated 90°, and ten additional lines were printed at the same binder per unit line length level perpendicular to the first set. This process simplified the recovery of the segments from the powder bed, but representative samples were still produced beyond the overlapping regions.

All of the PCL lines had relatively uniform surfaces, with partially dissolved or loose powder dominating the line surfaces. Figure 4.3 shows an end-on view of a single line primitive and the partially dissolved powder is easily visible. In addition, this view shows the shape of a line primitive. The cross

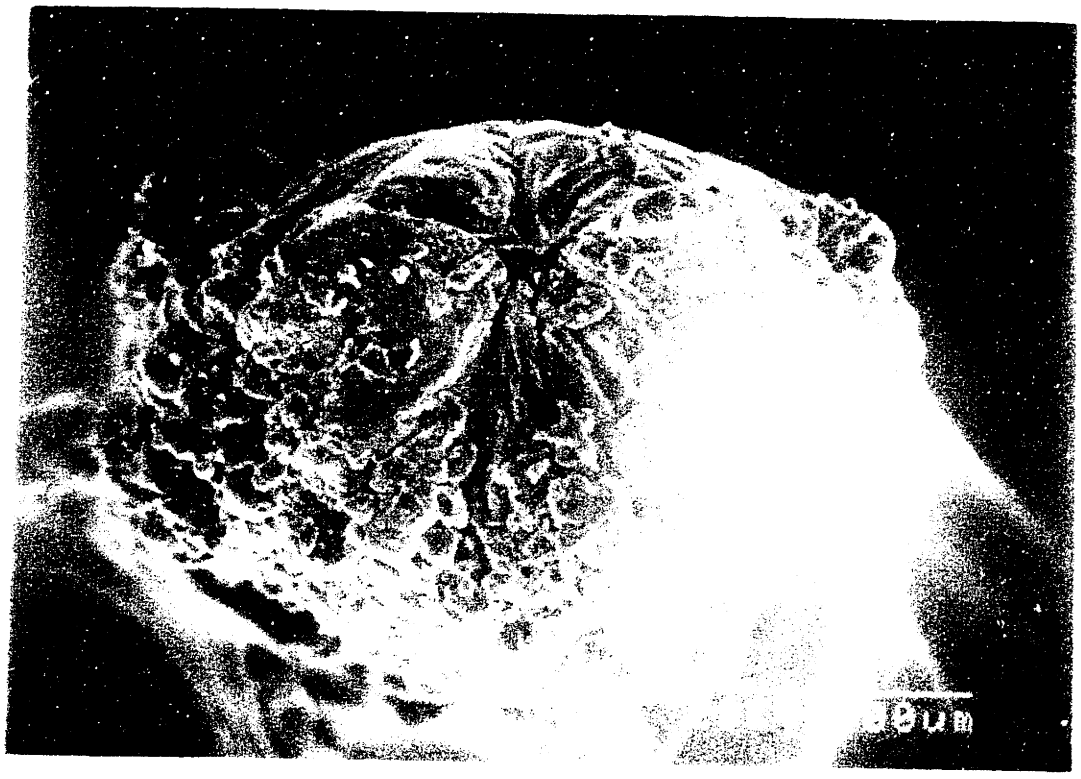

Figure 4.3 End view of a single line primitive.

section is somewhat oval in shape, as the side-to-side dimension is 22% larger than the top-to-bottom size. The difference is largely due to partially dissolved adherent particles. Such particles increase the side-to-side dimension twice as much as the top-to-bottom dimension because they are located on both the sides and the bottom of the line, but not on the top surface, which is generally smooth and free of adherent particles. Thus, while the "core" of the line may be relatively uniform in diameter, the eccentricity described here is produced from the asymmetrical presence of partially dissolved powder. Nonetheless, a circular cross section based on the side-to-side dimension and a cylindrical line volume are fairly reasonable approximations. In addition, approximating the line diameter as

the line width from a top view of the single line primitive will give the largest possible feature size for that line, accounting for all of the partially dissolved particles on both sides of the line. Note that these PCL samples were gold coated in the as-harvested state.

The feature size vs. binder per unit line length data for all three binders and both PCL powder sizes are shown in Figures 4.4 and 4.5. The line primitive feature size using 75-150 μm powder (Fig 4.4) varied between 550 μm and 900 μm for the 100% solvent binder, between 400 μm and 650 μm for the 26.5% acid modified PCL in chloroform binder, and between 300 μm and 675 μm for the 10% PCL in chloroform binder. For the 45-75 μm powder experiments (Fig. 4.5), the size of lines varied from 240 μm to 620 μm for the 100% solvent binder and from 190 μm to 540 μm for the 10% PCL in chloroform binder. Only two data points were available from the samples printed with 26.5% acid modified PCL in chloroform binder, so that information was not plotted.

Some trends are apparent from this data. The line primitive feature size is smaller for lines printed with the 45-75 μm powder than those printed with the 75-150 μm powder for all binders at all binder per unit line length levels. This result agrees with the single drop experiment in that smaller, partially dissolved particles on the outer edges result in a smaller feature size. Furthermore, more complete dissolution of polymer particles might be achieved when printing on the 45-75 μm powders because the surface area to volume ratio for those particles is greater than for the 75-150 μm particles. Greater dissolution of the particles allows them to become more tightly packed after solvent evaporation, resulting in a higher density and smaller diameter line. Lower tap densities for the 45-75 μm powders relative to the 75-150 μm powders might also result in less total material being incorporated in a given line, producing a smaller diameter line.

The relationship between the feature size of lines printed with solvent binders and lines printed with polymeric solution binders with the same sized

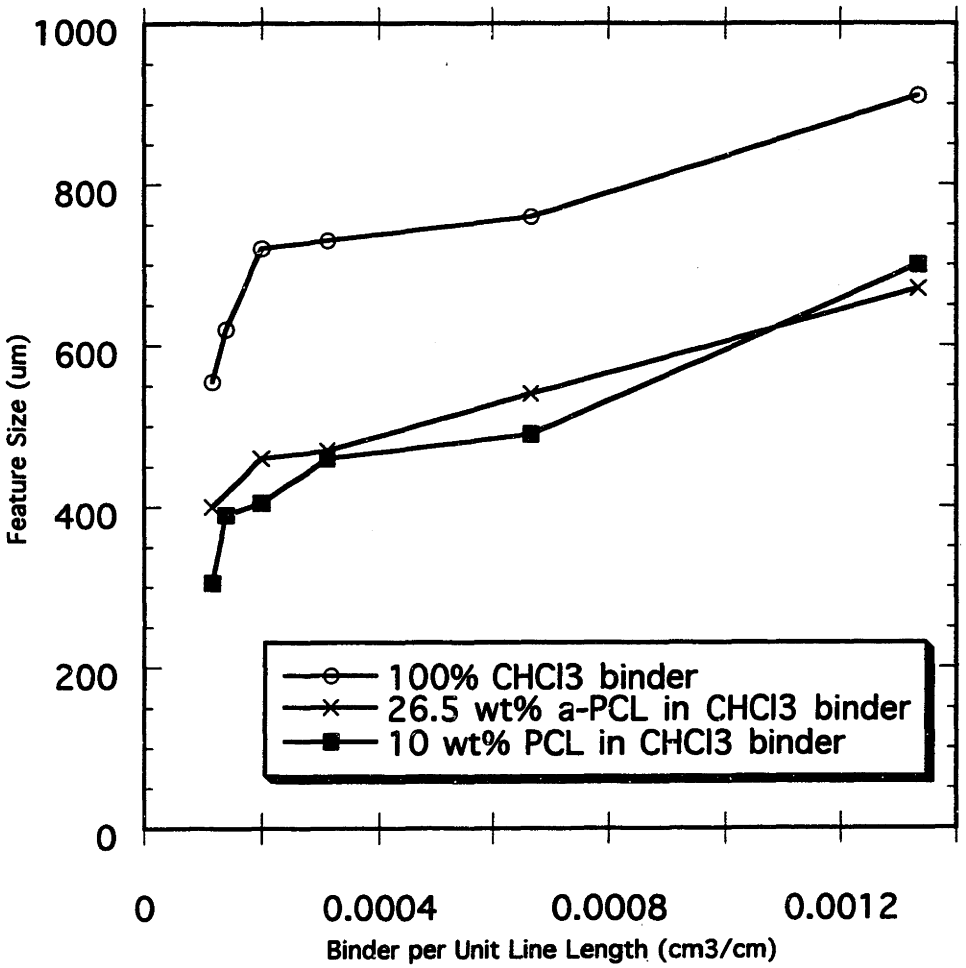

Figure 4.4 Line Primitive Feature Size vs. Binder per Unit Line Length for binders printed on 75-150 um PCL

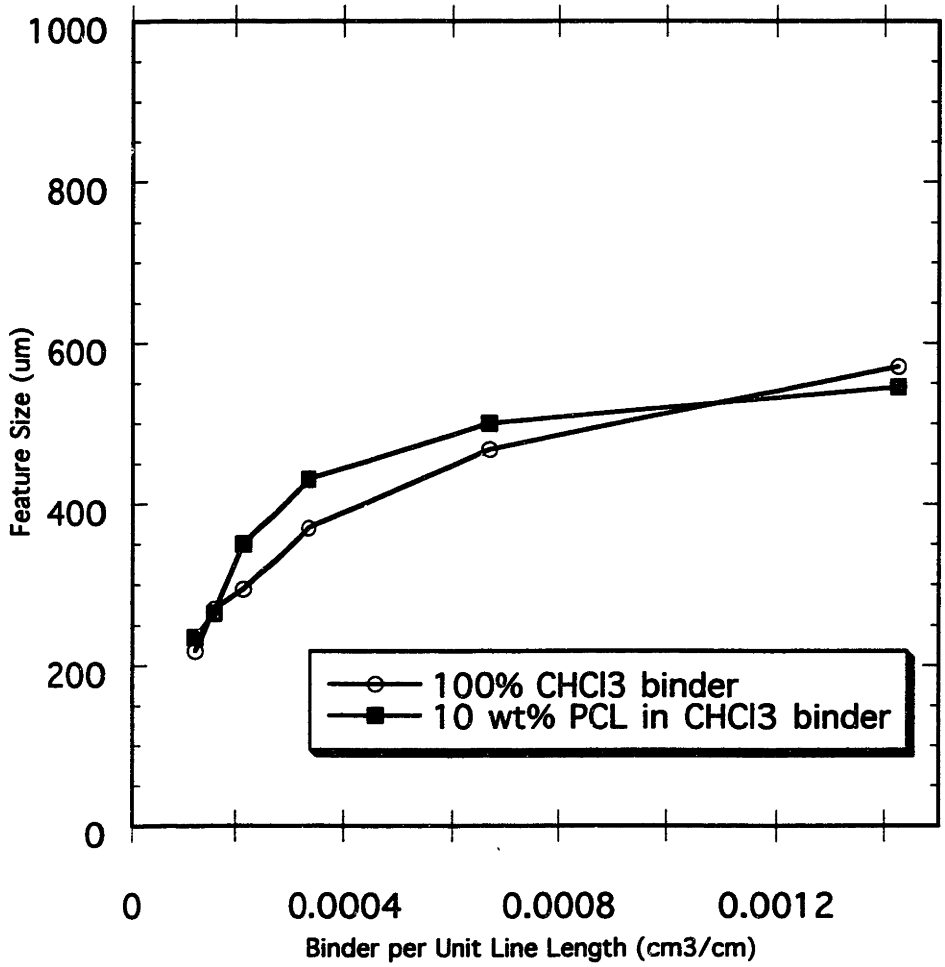

Figure 4.5 Line Primitive Feature Size vs. Binder per Unit Line Length for binders printed on 45-75 um PCL

powder is less apparent. In some cases, lines printed with a solution binder are larger than corresponding lines printed with a solvent-only binder. A facile explanation for the larger feature size is that mass is added to the powder bed when printing with polymeric solution binders. The influence of binder polymer on total line composition and size can be determined from a simple calculation.

From the data in Figure 4.5, consider a 468 μm (diameter) line, 1 cm long, fabricated from 45-75 μm PCL using a 100% chloroform binder solution at a binder per unit line length level of 6.68×10^{-4} cm^3/cm. The total volume of that line of length 1 cm (void space plus polymer) is 1.72×10^{-3} cm^3. Table 4.2 shows the possible line primitive final density and total polymer mass for the 468 μm line. The total mass of polymer in the line depends on the final line density, which varies between the powder bed tap density (0.34 g/cm^3) and the theoretical solid polymer density (1.1 g/cm^3). The polymer mass in that line is between 0.58 mg and 1.89 mg, as shown in Table 4.2. For lines printed with a polymeric solution binder, the polymer content is higher. For a higher polymer content and the same line density, the line must have a larger diameter. Table 4.2 also shows total polymer mass and line diameters at each of four densities line primitives printed with a 10 wt% PCL in chloroform binder. For this binder per unit line length level, 0.09843 milligrams of polymer would be added to a 1 centimeter (length) line using such a binder. Thus, the polymer content of lines printed with this binder would be between 0.68 mg and 1.99 mg. The lines printed with polymeric solution binders would be 2.5% to 8% larger than similar density lines printed with a solvent-only binder. Experimental data from printing on 45-75 μm PCL at a binder per unit line length level of 6.68×10^{-4} cm^3/cm yielded a feature size of 468 μm for the 100% chloroform binder and a feature size of 500 μm for the line printed with the 10 wt% PCL in chloroform binder, comparable to what would be expected for these binders according to Table 4.2.

The difference in size may be attributable to other sources as well. The evaporation of solvent from the polymeric solution binder may be slower than evaporation from a 100% solvent binder. Slower evaporation would allow for more exposure of the powder bed material to the binder prior. As a result, the effective binder per unit line length for the polymeric solution binder would be higher than that for the pure solvent binder printed under the same conditions. A higher effective binder per unit line length would certainly result in a larger feature size. Regardless of the mechanism, the size difference between lines printed with pure solvent binders and lines printed with polymeric solution binders can be explained by considering the effects of the polymeric material added in the binder.

For the 45-75 μm powder, the lines printed with the 10 wt% PCL in chloroform solution binder are, indeed, slightly larger (a particle size or less) than those printed with the pure solvent binder over the whole binder per unit line length scale. The addition of polymeric material in the polymeric solution binder, as predicted, results in a larger feature size relative to the 100% solvent binder case (in which no additional polymeric material is added via the binder). Only two data points are available for lines printed on 45-75 μm powder using the 26.5 wt% acid modified PCL in chloroform binder, so analysis of that data relative to the other printing scenarios is not reliable.

However, for the 75-150 μm powder, the feature size is always smaller for the primitives printed with the polymeric solution binders relative to those printed with the pure solvent binder. The feature size difference is always approximately two particle sizes. It is anticipated that binder wicks the same distance in the powder bed regardless of its composition[15]. However, in preparing the binders, it was observed that the polymeric solution binders dissolved additional PCL particles more slowly than the solvent-only binders. It is likely that the particles sitting at the binder interface in the powder bed are similarly

Table 4.2 Line Primitive Diameters for Solvent-only and Polymeric Solution Binders (assuming length of 1 cm)

Solvent-Only Line Diameter	Line Primitive Final Density	Solvent-Only Polymer Mass	Solution Binder Polymer Mass	Solution Binder Line Diameter
468 μm	1.1 g/cm^3	1.89 mg	1.99 mg	480 μm
468 μm	0.75 g/cm^3	1.29 mg	1.39 mg	486 μm
468 μm	0.5 g/cm^3	0.86 mg	0.96 mg	494 μm
468 μm	0.34 g/cm^3	0.58 mg	0.68 mg	505 μm

slowly dissolved by a solution binder relative to a solvent-only binder. As a result, solvent may evaporate from a polymeric solution binder before those interfacial particles can be permanently attached to the printed line, whereas such particles are bonded to the printed line by the solvent-only binder, which would dissolve them more quickly. The absence of one such particle on each side of the line would account for the observed size difference. This theory is consistent with the morphology of these lines. Figure 4.6 shows SEM micrographs of lines printed on this powder using the two binders. The line printed with the solvent binder (Fig. 4.6a) has adherent particles with abrupt, sharp edges, which indicates those areas of the particles were not exposed to binder. Conversely, on the line printed with the polymeric solution binder (Fig 4.6b), the adherent particles are all slightly smoothed and rounded. This indicates those particles were fully exposed to the binder. Thus, it appears that the polymeric solution binder did not permanently bond powder to which it was only partially exposed, which resulted

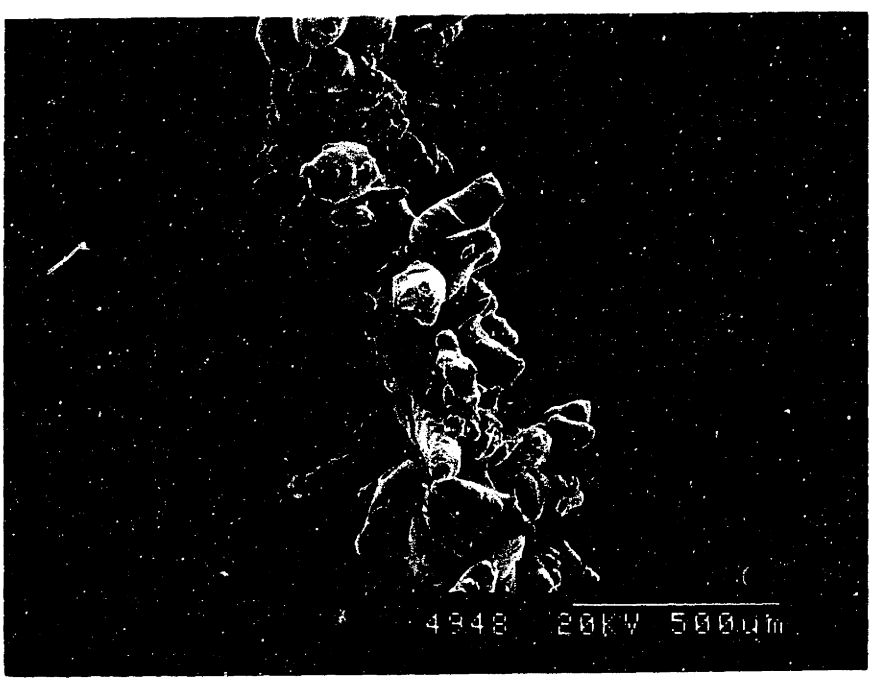

Figure 4.6 (a) Line primitive printed with 75-150 μm PCL using 100% chloroform binder; (b) Line primitive printed with 75-150 μm PCL using 10 wt% PCL in chloroform binder.

in the observed feature size difference in lines printed with the different binders on the 75-150 μm PCL powder.

An unexpected result occurred when printing onto the 45-75 μm PCL with a 100% chloroform binder at the highest binder delivery rate (1.425 X 10^{-3} cm^3/cm). These conditions are theoretically the most favorable conditions for complete dissolution of the powder particles. The printed lines were contiguous, but were composed of connected "sausage links, in contrast to the relatively uniform cylindrical-like (straight-sided) lines formed in all other cases. A new link formed every 800-1000 μm along the length of the line (Figure 4.7). The links are about 650 μm in diameter, while the "pinches" between the links are about 500 μm across. Relative to the other feature size data, a line with a constant diameter close to the link diameter would be anticipated. If the powder incorporated in these lines is fully dissolved, any structure attributable to the powder in the bed would be eliminated. Thus, the structure of these line primitives would depend only on solvent evaporation. As a result, one explanation for the sausage link formation may be that this "pinching off" may alleviate some of the internal stresses that are generated in the solidifying line during the process of solvent evaporation.

Poly(Lactic Acid)

A significant amount of loose powder adhered to the printed lines in all of the PLA experiments in which the 100% chloroform binder was printed on both the 45-75 and the 75-150 μm powders (Figure 4.8). This undissolved powder was held in place by weak cohesive "sticking" only. Some of this phenomenon may be due to a very small amount of dissolution on the particle surfaces. Such dissolution might be sufficient to bond the particle, but not enough to permanently adhere it. The loose powder was removed from the PLA samples by

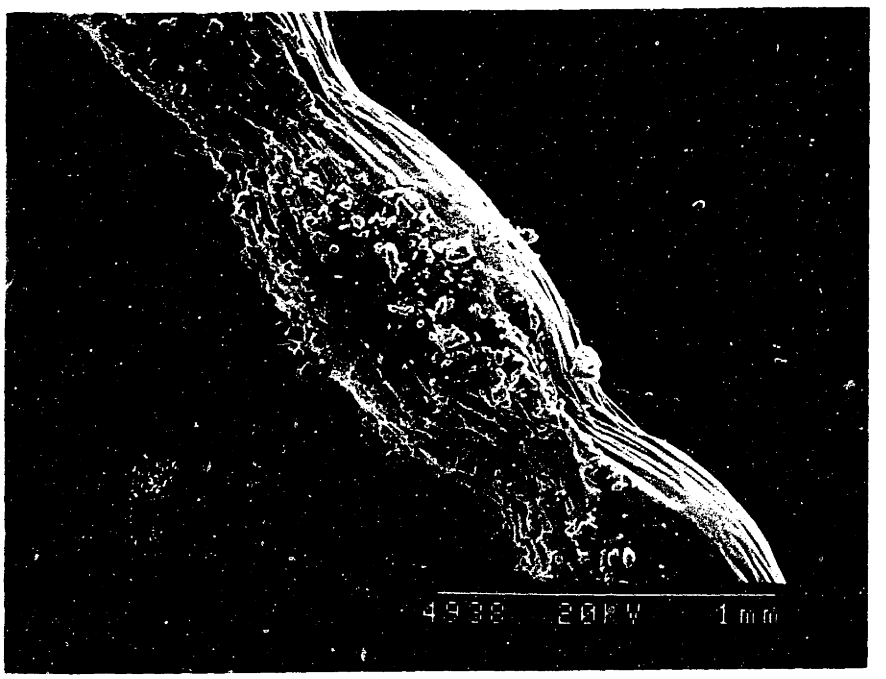

Figure 4.7 "Sausage links" formed in line printed with 45-75 μm PCL using 100% chloroform binder

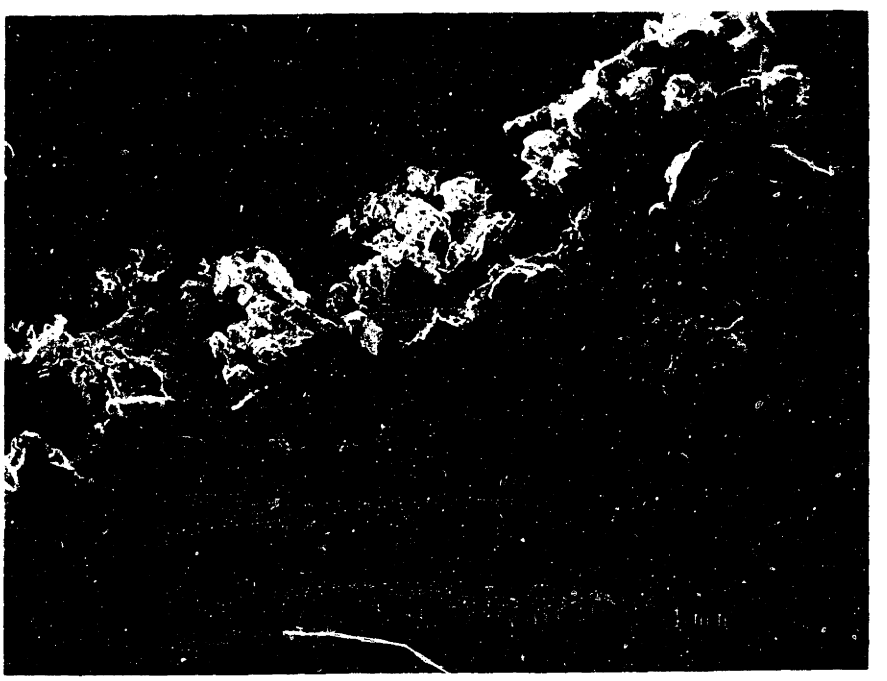

Figure 4.8 Cohesively-held loose powder on PLA line primitive

dropping the samples from a height of 10 cm onto a hard surface. Although the loosely adherent particles could easily be removed from these single line primitives, removal of this powder from more complex devices could be problematic. The PLA "cores" appeared to be very similar in character to the PCL samples (Figures 4.9a and 4.9b).

The feature size data for the 100% solvent binders and both PLA powder sizes are shown in Figure 4.10. The line primitive feature size using the 75-150 μm powder varied between 410 μm and 810 μm for the 100% solvent binder. The lines printed with the 45-75 μm powder using this binder varied in diameter between 300 μm and 550 μm.

The relationship between feature size and initial powder size for PLA is similar to that described above for PCL. The line primitive feature size obtained using the 45 -75 μm powder is always smaller than that obtained using 75-150 μm powder at the same binder per unit line length level. There appears to be more scatter in this data. It was observed while preparing binder solutions that dissolution of the PLA powder particles was much than that for PCL particles of a similar size. Slow dissolution may be the source of the scatter in the data, as it could result in largely intact particles being stuck on the line surface. The presence of such intact particles on the line surfaces made feature size measurements more difficult to determine because it increased variability of the surfaces.

In addition, the PLA/100% solvent data can not be directly compared with the PCL/100% solvent data because the pre-gold coating treatments were different. Dropping the PLA structures may have displaced some partially dissolved particles in addition to the loosely held powder. The PCL lines were not dropped and retained all partially dissolved particles. Nevertheless, similar trends in the feature size versus binder per unit line length are apparent for both cases.

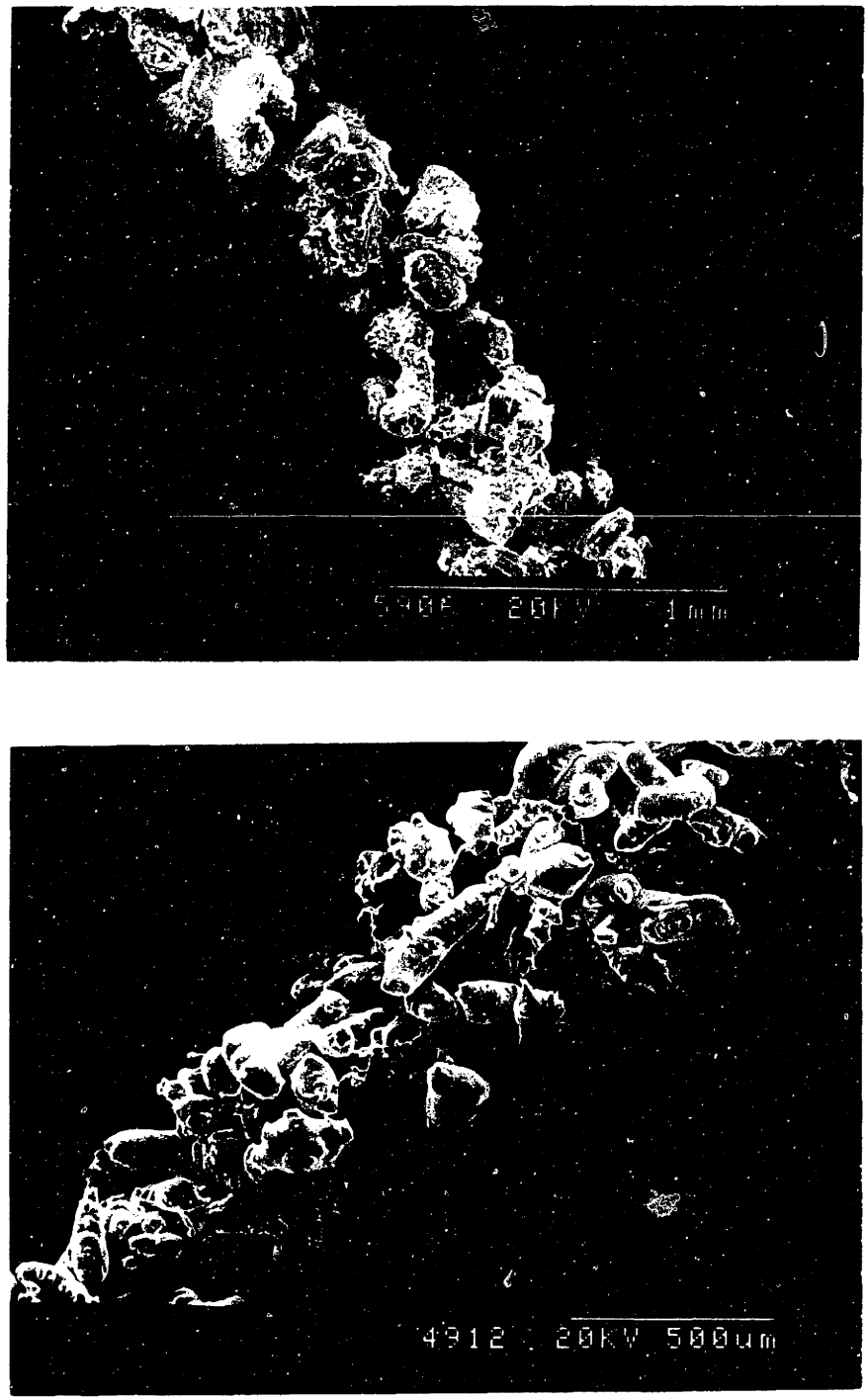

Figure 4.9 (a) PLA "core" with loose powder removed; (b) PCL line primitive

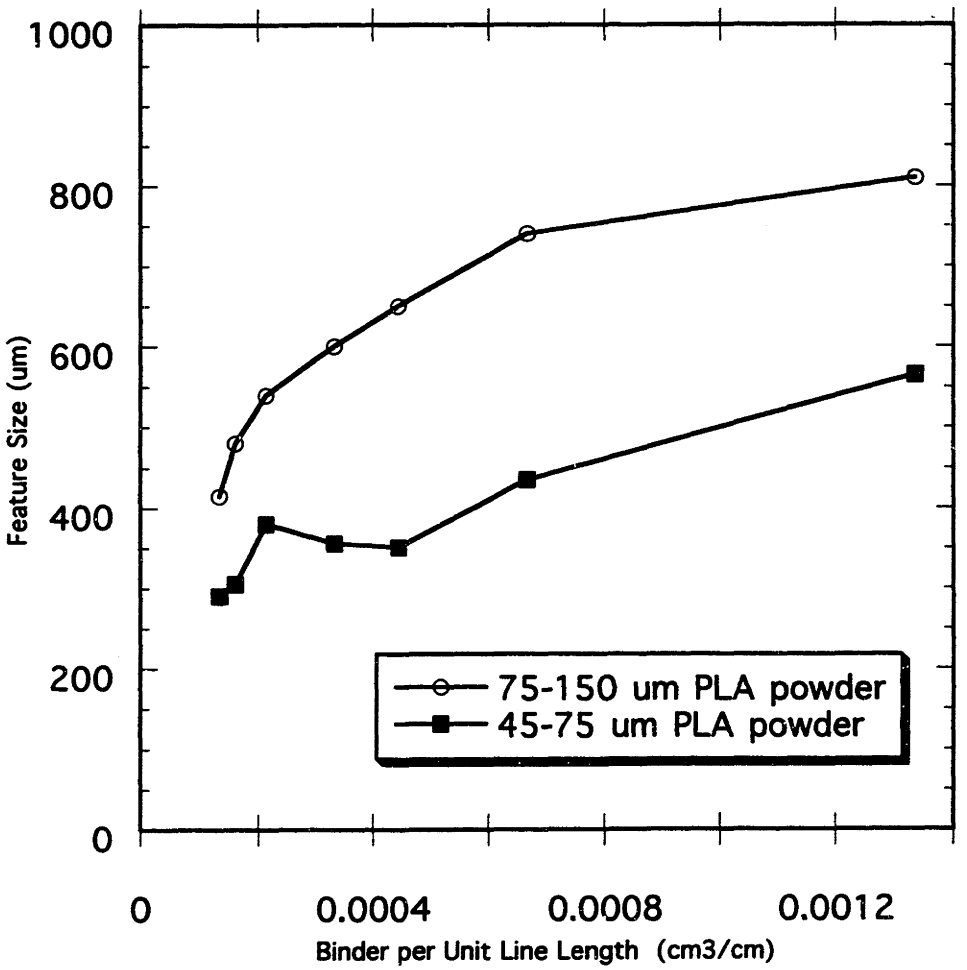

Figure 4.10 Line Primitive Feature Size vs. Binder per Unit Line Length for 100% chloroform binder printed on 45-75 um and 75-150 um PLA

These data are useful for the design of more complex structures. They are immediately useful for the design of devices that use the same powder and binder materials. For example, consider the design of a device requiring a 500 μm channel running through the structure to be constructed from 75-150 μm PCL using a 10 wt% PCL in chloroform binder at a binder delivery rate of 2.0×10^{-4} cm^3/cm. These results indicate that printed lines on either side of the channels must be printed at least 900 μm apart to avoid filling the channel with printed material (each line would overlap the separation by one line radius for a total of 400 μm).

5. ANALYTICAL RELATIONSHIP BETWEEN FEATURE SIZE AND PROCESS PATAMETERS

It is necessary to examine the fundamental phenomena that control feature formation in order to apply these experimental line primitive feature size results to the design and fabrication of fundamental and complex structures with these and other powder-binder systems. The dominant processes can be quantitatively described by comparing experimental and theoretical line primitive feature size data. Such an approach requires the development of a feature size model.

Background

The feature size of line primitives created by 3D Printing can be modeled in terms of key geometric and physical parameters of the printing system. Such an analysis has been done for ceramic powders. Figure 5.1 shows the typical feature size-binder per unit line length relationship for ceramic powder bed materials. For those systems, the feature size varies linearly with the binder delivered at low binder per unit line length levels. However, a transition is observed at an intermediate delivery level (shown as β_t in Figure 5.1) and the dependence of feature size on binder delivered shifts to another line with a much steeper slope. The shift in this relationship is observed at the binder delivery level in which the void spaces around the powder bed particles are filled to the highest extent possible. At higher delivery levels, binder delivered can not further fill void spaces in the printed region, so it "bleeds" into the surrounding region. This phenomenon results in the dramatic increase in feature size observed at those binder delivery levels.

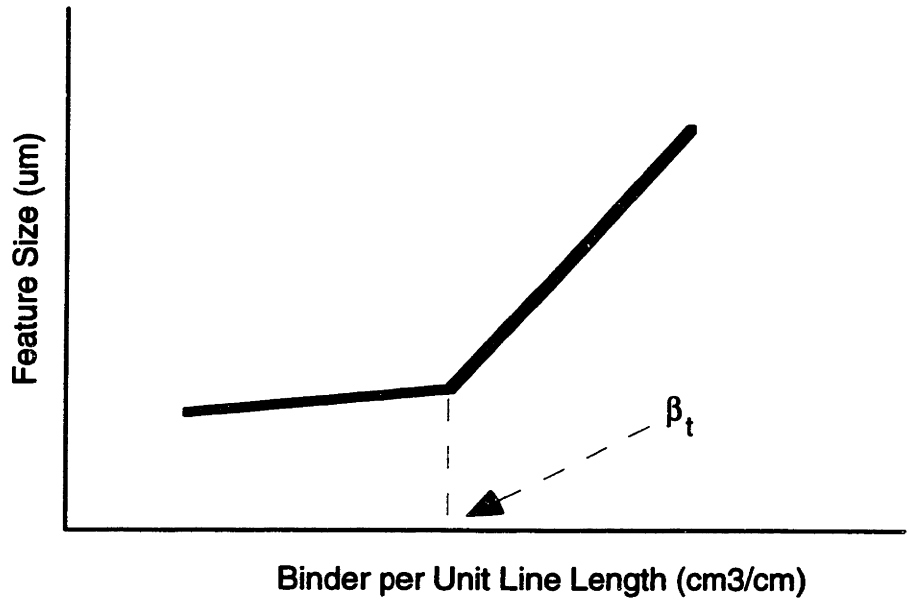

Figure 5.1 Typical Feature Size-Binder per Unit Line Length relationship for ceramic powder bed materials

The polymeric materials system investigated in this work is fundamentally different from those 3D Printing materials systems, however. For example, no change in the shape of ceramic powder bed particles occurs during the printing process, while polymer particles are easily dissolved by the solvent-based binders. Also, ceramic and metal powders are generally much smaller than the size of the binder drops (10-20 μm particles vs. 65-75 μm drops). As a result, the line primitive feature size for those materials is governed by the size of the drop at binder per unit line length levels below β_t. In contrast, the polymeric powder particles used in these experiments are always on the order of, or larger than, the binder drop in size, so the line primitive feature size is dominated by the particle size. As a result, the feature size-binder delivered relationship in Figure 5.1 likely does not describe polymeric features fabricated by 3D Printing, and different

parameters and processes must be considered to adequately characterize these structures.

Derivation of Polymer Line Primitive Feature Size Equation

The line primitive feature size can be theoretically estimated in terms of the physical parameters that describe the printing system. The geometric shape of line primitives fabricated in this work is roughly cylindrical, as shown in Figure 4.3 and illustrated schematically in Figure 5.2. The total volume of such a cylindrical line is given by

$$V = \left(\frac{\pi}{4}\right) D_{bd}^2 L \tag{5.1}$$

where V = line volume (cm^3)

L = line length (cm)

D_{bd} = diameter of line defined by binder (cm).

The volume available for binder during printing is the void fraction times the total volume

$$V_b = \left(\frac{\pi}{4}\right) D_{bd}^2 L\varepsilon \tag{5.2}$$

where ε = powder bed void fraction

V_b = volume available to binder (cm^3).

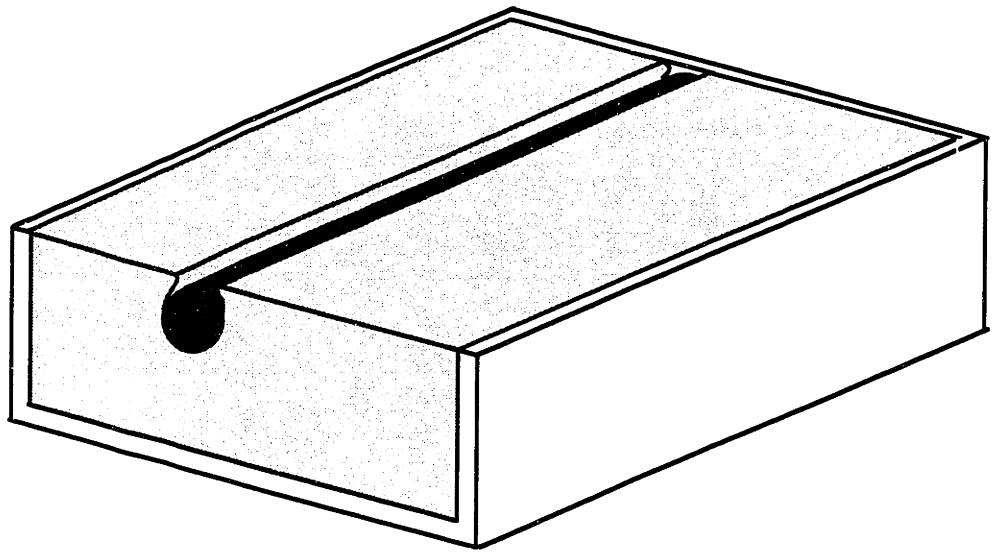

Figure 5.2 Model of a cylindrical printed line sitting in the powder bed.

The powder bed void fraction is

$$\varepsilon = \frac{(\rho_p - \rho_o)}{\rho_p} \tag{5.3}$$

where ρ_o = powder bed tap density (g/cm^3)

ρ_p = density of solid powder material (g/cm^3),

so equation 5.2 can be rewritten as

$$V_b = \left(\frac{\pi}{4}\right) D_{bd}^2 \left(\frac{(\rho_p - \rho_o)}{\rho_p}\right) L \qquad (5.4)$$

As mentioned, the void volume of the powder bed within the printed line is not completely filled with binder during printing. In addition, inaccessible internal pores might be created by the dissolution and recasting of "external" polymer powder particles. This incomplete filling of available void volume by printed binder must be accounted for in quantitative relationships between feature size and printing variables.

"Saturation" is defined as the fraction of the void volume of a printed line that is filled with binder during the printing process. This term quantifies the extent to which powder particles are contacted by binder in the powder bed. It is an average value of the extent of void filling within the entire line volume defined by the feature size.

The amount of binder delivered to powder bed is

$$V_d = (L)(\beta) \qquad (5.5)$$

where V_d = volume of binder delivered to bed (cm^3)

β = binder per unit line length (cm^3/cm).

Saturation is given by the ratio of equation 5.5 to equation 5.4, or

$$S = \frac{V_d}{V_b} = \frac{\beta}{\left(\frac{\pi}{4}\right) D_{bd}^2 \left(\frac{(\rho_p - \rho_o)}{\rho_p}\right)} \qquad (5.6)$$

where S = saturation.

Equation 5.6 can be rearranged to yield

$$D_{bd} = \left(\frac{4\beta\,\rho_p}{\pi S\,(\rho_p - \rho_o)}\right)^{1/2} \qquad (5.7)$$

Equation 5.7 indicates the diameter of the region defined by the printed binder. The volume of a line with this diameter is

$$V_{bd} = \left(\frac{\beta L\,\rho_p}{S\,(\rho_p - \rho_o)}\right) \qquad (5.8)$$

where V_{bd} = volume of the as-printed line defined by the binder (cm^3).

The tap density of the powder bed then can be used to determine the total mass of polymer (in the form of powder) in this defined region. The total powder mass in a printed line is given by

$$M_{pp} = V_{bd}\,\rho_o = \beta L\left(\frac{\rho_o\,\rho_p}{S\,(\rho_p - \rho_o)}\right) \qquad (5.9)$$

where M_{pp} = mass of polymer powder in printed line region (g)

However, Equation 5.9 only accounts for the polymeric material in the powder bed. It does not include effects of polymer added in the binder. The volume of polymer added when using a polymeric solution binder is

$$V_{pb} = (\beta)(\omega)L \tag{5.10}$$

where ω = fraction of binder mass that is polymer

V_{pb} = volume of polymer printed in binder (cm^3).

The mass of polymer delivered in the binder is given by

$$M_{pb} = (\beta)(\omega)L\rho_b \tag{5.11}$$

where ρ_b = binder density (g/cm^3)

M_{pb} = mass of polymer delivered in binder (g)

The total amount of polymer incorporated in the feature is the sum of the polymer incorporated from the powder bed and the polymer in the binder. This total mass, given by the summation of Equations 5.9 and 5.11, is

$$M_{tot} = \beta L\left(\frac{\rho_o \rho_p}{S(\rho_p - \rho_o)} + (\omega)\rho_b\right) \tag{5.12}$$

where M_{tot} = total polymer mass in line (g).

The volume that this mass of polymer occupies is dependent on the final density of the line. This volume is given by

$$V_{tot} = \frac{\beta L\left(\frac{\rho_o \rho_p}{S(\rho_p - \rho_o)} + (\omega)\rho_b\right)}{\rho_f} \tag{5.13}$$

where V_{tot} = volume occupied by all polymer (cm^3)

ρ_f = final line primitive density (g/cm^3).

The volume of a cylindrical line is given by equation 5.1. As a result, the final diameter of a line defined by the total polymer volume and the final line density is given by

$$D_f = \left[\left(\frac{4}{\pi\rho_f}\right)\left(\frac{\rho_o \rho_p}{S(\rho_p - \rho_o)} + (\omega)\rho_b\right)\right]^{1/2} \beta^{1/2} \tag{5.14}$$

where D_f = final line diameter (cm).

The complexity of Equation 5.14 can easily be reduced in some cases. For example, when binders that contain no polymeric or other structural material are used, the second term of the equation is eliminated because $\omega = 0$. The line primitive feature size equation for 100% solvent binders is given by

$$D_f = M\beta^{1/2} \tag{5.15}$$

where

$$M = \left[\frac{4 \rho_o \rho_p}{\pi \rho_f S (\rho_p - \rho_o)} \right]^{1/2} \quad . \tag{5.16}$$

Equations 5.14 and 5.15 contain five or six parameters for determining the final diameter of a printed line primitive. Four of these, binder per unit line length, binder polymer mass fraction, powder bed tap density, and the solid polymer density, are easily measured. The other two, final line density and saturation, are more difficult to determine. The line density could be determined by cross-sectioning and calculating the density of each line or by using a technique such as mercury porosimetry to determine the density. Either approach would require a very large amount of data to achieve an accurate density. Saturation could be determined by observing the migration of binder in the powder bed. This would be difficult to observe prior to solvent evaporation given the high volatility of the solvents used in this work.

These equations can also be used to generate theoretical data for line primitive feature size. This information can then be compared to the experimental data described in the previous section. Such a comparison may be useful to determine some of the physical parameters, such as saturation and final line density, inherent to a given set of experimental printing conditions.

6. ANALYSIS OF EXPERIMENTAL LINE PRIMITIVE FEATURE SIZE DATA

The theoretical line primitive feature size can be determined for a given printing scenario using the equations derived in Chapter 5. Where experimental values for the saturation and final line density are unknown, the experimental feature size results can be compared to the theoretical data in order to estimate these parameters. This information may provide some insight into the processes occurring during printing, dissolution, and evaporation.

Line Primitives from Pure Solvent Binders

75-150 μm Polycaprolactone

Equation 5.15 relates the line primitive feature size to the binder delivered for line primitives fabricated using 100% solvent binders. Theoretical feature size data can be generated using a constant value of M (the slope) and various binder per unit line length levels. Each theoretical value of M refers to a "family" of saturation and final line density pairs. As mentioned, saturation and final line density have not been experimentally determined in this work, but theoretical data can be used to bracket the possible experimental values.

A few simple examples illustrate what is indicated by a particular value of the slope M. Table 6.1 shows the possible saturation-density pairs for the slope M = 1.55 in Equation 5.16. This condition corresponds to a line with a density equal to that of the powder bed (0.41 g/cm^3 for 75-150 μm PCL from Table 3.1) printed at a saturation of 1. Such a density could be obtained if the binder did not dissolve the powder bed material. It is unlikely that complete saturation could be achieved based on extensive work with (non-dissolving) ceramic powders.

However, this slope fits several other saturation-density pairs. The slope M = 1.55 also corresponds to a line with a final density almost four times the theoretical solid polymer density and a saturation as low as 0.1, as well as several other "intermediate" values for saturation and final line density, as shown in Table 6.1. The viable saturation-density combinations can be bounded by considering some limitations on the final line density. Final line densities above the theoretical solid polymer density (1.1 g/cm^3 for PCL) or below the powder bed tap density are not obtainable. The viable combinations can be further limited by qualitative examination of the printed line morphologies. Individual particles visible within a contiguous line imply a line density close to the powder tap density. Conversely, a line composed of more completely dissolved particles that are not individually distinguishable within the line would have a density much closer to the theoretical solid density.

While it would be difficult to predict the precise theoretical M values that the experimental data will follow, the qualitative saturation and final line density behavior can be anticipated. At low binder per unit line length levels, both parameters will be low; saturations less than 0.5 and final line densities close to the powder bed tap density are expected. In this regime, little binder is being delivered, so extensive particle dissolution will not occur. The density of particles arranged in such a line will not be much different from in the powder bed. The presence of largely undissolved particles on line surfaces will force saturation down to low values. At high binder per unit line lengths, saturation and final line density will reach constant values, as is observed for other 3D Printing investigations. Sufficient binder is delivered in this regime to more completely dissolve particles. Some maximum final line density value less then the theoretical solid density will be reached. A maximum saturation will be achieved and maintained for all succeeding binder levels. Once the maximum values for these parameters are obtained, the feature size will depend only on the amount of binder

delivered to the powder bed. In between these two regimes, saturation and final line density are expected to increase as the binder per unit line lengths levels increase.

Table 6.1 Possible values for saturation and final line density for M = 1.55 (in Equation 5.15)

Saturation	Final Line Density (g/cm^3)
1	0.41
0.9	0.45
0.8	0.51
0.7	0.58
0.6	0.68
0.5	0.81
0.4	1.01
0.3	1.35
0.2	2.03
0.1	4.05

Figure 6.1 shows theoretically- and experimentally-determined feature sizes for 75-150 μm PCL powder and the 100% chloroform binder at several binder delivery levels. It is apparent that the experimental data do not follow a single theoretical line. As predicted, saturation and final line density do not remain constant over all binder delivery levels. Instead, the data follow a line with a particular slope at low binder per unit line length levels (about 2.0×10^{-4} cm^3/cm and less). For this powder and binder, the experimental data follow a theoretical

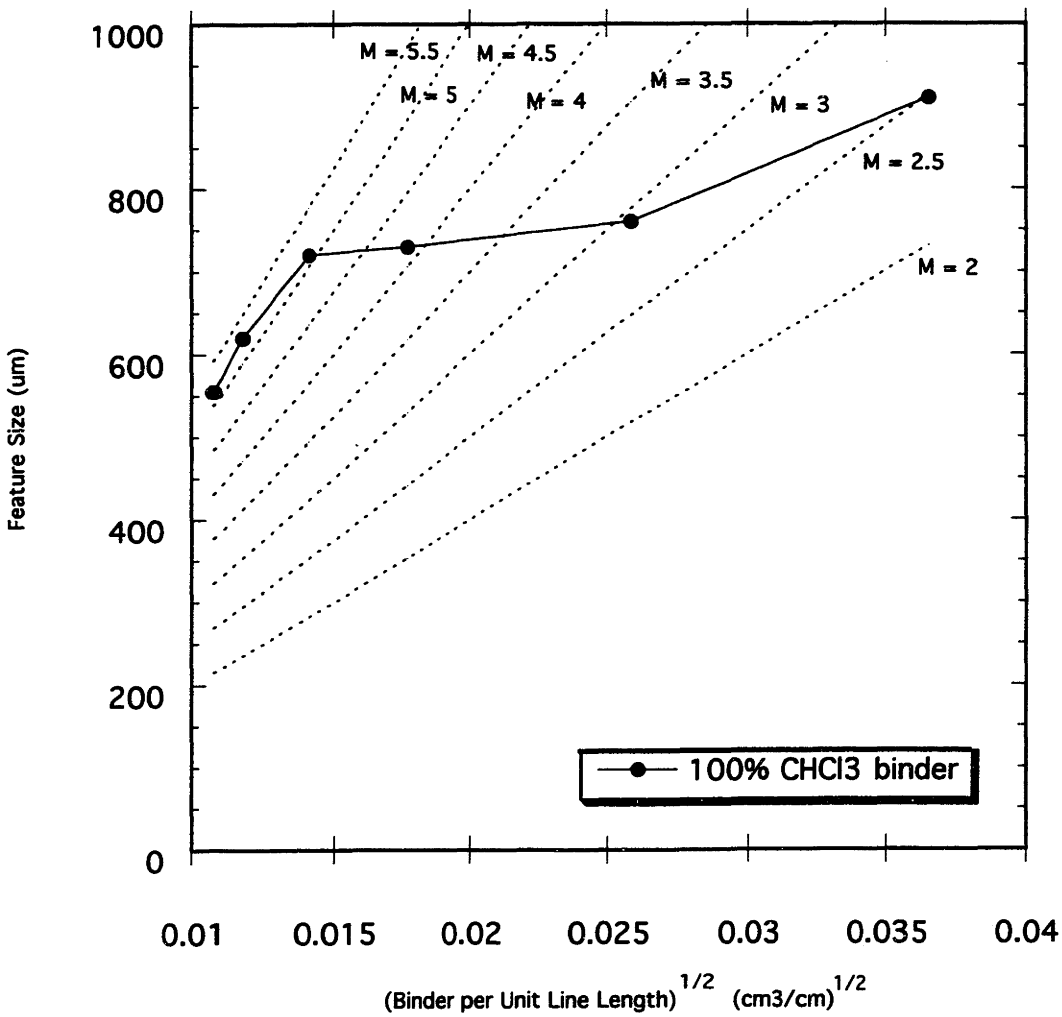

Figure 6.1 Theoretical and experimental line primitive feature size data for 75-150 um PCL using 100% chloroform binder

line with slope ~ 5.0 very closely in this low binder delivery regime. A transition occurs at intermediate binder per unit line length levels (about 2.0 - 8.0 x 10^{-4} cm^3/cm), as the experimental data intersect several theoretical lines. At higher binder per unit line length levels (about 8.0 x 10^{-4} cm^3/cm and greater), the experimental data then follow a second theoretical line with a lower slope. The experimental data follow another line (perhaps slope ~ 2.5) closely in this binder regime.

Table 6.2 shows the possible density/saturation combinations for lines with various slopes M printed on 75-150 μm PCL. This information is similar for other powder sizes and types, but it varies slightly since powder bed tap density and theoretical solid polymer density are included in the slope, as shown in Equation 5.16. Experimental data following a theoretical line with a slope = 5.0 would have a final line density approximately equal to the powder tap density and a saturation less than 0.1. The high binder per unit line length data approaching the theoretical line with a slope = 2.5 would have a saturation between 0.1 and 0.4 and a line density between the powder bed tap density and the theoretical polymer density.

Low binder saturation and low final line density were anticipated at low binder per unit line length levels because the small amount of binder being printed would not be able to fully dissolve the 75-150 μm powder particles. Individual particles should be apparent within a line printed at those saturation and final line density levels. Figure 6.2 shows a line printed in this binder per unit line length regime. The individual particles visible in the line reflect this anticipated line structure. A change in the slope of the experimental data is observed for the intermediate binder per unit line length levels. This shift could be due to variations in final line density and saturation, which were expected to increase with a higher amount of binder being delivered. Increases in these parameters would reduce the slope of data according to Equation 5.16. At the high binder per

unit line length levels, the experimental data follow a different theoretical line. This behavior corresponds to saturation and final line density reaching constant values, as predicted. The increase in feature size may depend on the increasing binder delivery (increasing binder per unit line length) alone. The comparison of theoretical and experimental data coincide well with the predicted qualitative saturation and final line density behavior.

Table 6.2 Viable final line densities (g/cm^3) for several slopes M and saturations for 75-150 μm PCL (powder tap density = 0.41 g/cm^3, PCL solid density =1.1 g/cm^3)

	Slope M								
Saturation	5.5	5.0	4.5	4.0	3.5	3.0	2.5	2.0	1.5
S = 1									0.37
S = 0.9									**0.41**
S = 0.8									**0.46**
S = 0.7									**0.52**
S = 0.6								0.35	**0.62**
S = 0.5								**0.42**	**0.74**
S = 0.4							0.33	**0.52**	**0.92**
S = 0.3						0.31	**0.44**	**0.69**	1.23
S = 0.2			0.24	0.30	0.34	**0.46**	**0.67**	**1.04**	1.84
S = 0.1		0.32	0.33	**0.41**	**0.52**	**0.68**	**0.92**	1.33	2.43
S = 0.05	**0.55**	**0.67**	**0.82**	**1.04**	1.36	2.16			

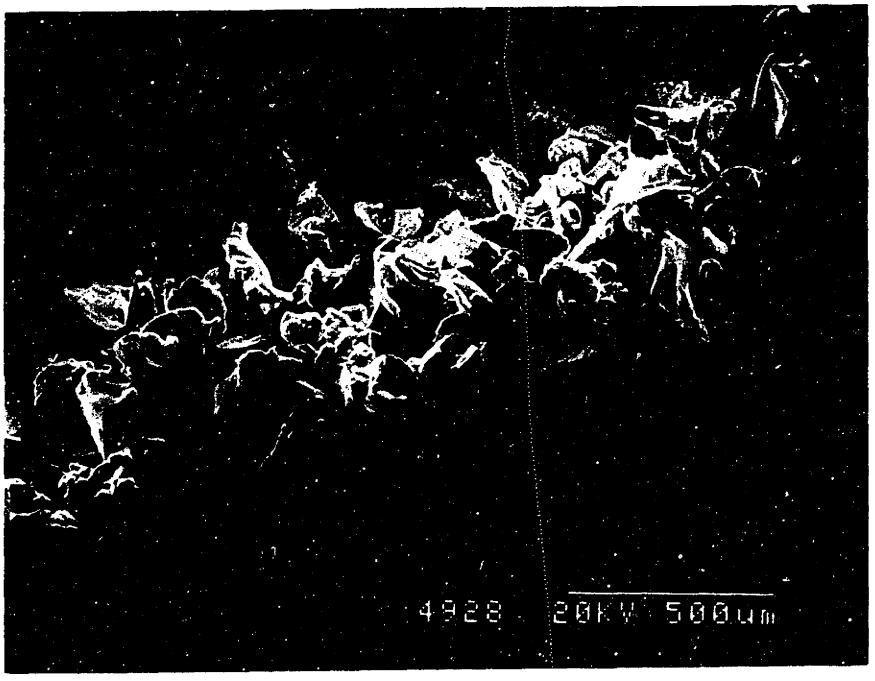

Figure 6.2 Single line primitive fabricated from 75-150 um PCL in the low binder per unit line length regime

The saturation and final line density conditions associated with these theoretical slopes can be realistically obtained. Table 6.2 shows that final line densities between the powder bed tap density and the theoretical polymer density are achieved for the observed slopes according to Equation 5.16. The possible saturations for these printing conditions as shown in Table 6.2 are also viable, but they are much lower than anticipated. Experiments with other 3D Printing materials have generally indicated a saturation in the 0.6-0.8 range.

These lower-than-expected saturations can be explained by considering the unique binder-powder interaction for this system. The powder bed particles are dissolved during the printing process to achieve particle-to-particle bonding. The dissolution of material makes it possible to incorporate particles in a feature that are only partially exposed to binder. The volume surrounding partially dissolved

surface particles is included in the volume available to binder even though the binders will never reach that space. This volume would not be a part of the available volume for other bonding mechanisms because more complete exposure of binder to the particle surface area would be necessary to bond those particles. As a result, saturation is necessarily lower for this dissolution bonding mechanism relative to a mechanism in which particles are held in place by gelation.

This concept is illustrated in Figures 6.3a and 6.3b. Two as-printed (prior to binder evaporation) line primitive cross sections are shown. Figure 6.3a shows a "ceramic-like" line with a smooth surface and no adherent particles. For simplicity, saturation is illustrated here as 100%. Saturation is more typically 60-80%, with the rest of the volume being empty void space distributed throughout the primitive. Figure 6.3b shows a polymer type line printed with the same amount of binder. Numerous partially dissolved adherent particles on the surface are apparent. These particles are only partially contacted by binder. Even though this line contains the same amount of binder as the line in Figure 6.3a, the saturation levels are different. The available volume is determined from the line primitive feature size and it is much greater for the polymer line than a comparable ceramic line. Since the same amount of binder is printed in each case, a higher fraction of the available volume in Figure 6.3a is filled with binder. The volume surrounding the partially dissolved particles in Figure 6.3b is included in the volume of the line and, therefore, must be included in the void volume, even though no binder ever contacted this portion of the powder bed. Thus, for polymeric/dissolving powder systems, the defined available volume is shifted to a higher value for the same volume of binder delivered, so saturation is necessarily lower. Similarly, lines printed with 75-150 μm powder are expected to have a lower saturation than comparable lines printed with 45-75 μm powder because the larger particles on the line surface increase the line diameter, and therefore the total available volume, more than the smaller particles.

a. "Ceramic" Line Primitive with High Saturation

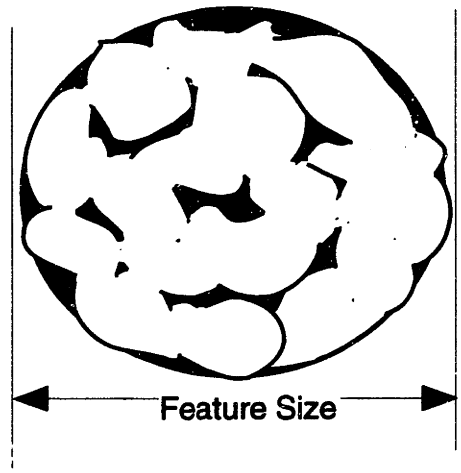

b. Polymer Line Primitive with Low Saturation

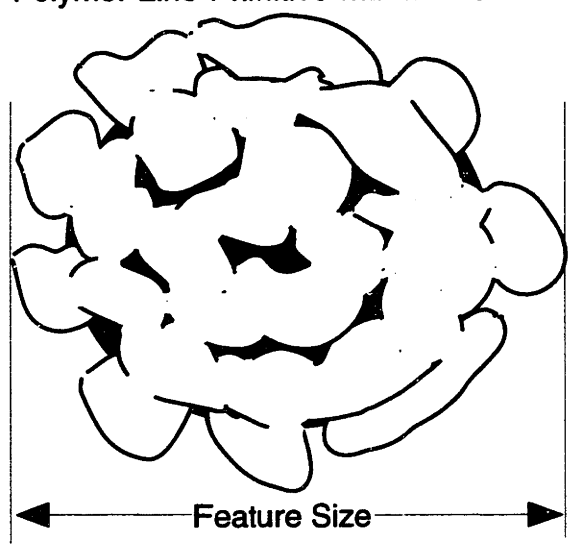

Figure 6.3 Unique saturation levels for different binder mechanisms and the same binder per unit line length level

45-75 μm Polycaprolactone

The theoretical equation derived in Chapter 5 can be used to describe lines fabricated with PCL powder in the 75-150 μm range. Other powders must be considered to determine if this theory describes polymeric lines formed by 3D Printing in general. Similar behavior of the experimental data and possible values for saturation and final line density are predicted. Figure 6.4 shows the theoretical and experimental feature sizes for the 100% chloroform binder printed on 45-75 μm PCL. This set of experimental data for all cases does not follow a single theoretical line. As with the 75-150 μm PCL powder, the experimental data follow the M = 2 theoretical line at low binder per unit line length levels. A transition over several theoretical lines occurs through the intermediate binder per unit line length levels. At higher binder per unit line length levels, the experimental data then approach a line with slope 1-1.5.

The slopes of the theoretical PCL lines followed by the experimental 100% solvent binder data are lower for the 45-75 μm PCL powder experiments relative to those for the 75-150 μm PCL experiments. As the smaller powder particles are more easily dissolved in the binder than the larger particles, a higher final line density can be achieved. The smaller adherent particles on line primitive surfaces when using the 45-75 μm powder may result in a higher saturation of the printed region by the binder, as described earlier. Higher values for these two parameters relative to those for the 75-150 μm experiments result in the lower theoretical slope.

More complete powder dissolution is apparent in the morphology of lines printed using 45-75 μm PCL powder. Figure 6.5 shows a line primitive printed using 45-75 μm PCL powder at the same binder per unit line length level as the 75-150 μm PCL sample shown in Figure 6.2. Individual particles are

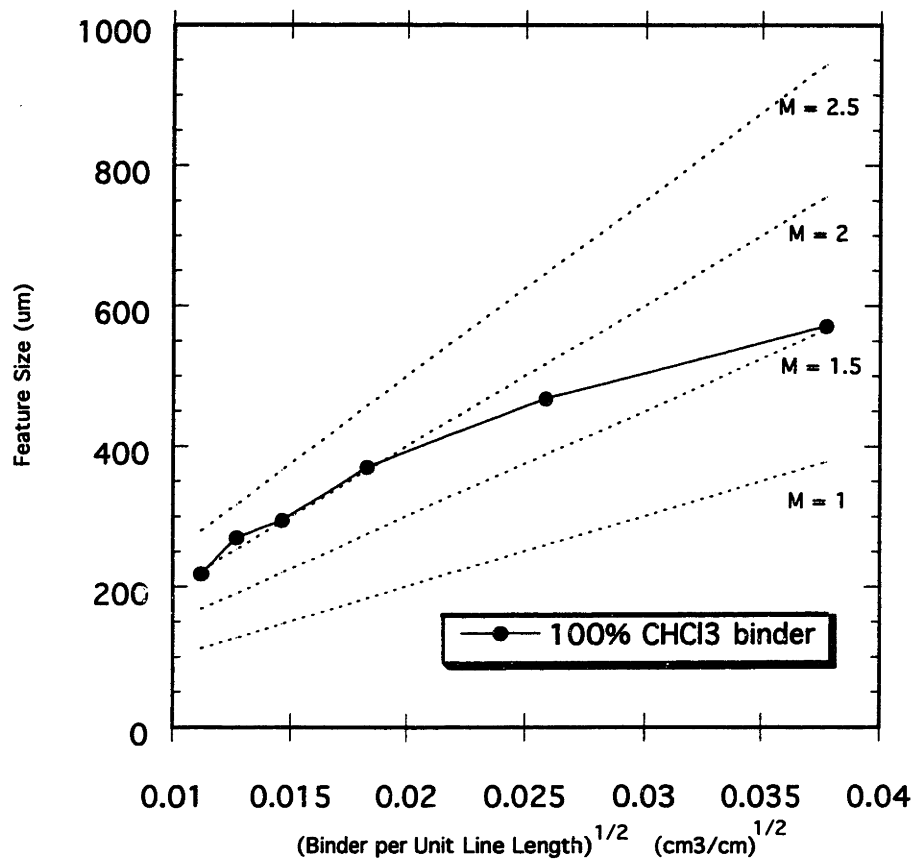

Figure 6.4 Theoretical and experimental line primitive feature size data for 45-75 um PCL using the 100% chloroform binder

distinguishable only on some portions of the line surface. The center core of the line is composed of polymer that appears to have been almost fully dissolved by the binder. Figure 6.6 shows a line printed with 45-75 μm PCL powder in the higher binder delivery regime that demonstrates the more complete powder dissolution expected for high binder delivery levels. The line is almost completely smooth with few adherent partially dissolved powder particles. The center of the line is composed of fully dissolved and recast polymer. No residual powder structure is visible.

Poly(Lactic Acid)

The behavior of PLA is expected to parallel that PCL; indeed, data for lines printed with 75-150 μm PLA powder resembles that for the corresponding PCL powder. As shown in Figure 6.7, data for 75-150 μm PLA powder follow the theoretical line with slope ~ 3.5-4. After a transition across several theoretical lines for intermediate binder delivery levels, the experimental data for high binder per unit line length levels follow the theoretical line with slope ~ 2. The slopes of the theoretical lines followed by the experimental data are similar to those determined for the PCL case (~ 5.0 at low binder per unit line length and ~ 2.5 at high binder per unit line length). Less particle dissolution (and, therefore, a lower final line density and a higher slope) was anticipated due to the higher molecular weight and slower dissolution of the PLA. Since powder dissolution for this particle size is relatively slow, differences in dissolution between the two powder types may not be apparent. These results are reasonable morphologically for the lines created. The line fabricated with the low binder delivery regime (shown in Figure 6.8) is similar in morphology to the line constructed from 75-150 μm PCL at a comparable binder delivery level (as shown in Figure 6.2). The particles in

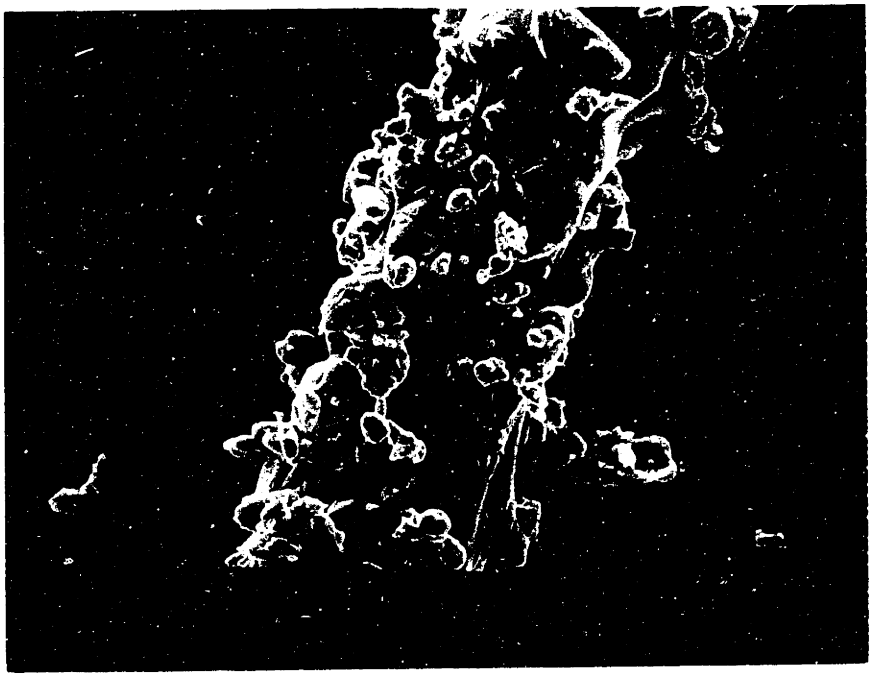

Figure 6.5 Single line primitive fabricated from 45-75 um PCL in the low binder per unit line length regime

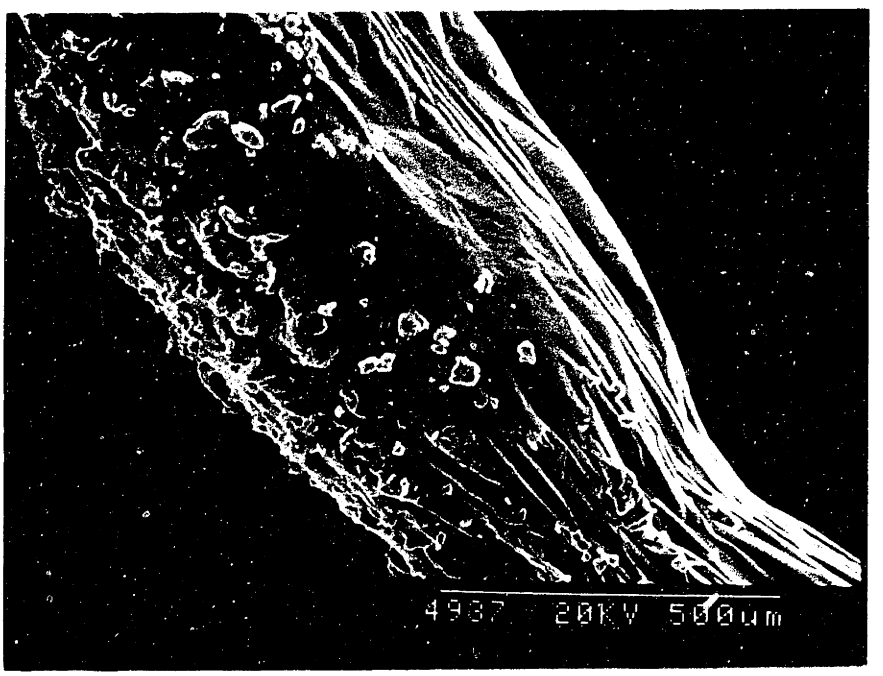

Figure 6.6 Single line primitive fabricated from 45-75 um PCL in the high binder per unit line length regime

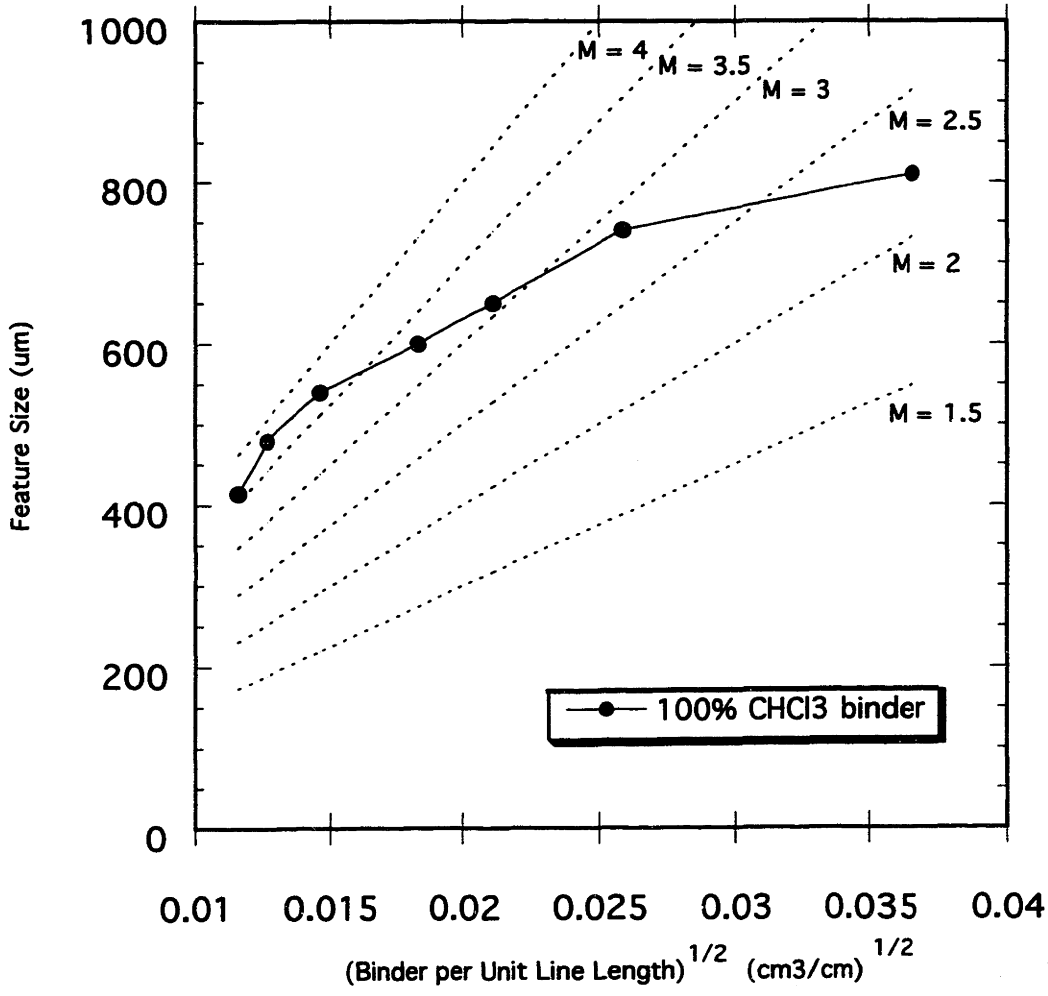

Figure 6.7 Theoretical and experimental line primitive feature size data for 75-150 um PLA using the 100% chloroform binder

this line are slightly less dissolved than those in the high binder per unit line length primitive (Figure 6.9).

The comparison of experimental data with theory for the 45-75 μm PLA powder is shown in Figure 6.10. The experimental data for low binder per unit line length levels appear to follow a line with a slope ~ 2.5, while the high binder delivery data closely follow the theoretical line with slope = 1.5. The slopes of these theoretical lines are slightly higher than the corresponding PCL lines. Given the higher molecular weight of PLA, less dissolution, as previously described, might be expected in the process of printing. As opposed to the larger 75-150 μm powders discussed above, powders of this size dissolve fast enough that differences between the PLA and PCL powders are noticeable. The slower polymer dissolution for PLA case decreases the final line density, so the experimental data follow a more steeply-sloped theoretical line than the data for the same size PCL powder.

A small decrease in feature size is observed in the transition through the intermediate binder per unit line length delivery levels. All other experimental data sets showed a leveling-off in feature size data in this region. The decrease is within experimental error (as shown in Figure 4.10), but such a result is nonetheless conceivable. Line primitive feature size is affected by saturation, final line density, and binder per unit line length delivered, as indicated theoretically in Equation 5.15. Increasing saturation and/or increasing final line density will decrease feature size, while increasing binder delivery will increase the size of the feature. The magnitude of the decrease due to saturation and final line density changes may be greater than the increase due to higher binder delivery levels, resulting in the overall net decrease in experimental feature size data.

As with the PCL powder, the slopes of the theoretical lines followed by PLA experimental data at binder per unit line lengths less than 2.0×10^{-4} cm^3/cm and greater than 8.0×10^{-4} cm^3/cm are lower for the 45-75 μm powder relative to

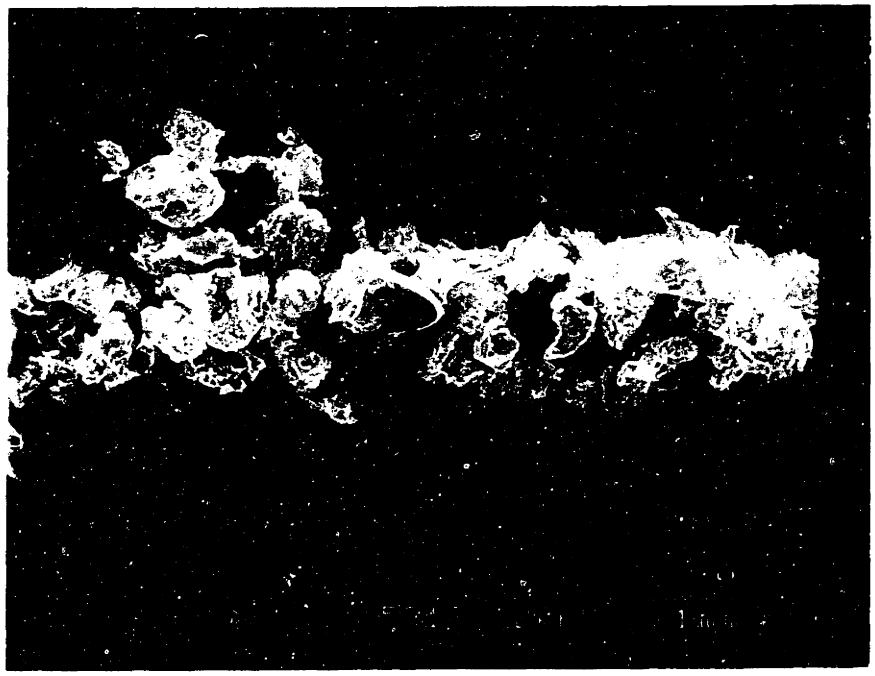

Figure 6.8 Single line primitive fabricated from 75-150 um PLA in the low binder per unit line length regime

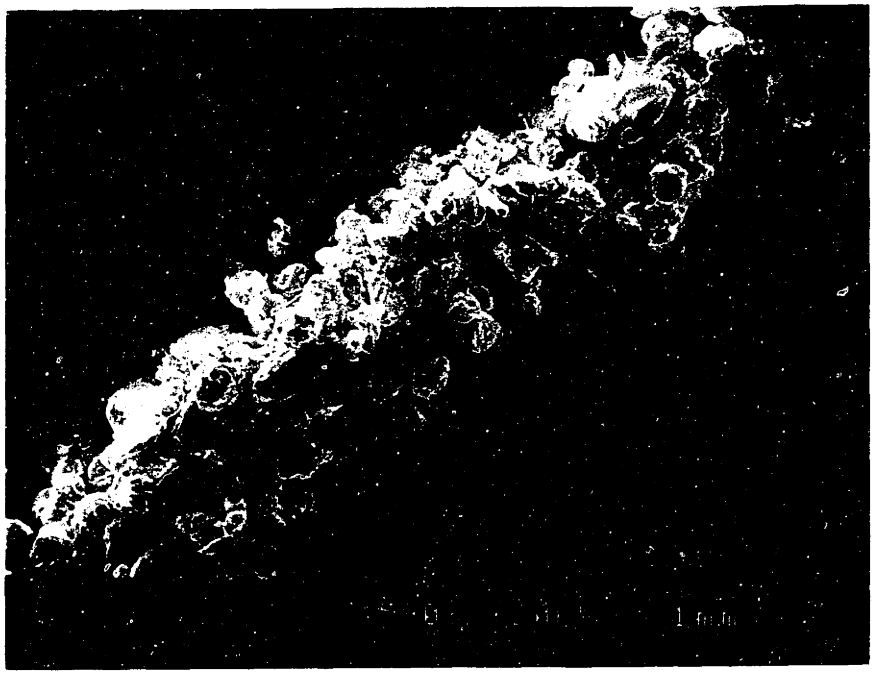

Figure 6.9 Single line primitive fabricated from 75-150 um PLA in the high binder per unit line length regime

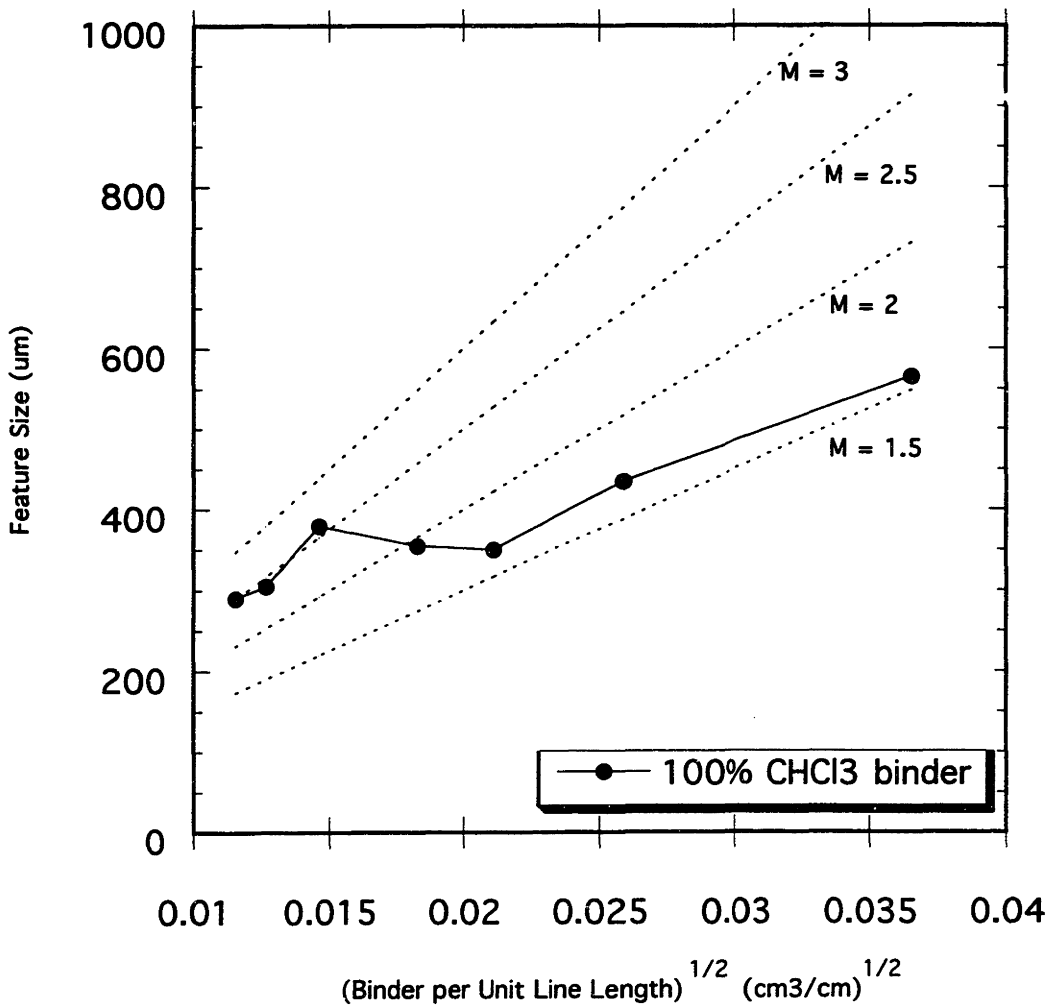

Figure 6.10 Theoretical and experimental line primitive feature size data for 45-75 um PLA using the 100% chloroform binder

the 75-150 μm powder. Lines printed with the 45-75 μm powders achieve a higher density than the lines printed with the 75-150 μm powders due to rapid powder dissolution. Also, the use of smaller powder particles results in a higher saturation of the printed region, as discussed previously. Higher saturation and final line density result in a smaller value of the slope M that is followed by the experimental data.

Line Primitives from Polymeric Solution Binders

A similar analysis for primitives printed with the polymeric solution binders is more involved. The inclusion of a polymeric component in the binder necessitates the use of Equation 5.14 (ω does not equal zero for these binders) to describe the line primitive feature size. This equation captures the impact of the polymeric binder component on feature size. A larger feature size for line primitives fabricated using a polymeric solution binder and the 45-75 μm PCL powder relative to lines printed using a solvent-only binder and the same powder is predicted from Equation 5.14 due the polymer component of the binder. A slightly larger line primitive feature size is observed when using a 10 wt% PCL in chloroform binder relative to a 100% chloroform binder and printing on 45-75 μm PCL powder, as shown in Figure 4.5.

The line primitive feature size for the 100% solvent binder is significantly larger than for polymeric solution binders printed on the 75-150 μm PCL powder, as shown in the experimental data in Figure 4.4. More partially dissolved particles would be bound to lines fabricated using the 100% solvent binder since more polymer could be dissolved in that binder relative to a binder that initially contained polymeric material. This phenomenon would increase the defined volume of the line, which would decrease the saturation achieved in printing that line, as discussed. A lower saturation would result in a larger feature size, as

indicated by the derived theoretical Equation 5.14. A similar effect in not seen with the smaller powder sizes due to the rapid and easy dissolution of those powder particles.

The same general behavior for line primitive feature size data observed for lines printed with solvent binders is anticipated for lines printed with polymeric solution binders. Low saturation and final line density are expected at low binder per unit line length levels. After a transition region for increasing values of both parameters, the data should follow a theoretical line at high binder per unit line length levels.

Figure 6.11 shows a comparison of experimental data and theoretical data generated using Equation 5.14 for 75-150 μm PCL powder using a 10 wt% PCL in chloroform binder. As with the pure solvent binders, the experimental data follow a theoretical line at low binder per unit line lengths (about slope = 3). The data then shift across several theoretical lines for intermediate binder delivery levels and follow a second theoretical line at high binder per unit line lengths (slope slightly less than 2). Note that the slopes of the theoretical lines can not be directly compared with M values for the pure solvent lines, as they are calculated using different equations. Figure 6.12 shows a similar comparison for a 26.5 wt% acid-modified PCL in chloroform binder. A comparable experimental data pattern is visible, although less apparent. At low binder delivery levels, the data are located around the theoretical line with slope = 3.5. For high binder delivery levels, the data approach a line with a slope between 1.5 and 2. The slopes of these lines are slightly higher than those for the 10 wt% PCL case due to the higher amount of polymer in the binder (increasing ω in Equation 5.14).

Figure 6.13 shows a comparison of experimental and theoretical data for a 10 wt% PCL in chloroform binder printed on 45-75 μm PCL powder. The data follow the theoretical line with a slope = 2-2.5 for low binder per unit line lengths. The high binder per unit line length data appear to be approaching a theoretical

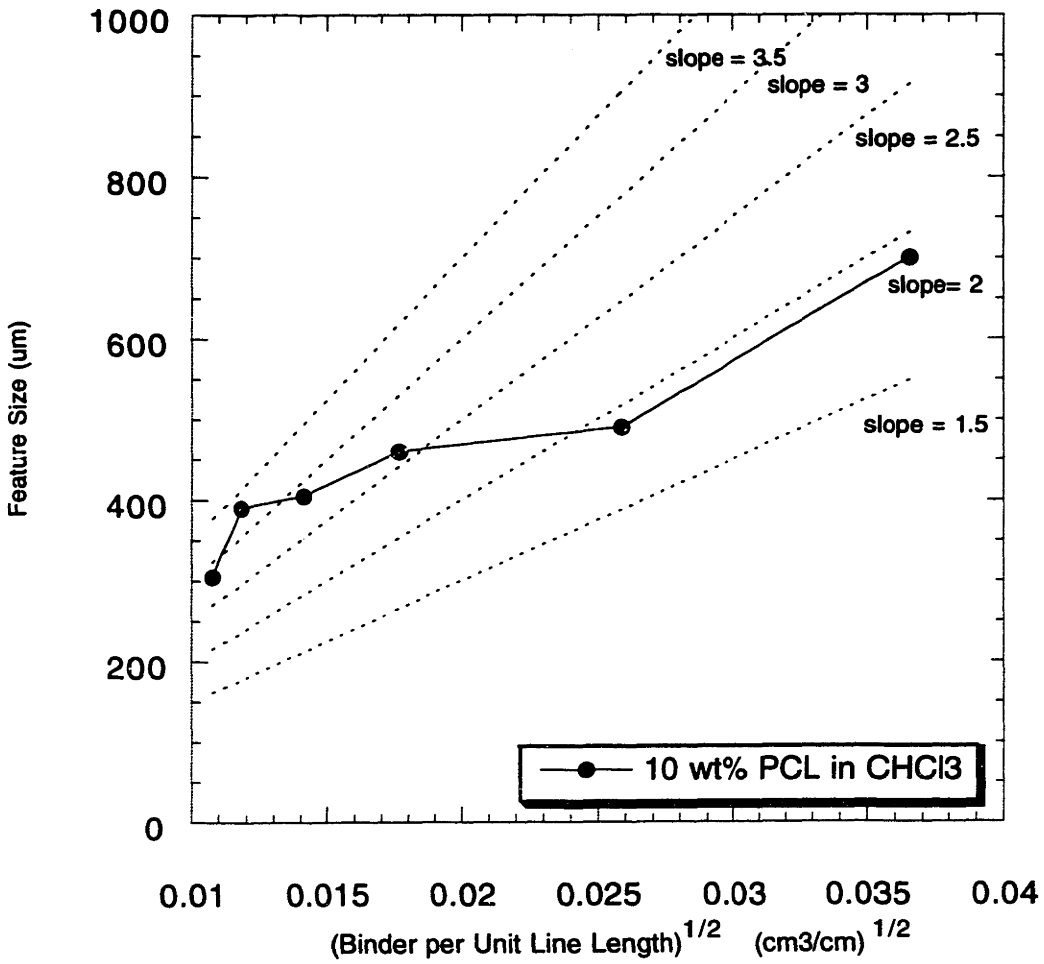

Figure 6.11 Theoretical and experimental line primitive feature size data for 75-150 um PCL using the 10 wt% PCL in chloroform binder

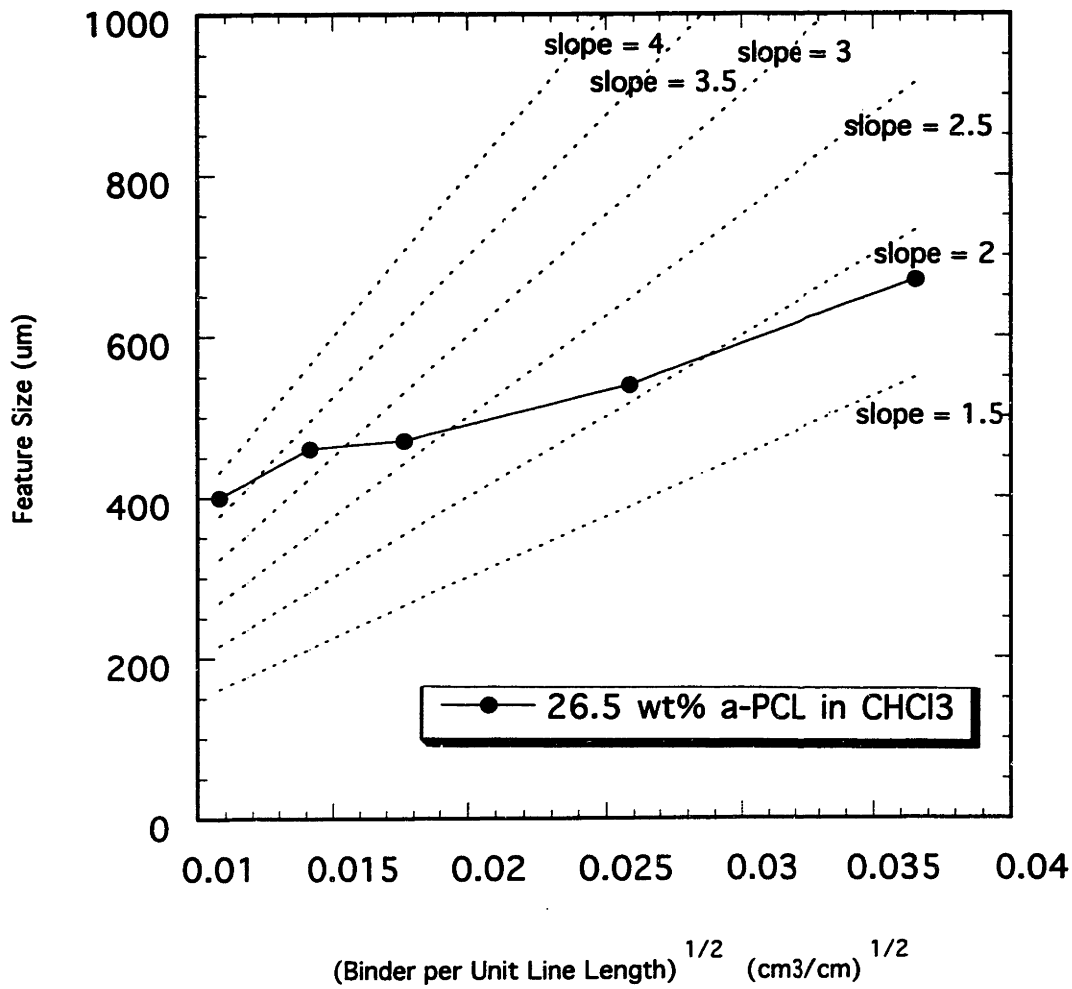

Figure 6.12 Theoretical and experimental line primitive feature size data for 75-150 um PCL using the 26.5 wt% acid-modified PCL in chloroform binder

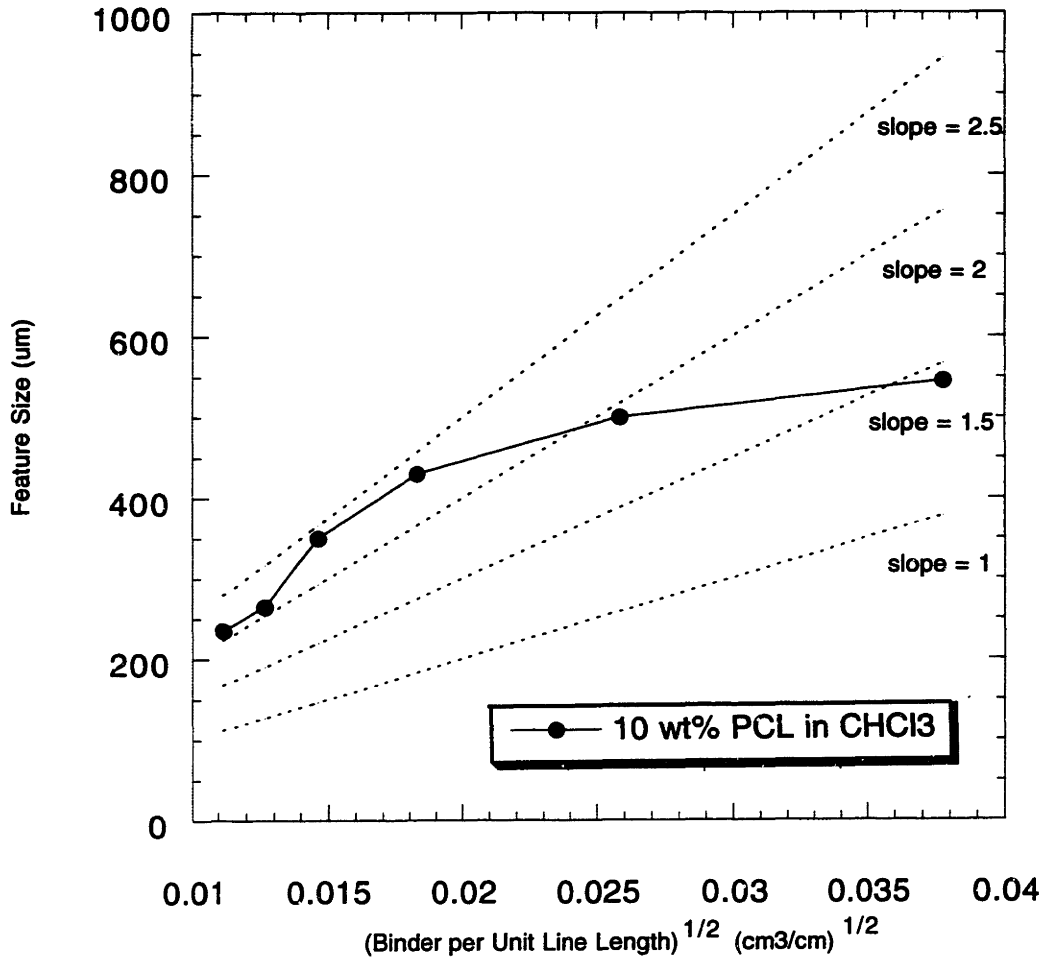

Figure 6.13 Theoretical and experimental line primitive feature size for 45-75 um PCL using the 10 wt% PCL in chloroform binder

line with slope ~ 1.5. Between these two regimes, the experimental data shift across several different sloping lines.

Discussion

The experimental data follow a similar pattern for several different powder size, powder composition, and binder composition combinations. The 100% solvent binder data follow a constant slope theoretical line at binder per unit line length delivery levels less than 2.0×10^{-4} cm^3/cm and a different constant slope theoretical line at binder delivery levels greater than 8.0×10^{-4} cm^3/cm. These patterns reflect either constant values for the saturation and final line density achieved during printing or a scenario in which an increase in one of those quantities is compensated by a similar decrease in the other parameter to produce a constant value for the data slope, as reflected in the theoretical equations 5.14 and 5.15. Either of these conditions is possible, but experimental measurement of the two parameters would be necessary to determine which is occurring in practice. The low binder delivery behavior is not as clearly defined the polymeric solution binder data. Other variables (saturation and final line density) are changing with binder per unit line length for the low and intermediate binder delivery regimes. Only at high binder deliveries do these data follow a constant properties theoretical line.

The behavior above 8.0×10^{-4} cm^3/cm is predicted since the saturation and final line density reach the maximum possible values, as described earlier. Increases in line primitive feature size at higher binder per unit line length levels are perhaps driven by the increasing binder delivery alone. Such a transition roughly corresponds to the transition in line primitive feature size observed for ceramic materials that occurs when maximum saturation is achieved.

The transition from the low binder per unit line length regime to the intermediate regime is more difficult to explain. There is no corresponding transition for other materials systems investigated. In addition, this shift occurs at about the same binder per unit line length level (about 2 x 10^{-4} cm^3/cm) for all types and sizes of powders with the 100% solvent binders, but this transition in not apparent for polymeric solution binders. Understanding why the transition occurs at this level and why saturation and final line density are constant (or they compensate for changes in each other) might deliver some added insight into the mechanisms of powder birding.

This transition must be independent of powder particle size, powder type, and binder composition, as it occurs around a specific binder per unit line length delivery level (2.0 x 10^{-4} cm^3/cm) for all printing conditions. At this level, binder drops may begin to overlap in the powder bed. At lower binder delivery levels, the binder drops may land in discrete locations in the powder bed and form contiguous features via capillary migration of the binder in the powder bed. Low capillary migration could produce the discontinuous lines observed and discussed in Chapter 4.

The spacing (distance/drop) between the binder drops as they are delivered to the powder bed is the ratio of the printhead speed (distance/sec) to number of drops that are generated per second (drop frequency or drops/sec)). The natural drop frequency is determined in Appendix A, Equation A-4. Table 6.3 shows the droplet spacing for several printhead speeds.

The size of the binder drops must be calculated in order to determine if they overlap and, if they do not, the space between them. The size of a drop for an orifice of 45 μm at the natural drop frequency of chloroform is derived in Appendix A. Equation A-7 indicates that the drop size (drop diameter) for these conditions is 86.4 μm. This drop size is much larger than all of the drop spacings

shown in Table 6.3. This indicates that there is some overlap of binder drops for all printing conditions.

Table 6.3 Droplet spacings for various printhead speeds for a droplet delivery rate of 46,850 droplets/sec

Printhead Speed (in/sec)	Binder Droplet Spacing (μm/drop)
50	27
41.67	23
31.25	17
20	11
10	5
5	3

This calculation does not account for solvent evaporation from the binder drops. A portion of the binder solvent may evaporate during delivery to the powder bed, resulting in a smaller drop size at the powder bed surface. Solution of the time-dependent heat and mass transfer equations is difficult. However, upper and lower bounds on the drop size can be easily calculated by assuming the drop evaporates at a steady state temperature. An upper bound (largest drop size) is obtained if this temperature is the wet bulb temperature. The binder drops begin to evaporate as they fall to the powder bed. With evaporation, the drop will cool and the amount of evaporation that occurs will decrease. The equilibrium temperature of the binder droplet, called the wet bulb temperature, is -14.5 °C for chloroform drops, as derived in Appendix B. A lower bound (smallest possible drop size) is obtained if the steady state temperature is room

temperature. If evaporative cooling is neglected, evaporation can be considered to occur at room temperature throughout the process.

Neither of these cases is reflective the true experimental conditions. The calculations in Appendix D indicate that the time to reach the wet bulb temperature is comparable to the time for the droplet to be delivered to the powder bed. Therefore, binder solvent evaporation occurs over a temperature range from room temperature to the wet bulb temperature during delivery to the powder bed. These steady state calculations serve as simple and useful bounds on the size of the binder droplets when they impact the powder bed.

The calculations to determine the size of a binder drop at the surface of the powder bed are discussed in Appendix C. If steady state evaporation is considered to occur at the wet bulb temperature, the binder drop will decrease in diameter from 86.4 μm to 84.0 μm (an 8% decrease in volume) in falling from the printhead to the powder bed. For the most significant case of binder evaporation (steady state evaporation at room temperature), the binder drop diameter will decrease to 67 μm (a 53% decrease in volume) during binder delivery. Thus, even for the worst case of solvent evaporation, the diameter of binder drops will be much larger than the drop-to-drop spacings shown in Table 6.3. As a result, the onset of binder drop overlap does not appear to be the cause for the transition in the experimental data observed.

The distribution of drops in the jet could impact feature size formation. As mentioned in Chapter 3, the Pre-Proto 3D Printing machine is not outfitted with the electronics or piezoelectric devices necessary to generate uniform binder drops. Drop formation for 100% chloroform binders was examined. The "natural" binder stream is composed of highly non-uniform drops ranging in size from 60-110 μm. The average drop diameter is 70-80 μm, comparable to the theoretical drop diameters determined in Appendix C. Also, the jet breakoff distance without piezoelectric devices used to generate drops varies significantly.

The jet breakoff distance is the location downstream from the orifice at which point individual droplets are formed. Finally, the spacing between drops is not uniform by the time the drops impact the powder bed. Neighboring drops are observed to merge at distances less than the distance to the powder bed surface. This results in the formation of "superdrops" and "blank" spaces in the binder jet.

This examination explains some of the phenomena observed in fabricating single line primitives. The formation of line segments (rather than contiguous lines) observed at binder per unit line length delivery levels 2.0×10^{-4} cm^3/cm and less is due to this non-uniform drop spacing. Gaps in the binder jet translate into gaps in the printed line in the powder bed. This is not observed at higher binder delivery levels because these discontinuities are "filled in" by the larger number of drops and more total binder volume delivered in those cases. This problem was originally attributed to printing on low tap density powders. However, these results indicate that printing onto lower tap density powders may still be possible using a controlled binder jet. In addition, the low binder per unit line length behavior for experimental line primitive feature size/binder per unit line length data is likely also due to this non-uniform distribution of drops in the binder jet. Printing with uniformly-spaced drops generated using a piezoelectric device on the printhead will probably smooth or even eliminate this transition in the data. Indeed, the low binder level behavior is not observed for the polymeric solution binders. Individual drops are not formed without piezos using these binders. Without discrete drop formation, those binder jets are probably relatively uniform.

Lines created by 3D Printing can be described using the models in Equations 5.14 and 5.15. One set of apparently anomalous data can also be explained. Experiments in which a 100% chloroform binder was printed on both 45-75 μm and 75-150 μm PCL with a binder flow rate 2.3-2.4 g/min resulted in a

line primitive feature size 20-40% larger than those printed with a "typical" binder flow rate of 1.3-1.5 g/min, as shown in Figure 6.14. As defined above, the binder per unit line length measurement accounts for variations in binder flow rate and printhead speed that impact the amount of binder delivered to the powder bed. A shift in either parameter would result in a commensurate shift in binder per unit line length delivered. Only a modest shift in line primitive feature size would be expected from the change in flow rate for the experimental set-up described above and, therefore, binder per unit line length.

A higher binder flow rate may be offset by a higher printhead speed to yield the same binder per unit line length for two different printing scenarios. In fact, many of the binder per unit line length measurements are the same for both the high flow and the low flow rate cases, as shown in Figure 6.15. The experimental data would be expected to be identical for the same binder delivery level regardless of the flow rate. Nonetheless, there are dramatic differences in feature size for both powder sizes of PCL used for different flow rates. Attempts to demonstrate a similar effect using polymeric solution binders were unsuccessful because the high viscosity of those binders made printing at the high flow rates impossible.

The only unique observation for these experiments was significant ballistic ejection at the high flow rates. Ballistic ejection is the displacement of powder material from the printing region caused by the impact of the binder jet on the powder bed, as illustrated in Figure 6.16. The pressure on the binder had to be doubled to achieve the higher flow rates; the increased pressure causes the binder droplets impact the powder bed with more force and at a higher velocity, as indicated in Appendix A. This phenomenon was not significant at low flow rates. The ejection of powder from the bed results in a change in the bed composition.

Variations in parameters other than binder per unit line length could account for the significantly larger feature size created at the high binder flow

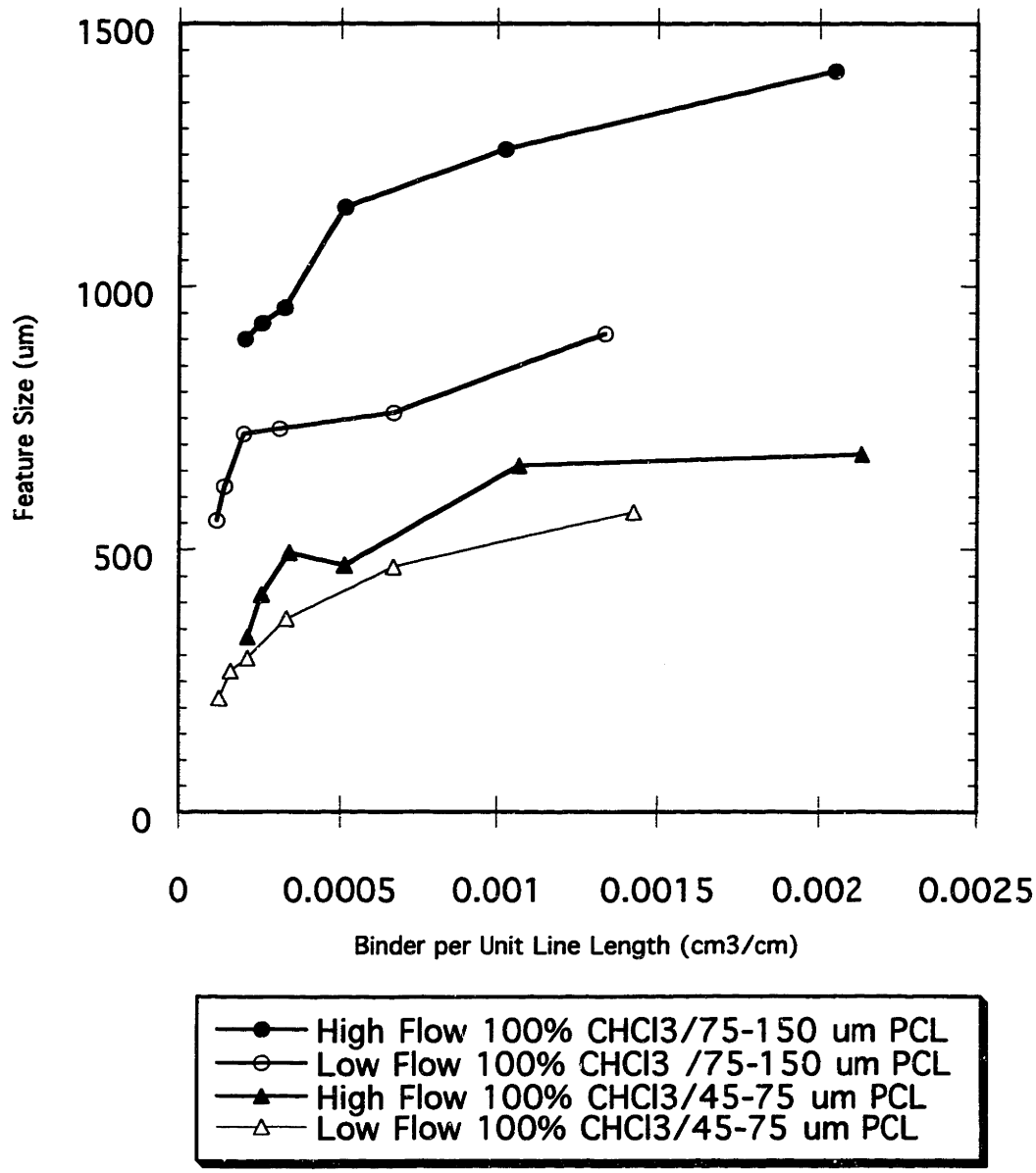

Figure 6.14 Experimental line primitive feature size data for 45-75 um and 75-150 um PCL using 100% chloroform binder at flow rates 1.3-1.5 and 2.3-2.4 g/min

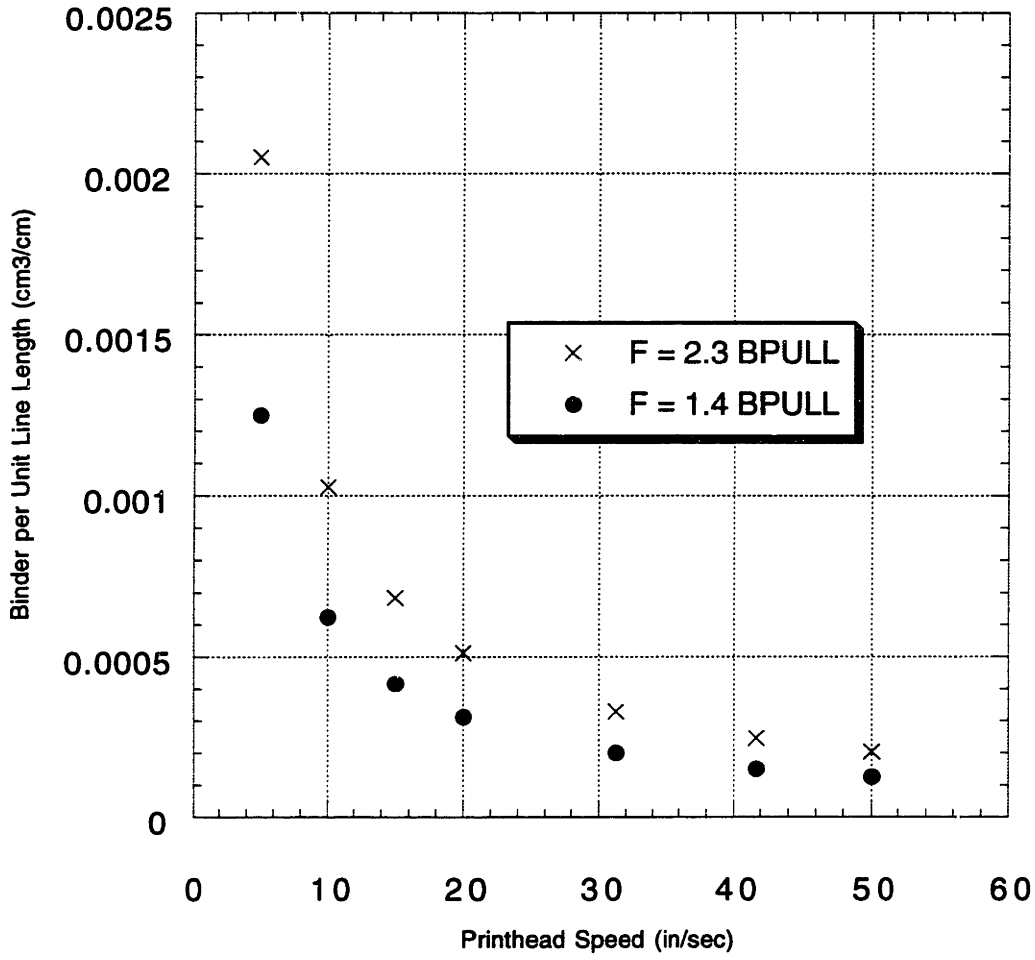

Figure 6.15 Overlap of binder per unit line length measurements for different printhead speed/binder flow rate combinations

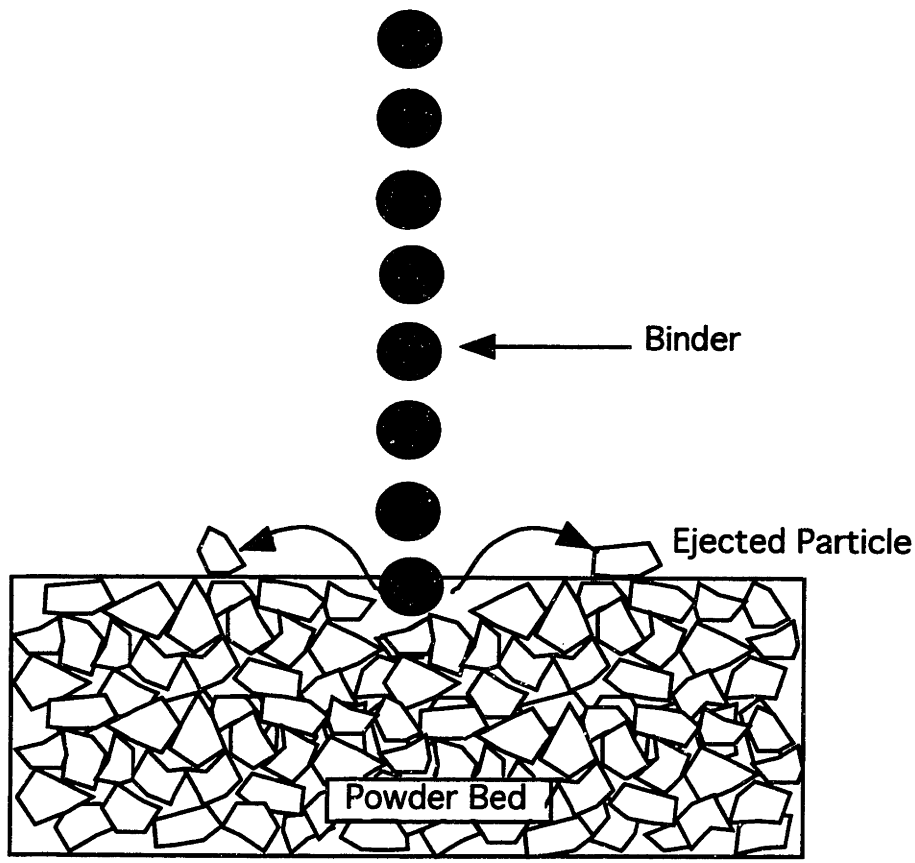

Figure 6.16 Ballistic ejection of powder particles at high binder flow rates

rates. Equation 5.16 can be used to examine the impact on line primitive feature size of variations in the powder bed composition. Changes in the parameters in this equation would occur with significant ballistic ejection. Since powder bed tap density is defined macroscopically, this parameter is largely unaffected by ballistic ejection. The final line density and saturation that could be achieved would be affected by this phenomenon. A void space "valley" is created by the ejection of powder particles. This volume is incorporated in the printed line, as the binder will not completely sink to the new surface before forming the feature. The inclusion of this space in the line may decrease the achievable final line density. Distribution of binder and saturation in the powder bed are also be affected. While the top of feature would still be defined by the powder bed surface and the surrounding particles, the binder might migrate down more easily in the bed in the additional void space. As has been discussed, saturation is the ratio of binder volume to available volume. Removing powder particles from the bed would increase the available volume and necessarily decrease saturation. For 75-150 μm PCL, a 30% drop in the final line density accompanied by a 30% decrease in saturation would increase the theoretical line primitive feature by 40%, as was observed.

The theoretical equations derived in Chapter 5 can be used to elucidate the processes behind predictable and unforeseen experimental data. These equations have been used to show that the line primitive feature size data generated here for novel materials and binder mechanism are similar to the results for ceramic line primitives.

7. DISTORTION OF 3D POLYMER STRUCTURES

Shrinkage that occurs in forming a solid object can result in distortion of polymeric devices fabricated by 3D Printing. Shrinkage occurs as binders evaporate during the printing process and during the drying that takes place after printing is completed. Distortion almost always results in undesired structure in the printed devices. Two types of distortion are possible in these structures: in-plane (within a layer) and out-of-plane (out of one layer into another). Out-of-plane deformation, or warpage, is particularly problematic if it occurs during printing of devices with a large number of layers. A structure protruding out of the powder bed contacts the spreader during powder spreading, prohibiting further printing.

Warpage

Warpage was observed during and after printing in polymer parts constructed using 3D Printing. This type of distortion occurs due non-uniform rates of binder evaporation and it can be severe with highly volatile binders if efforts are not made to control evaporation. When the solvent evaporates, one portion of a printed section shrinks, which changes the shape of the rest of the line. The rate of evaporation is crucial because if it is significantly faster than the rate of solvent diffusion/wicking from surrounding regions, the change in structure of the line can not be accommodated and warpage will be observed, as shown in Figure 7.1.

If the solvent evaporation rate is lower, warpage may also be reduced since the relative difference between evaporation and diffusion is reduced. Several approaches for controlling the binder evaporation rate during and after printing were investigated:

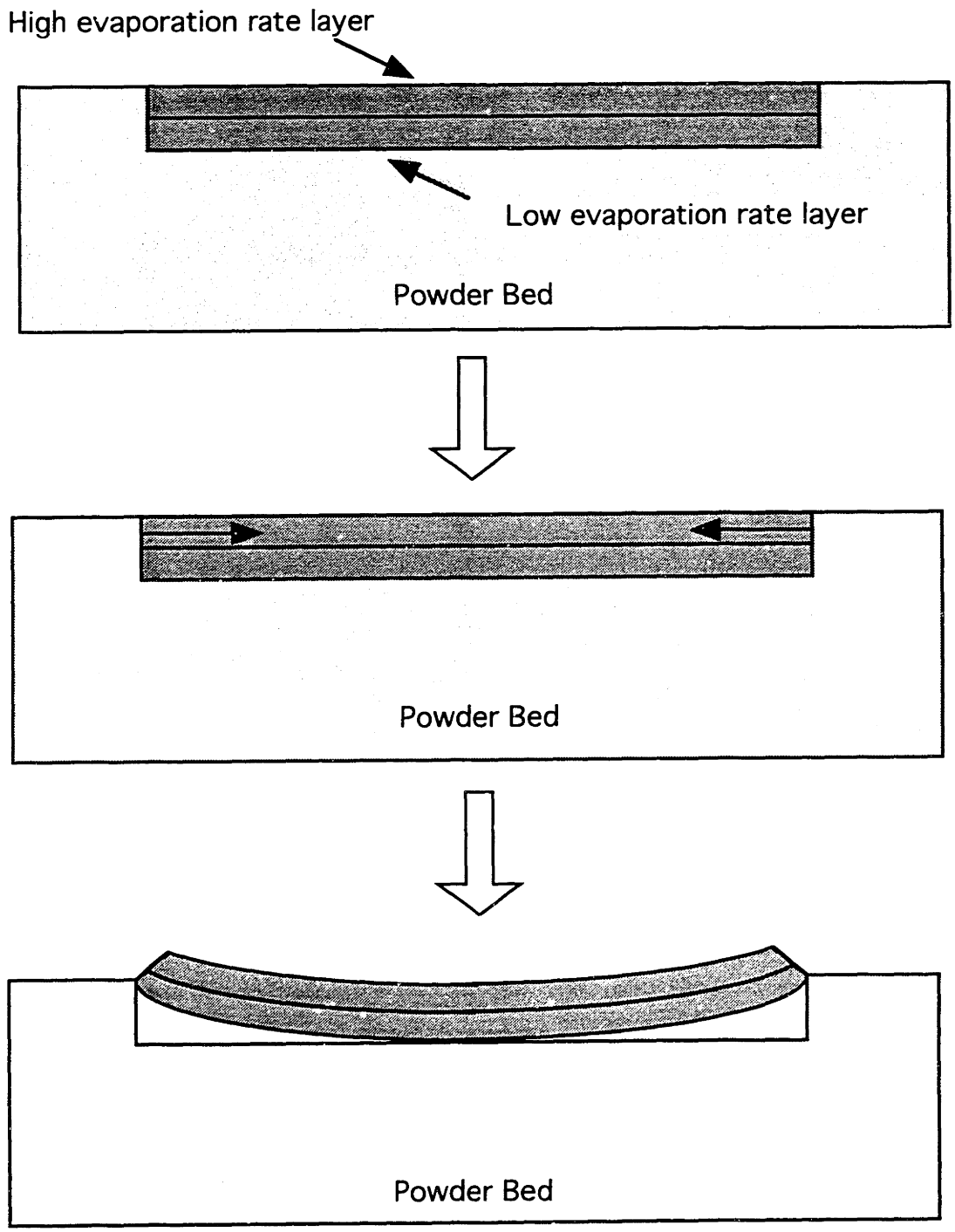

Figure 7.1 Warpage in two layer "device"

- reducing binder volatility
  - low vapor pressure solvents
  - mixed solvents
  - polymeric additives
- promoting adhesion of the first printed layer to a base to prevent warping motion
  - direct piston adhesion
  - "tack down" adhesion
- reducing driving force for evaporation (controlled environment)
- controlling post-processing
  - physical impediment
  - uniform drying

Control of Warpage During Printing

Warpage can be controlled by reducing the volatility of the binder, which will reduce the difference between the binder evaporation rate and the binder diffusion rate. One method for reducing the binder volatility is use a low vapor pressure solvent. As shown in Table 3.2, the low volatility solvents, including dimethyl sulfoxide, cyclohexanone, ethyl acetate, and toluene, do not dissolve PCL to any significant degree. Thus, the binder must include a volatile solvent.

Another method is to use mixed solvents in which one component has a low volatility. Since the amount of the high vapor pressure component is reduced, the overall evaporation rate is reduced. Several mixed solvent binder systems were investigated, including dimethyl sulfoxide, cyclohexanone, ethyl acetate, and toluene in methylene chloride. None of these mixture attempts produced a significant reduction in warpage from the pure solvent case. Because the low

volatility solvents do not dissolve the polymer to a significant extent, they may not "participate in the mechanism of shrinkage.

An alternative to using miscible liquids as the second binder component is to include a soluble solid component such as a polymer. The addition of polymer to the binder increases the binder viscosity, as indicated in Table 3.3. Higher viscosity reduces the binder flow rate and, therefore, the total amount of material delivered per time. Contiguous features can still be created while delivering less binder. Using a 5-15 wt% PCL in methylene chloride polymeric solution binder, devices up 17 layers thick were constructed before warpage precluded further printing.

Changing the solvent component of polymeric solution binders from methylene chloride (vapor pressure = 400 mm Hg) to chloroform (vapor pressure = 199 mm Hg) further reduced the warpage. Devices up to at least 75 layers could be constructed. More layers were not printed due to the depth limitations of the powder bed on the 3D Printing machine used for these applications. While this is an improvement, this approach is somewhat limited for use with these biomedical materials, as these polymers are soluble in only a few, generally high vapor pressures solvents. The method might be tremendously useful with other polymeric materials that might be soluble in a wider range of solvents.

A second approach for controlling warpage is to promote adhesion of the bottom of a printed device directly to a base. Stresses which develop at the top of the device are then resisted by the forces of adhesion at the base. One implementation of this approach involves using double-sided tape on the piston plate to hold spread powder and the printed device in place. This was initially effective, but the solvent would ultimately dissolve the adhesive and the device immediately warped. Adhering the first layer to the piston by printing over a single layer of powder on the piston plate successfully prevented warpage in numerous devices and for long print times. The first layers of such devices were

somewhat irregular. This irregularity was due to the fact that the polymeric powders did not stick to the smooth metal piston plate, which made it impossible to spread even layers. Another option was to restrict the powder material to the center portion of the piston only, printing the binder on the powder material in the center and directly on the piston around the edges to affix the printed objects to the piston, tacking the device down.

These "tack down" approaches made it possible to construct devices with multiple layers of varying complexity, but its application is limited. Scale-up to printing large numbers of devices at a time would be difficult due to powder bed space limitations. While a single "tack down region" around the border might be possible, a larger powder bed would be necessary for such an experiment. Another limitation in this approach is that it could cause distortion on the edges or be completely unsuccessful with very thick devices, when the height difference between the printing layer and the tack down region would be greater than the maximum difference investigated with these experiments (about 30 150 μm layers).

Another method for controlling the evaporation rate of the binder, and therefore warpage, is to reduce the driving force for evaporation out of the powder bed. If no solvent is present in the vapor state over the bed, the driving force for evaporation is high. Conversely, if the atmosphere over the bed were completely saturated with solvent, the driving force for evaporation would be zero. Thus, if the atmosphere over the bed were controlled, the evaporation rate of the solvent could also be adjusted, conceivably to the point of eliminating warpage due to evaporation gradients or high evaporation rates in a device.

Implementation of this approach requires encasing the entire machine in a controlled atmosphere, as the printing region could not be easily isolated. This is not easily done given the current machien set-up. The machine was enclosed in a polyethylene glove bag, which was affixed around the base of the machine using

duct tape. Chloroform was allowed to evaporate for 2-14 hours in the closed glove bag to saturate the atmosphere over the powder bed. Printing was then begun using a 100% chloroform binder. Increased adhesion of the polymer powders to the roller spreader was observed, but spreading of a powder layer was still possible. These layers were less uniform than typical powder beds and tap density likely was reduced. Warpage was observed in printing onto a loose bed of powder. Printing directly onto the piston using a solvent binder in this atmosphere allowed for the construction of a device at least 15 layers thick. Use of solvent binders in an open atmosphere permitted construction of only 2-3 layer devices.

Other issues make it difficult to judge the success of controlling the solvent atmosphere to eradicate warpage. As mentioned, the atmosphere produced a detrimental effect on powder bed character and powder tap density. An ideal arrangement would be to control the atmosphere over the powder bed while limiting the exposure of the bed to the solvent in order to avoid altering the character of the latter, but that would require a completely different machine set-up. This implementation of atmosphere control is crude at best. The saturation of the atmosphere was not measured, so it is possible that complete saturation was not achieved. As a result, it is somewhat premature to draw conclusions about the potential for controlling warpage using this approach.

Control of Warpage After Printing

Warpage of a significant magnitude also occurred after printing was complete. Virtually all devices more than a layer or two in thickness held a significant amount of solvent after printing was complete. In the original processing protocol, the powder bed was left to completely dry after the final layer was printed, leaving the top layer exposed. Drying of the devices in the

powder bed for up to 12 hours in a hood was sufficient to allow for removal of the structures from the bed (Work by Giordano, et al indicates that more time or use of a vacuum is necessary to completely remove residual solvent)[16]. With no impediment to evaporation over the top layer, mass transfer from that layer is very high, whereas mass transfer is low in the first (still buried) layer due to the surrounding powder. This results in different amounts of shrinkage through the device, and the device edges warp up out of the top of the powder bed. If these mass transfer rates were reversed (the top layer covered with powder and the bottom layer exposed) while maintaining the same bottom-top orientation, the device warped down (device edges bending down) to reduce the resulting stresses through the device.

One approach to preventing this warpage is a physical impediment. A 45 gram piston plate placed over the top layer (resting on the piston edges) limited out-of-plane warpage to less than a layer thickness. This approach was particularly successful when used in conjunction with the "tack down" approach to warpage control described above. However, the applicability of this approach is limited in that placing a weight over a large powder bed with a large number of devices is impractical, particularly if long drying times continue to be required.

A second approach to preventing this type of warpage is to alleviate the accumulation of stresses in the printed device. This would require that the evaporation rate throughout a device be uniform. A controlled atmosphere environment with a uniform (perhaps even completely saturated) solvent partial pressure would be useful to this end. An alternative approximation would be to equilibrate the mass transfer on all sides of the devices and to slow the evaporation process down as much as possible to avoid creating large gradients in mass transfer from the outside edges to the interior. To this end, loose powder, (equivalent to about 30 layers) was placed on top of the device once printing was completed. Warpage was minimal in devices encased in such a powder bed

throughout the drying process. In addition, this approach for controlling warpage after printing would be amenable to scale-up, since only more loose powder would be required for implementation.

In-Plane Distortion

In-plane distortion has also been observed in a wide variety of polymeric 3D Printing implementations. In all of these instances, the magnitude of the distortion was dramatically less than any out-of-plane warpage. The primary examples of in-plane distortion consisted of slightly sloping vertical walls or "drooping" structures. The distortion in the former was generally uniform in a particular direction within a given device and may be attributable to the activity of powder spreading. The latter was seen exclusively in unsupported structures. This phenomena may be eradicated by adjusting printing parameters to avoid oversaturation when printing unsupported features. Given the relatively small magnitude of in-plane warpage, exhaustive investigations to control these distortions were not undertaken.

8. EXPERIMENTAL MATRIX DEVICES

The next task in developing 3D Printing for polymeric materials applications involved fabrication of designed three dimensional objects. Intimate control of the shape and structure of 3D devices is also vital to the development of tissue regeneration devices. Construction of 3D objects involves the joining of single lines vertically and horizontally. Thus, adhesion between a line and those above, below, and on either side, is crucial for building a contiguous device. The initial three dimensional test pieces were designed to explore these issues.

In designing preliminary matrix device analogs, several fabrication limitations inherent in the selection of organic solvents as the primary binder component and the use of the Pre-Proto 3D Printing machine had to be considered. The set-up used with these experiments involves a continuous jet printhead with no on/off control. This printing mode limits the types of structures that can be fabricated; straight lines of travel across the powder bed are necessary in order to avoid the build-up of binder during changes of direction in printing. Building structures in this way is analogous to drawing a picture without taking the pencil off the drawing page. The continuous jet on/off limitations also result in the necessity for overlapping printed lines. The regions surrounding the overlap are subject to binder flooding, since twice as much binder is delivered there. As discussed in Chapter 6, uniform jets were not generated with the current Pre-Proto set-up. The printheads lacked the necessary piezoelectric devices and the machine was not equipped with the necessary electronics to print in this mode. In addition, some devices require void spaces to be included in the structure. While these spaces can be obtained by simply not printing in particular locations, excess binder from overlapping lines or high binder per unit line length regions must not bond the loose powder in those regions. As a result, creating even simple structures with a raster machine without on/off control is quite involved. While relatively simple devices can be constructed using this modified set-up, fabrication of more complex devices will require further printhead development.

Control of Macroscopic Shape

A schematic of a designed device with controlled macroscopic structure is shown in Figure 8.1. This device was fabricated by printing six straight lines separated by loose powder. The powder bed was rotated 90° and the process was repeated on the same layer to produce square channels running in the vertical direction through the device. After printing 10 layers, the first two lines/walls were deleted from the program and the fabrication process was continued. After 10 more layers, the second pair of lines/walls was deleted and the build continued with only two lines/walls in each direction for each layer. Warpage was controlled by using a chloroform-based binder and the "tack-down" approach using double-sided tape on the piston plate. This device was constructed using PLA with a particle size of 75-150 μm as the powder bed material and 100% chloroform as the binder. The layer thickness was 150 μm. The binder per unit line length level was 1.34×10^{-3} cm^3/cm.

The square channels of this printed device visible in Figure 8.2a are designed to be 4 mm across. Some of these channels are slightly rounded and smaller than the designed size. This rounding phenomenon is observed only in the corners of the channels and not along the length of the defining walls, so it is due to the proximity of overlapping lines in those locations. The size of the channels is slightly smaller than designed due to the wall thickness being slightly larger than the thickness of an individual line. This anticipated feature size increase is due to the vertical stacking of individual lines. Characterization of the feature size for stacked lines (walls) would be a useful future investigation.

Figure 8.2b shows additional control over the 3D structure. The walls defining the square vertical channels vary in height. Structures similar to this "stair-stepping" might be explored as a means of effecting tailored cell migration, but in this experiment it demonstrates control over the structure through the third dimension of the device. The shorter walls (10 layers and 20 layers) were only printed through a portion of the build process, while the tallest walls (30 layers) were constructed through the entire build.. This is a crude demonstration of the

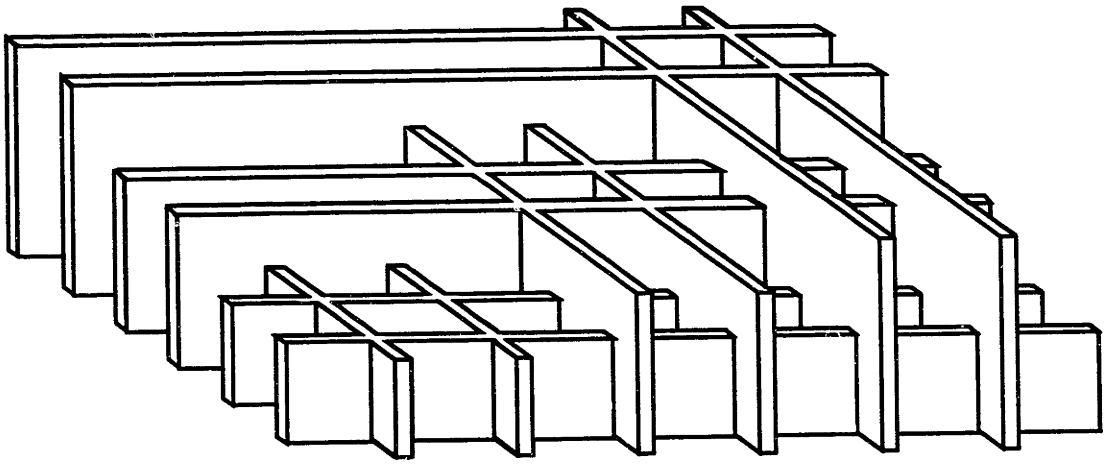

Figure 8.1 Design of a controlled macroscopic shape device

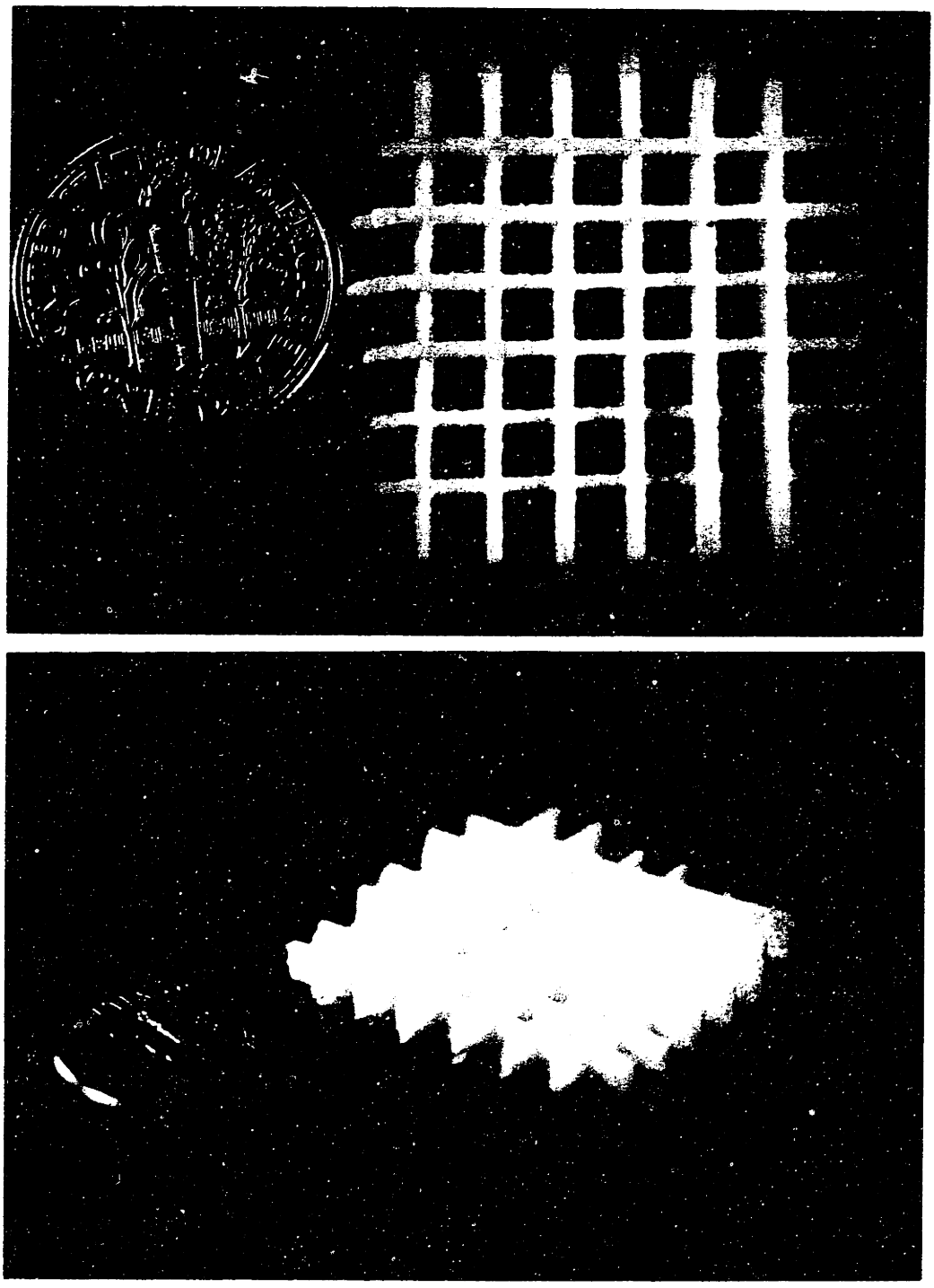

Figure 8.2 PLA experimental matrix device demonstrating control over macroscopic shape Binder: 100% chloroform; Binder per unit line length: 1.34×10^{-3} cm^3/cm; Powder: PLA 75-150 μm (a) top view of device showing channel dimensions (b) side view showing layered structure

potential for fabricating structures that might be possible with more sophisticated on/off printhead controls. The minor in-plane distortion in the vertical walls is due to warpage that occurred during the build process.

Oriented Channels in 3D Devices

An additional level of structural control to be demonstrated was the incorporation of specifically oriented channels within a device. Fabrication of devices with oriented channels on the scale of 0.1-1 mm requires a modification in the path the printhead follows in creating a device. In addition, due to the increased void fraction in such devices, line to line and layer to layer adhesion is more critical. An oriented channel device was fabricated by executing only 1/2 of the process described above; that is, six single lines were printed, but the powder bed rotated every five layers. The build process and device appearance are shown in Figure 8.3. This created a stack of layers with channels alternating in orientation. The location of channels within the device is unique depending on the face considered. The rotating process also produced channels running through the vertical dimension similar to those built into the previous device. This device was constructed using a 26.5 wt% acid modified PCL in chloroform binder and a powder bed consisting of a 70-30 mixture of PCL (75-150 μm) and bovine bone (<250 μm). The layer thickness in constructing this device was 100 μm. The binder per unit line length level was 3.33×10^{-4} cm^3/cm.

Figure 8.4 shows the various faces of this device. The structure of the device was very difficult to capture on film due to its small scale. While oriented porosity was demonstrated in this device, it was very fragile. The lack of structural integrity was due to decreased adhesion between layers. A decrease in the area for adhesion is one reason for the reduced layer-to-layer cohesion. Only the region where walls overlapped was area available for bonding between the top-most layer of the channels oriented in one direction and the bottom layer of the channels oriented in the perpendicular direction. In addition, the overall decrease

Build Approach:

5 layers of (a), then 5 layers of (b), repeat.

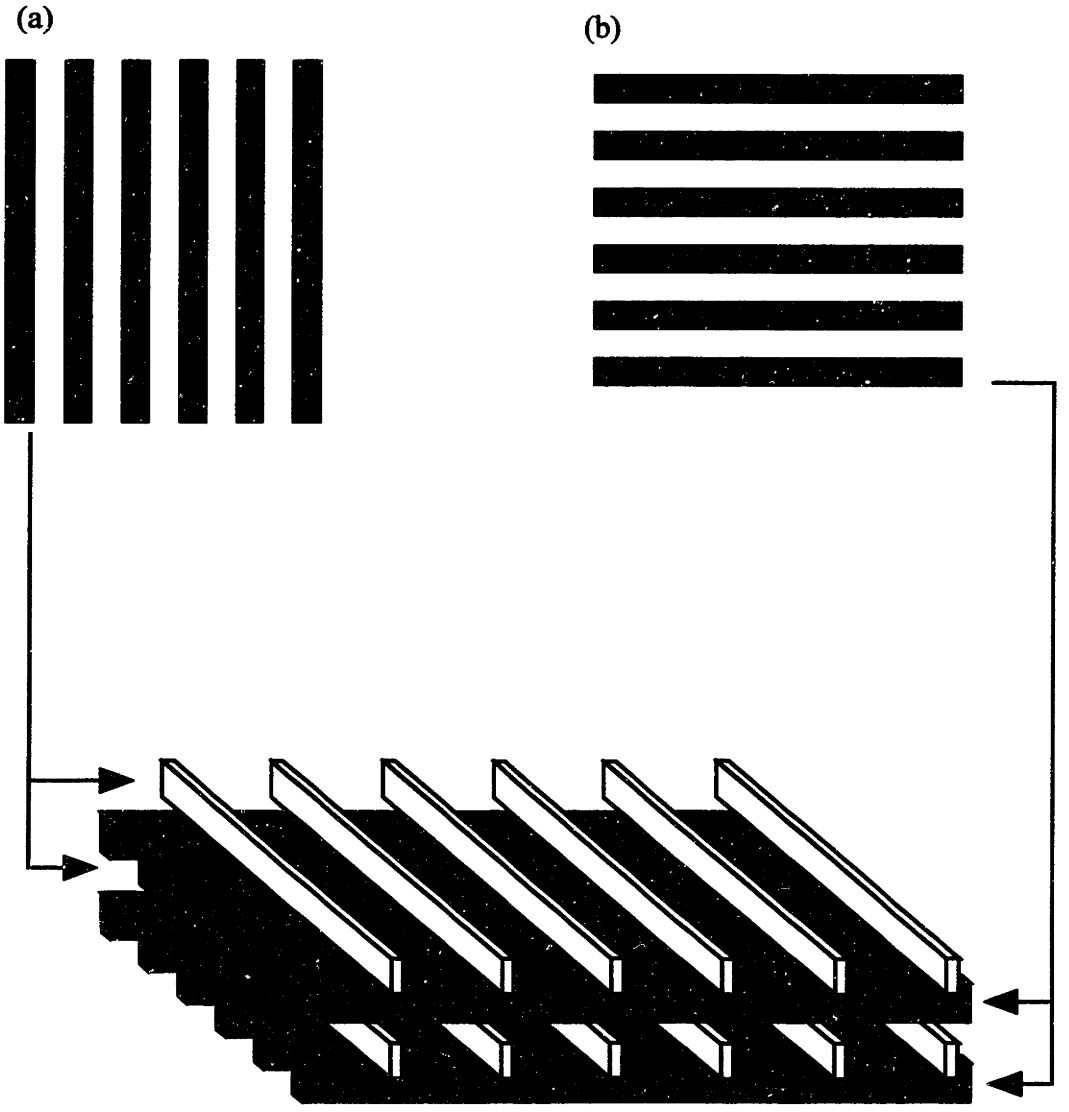

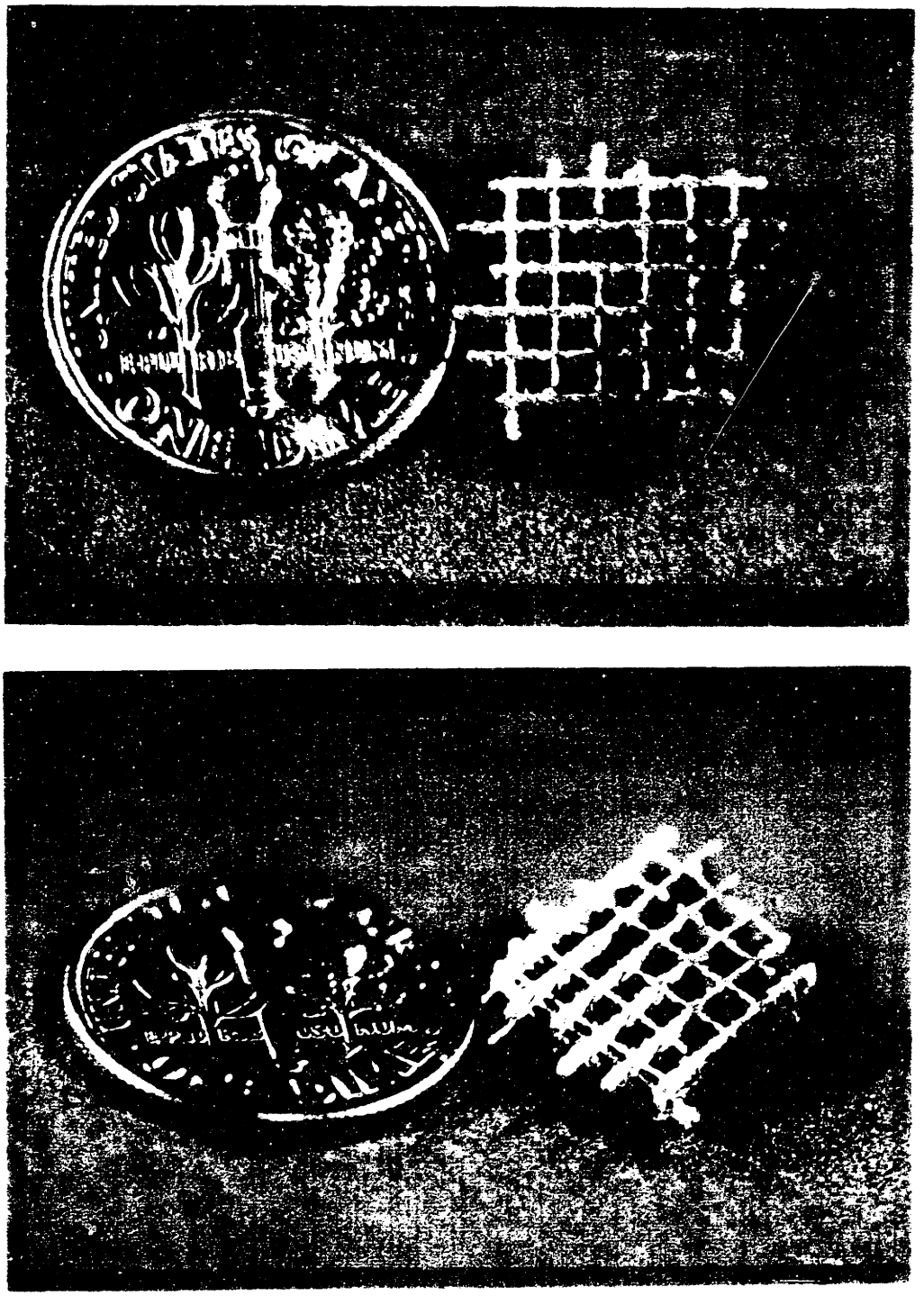

Figure 8.4 PCL-Bovine bone experimental matrix device demonstrating oriented porosity and incorporation of non-soluble entity in the device. Binder: 10 wt% PCL in chloroform; Binder per unit line length: 3.33 x 10^{-4} cm^3/cm; Powder: 70-30 mixture of PCL (75-150 μm) and bovine bone (< 250 μm);

in the amount of polymer available for particle bonding due to the incorporation of bone material in the powder bed also contributed to the frail nature of the device.

Another reason for the poor structural integrity of this device may be the small layer thickness used in fabricating the object. The thin layer thickness was employed to ensure layer to layer adhesion. However, that approach might have produced the opposite effect. The 100 μm layer thickness is smaller than some of the polymer and bone particles. As a result, in some locations, the particles would have been pushed along the surface of the powder bed rather than filling in the spaces. This produces a non-uniform powder bed with a low tap density. The non-uniformity could negatively affect layer to layer bonding.

Despite these structural problems, this part successfully demonstrates the inclusion of a non-polymeric component in the powder bed and in the final part. The bone material was included in the device in order to demonstrate the incorporation of non-soluble material within a polymeric device. Such material might be important for some bone regeneration applications.

Microporosity in 3D Devices

A third level of structure desirable to incorporate in three dimensional structures is microporosity on the scale of 50-250 μm. Based on the single line primitive results discussed in the previous section, features less than 200 μm can not be printed via the 3D Printing process at the present time. Microporosity can be generated by including a leachable component in the solid structure.

Devices were constructed using a process similar to those described above. The powder bed material was 100% NaCl (particle size 75-150 μm) and the binder was a 30 wt% solution of acid-modified PCL in chloroform. The layer thickness was 150 μm. The binder per unit line length level was 2.85×10^{-4} cm^3/cm. After drying, these devices were placed in water for 18 hours to leach out the salt particles.

A section of the resulting device is shown in Figure 8.5. The pores in this device are on the order of 50-250 μm. This example has a similar macroscopic structure as in the device shown in Figures 8.2a and 8.2b. This device weighed 450 mg prior to leaching. After leaching, the structure weighed only 68 mg. Based on the printing parameters described above and the character of the powder bed, if the salt were completely removed from the device, it would have weighed 65 mg. Thus, 99% of the NaCl powder bed material has been leached out of the final device. Thus, the part is a landmark on two fronts: it demonstrates the fabrication of microstructure in a device and it is the first 3D printed device of any kind to be constructed only of material that was delivered through the printhead.

Variable Density Devices

Devices with appreciable strengths might be useful in tissue regeneration applications in which some initial strength would be crucial. The mechanical properties of these devices might be improved by an appropriate design. Despite current machine limitations, such a device with a porous core surrounded by a dense border could be constructed by printing several solid layers and then solid regions on the edges and a channel-generating mesh in the middle on succeeding layers. Finally, printing several solid layers on the top produces a solid border surrounding the inner channeled core. The designed appearance of this device is shown in Figure 8.6. In addition, this fabrication approach also demonstrates that device construction could be effected in several orientations. This device was built horizontally with channels running parallel to the piston surface. The powder bed material in both cases was 75-150 μm PCL with a binder of 26.5 wt% acid modified PCL in chloroform. The layer thickness in each device was 250 μm. The binder per unit line length level was different in the different regions of the structure. For the dense border, the binder per unit line length level was 1.33×10^{-3} cm^3/cm. For the channel walls in the inner porous region, the binder per unit line length level was 3.33×10^{-4} cm^3/cm.

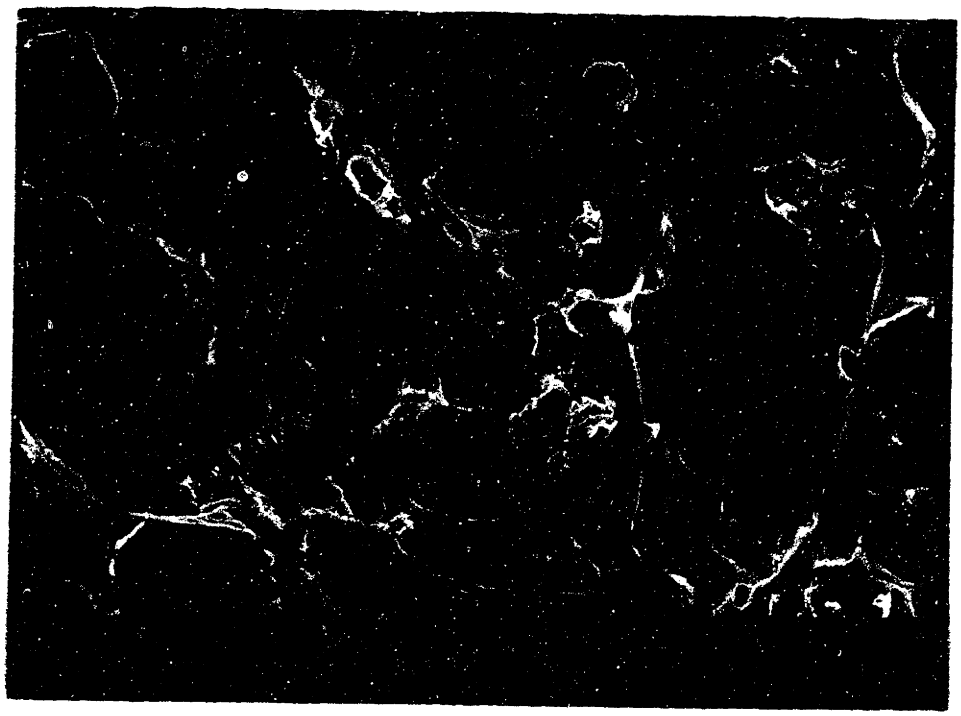

Figure 8.5 Cross section of leached acid-modified PCL experimental matrix device demonstrating structural microporosity. Binder: 26.5 wt% acid-modified PCL in chloroform; Binder per unit line length: 2.85 x 10^{-4} cm^3/cm; Powder: NaCl (leached out) 75-150 μm;

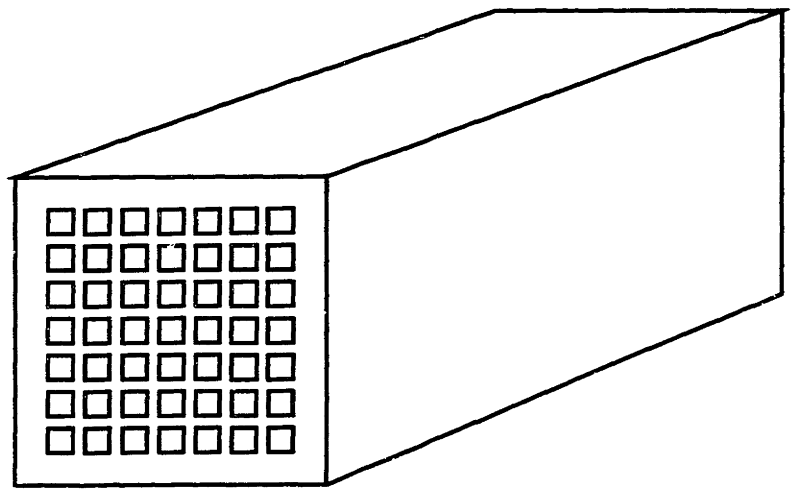

Figure 8.6 Design of variable density device (within a single structure)

A cross section of such a device is shown in Figure 8.7. This figure demonstrates some of the problems in fabricating a device with variable density. Incorporation of regions with drastically different densities in a single device is difficult because the amount of binder delivered to each region is dramatically different. Specific placement of the binder is particularly important given the close proximity of the dense and porous regions. Solid regions require a very high amount of binder to make the region solid, but this high rate of delivery could result in bleeding to the porous region. As shown in Figure 8.7, all of the interior channels are open, but some of the channels around the edge (close to the dense region) are closed or partially obstructed. This is likely due to migration of some binder from the dense region into those channels.

Discussion

These three dimensional devices are very simple in configuration, but they demonstrate the ease with which designed structures can be fabricated via 3D Printing. Despite several inherent (though temporary) limitations, devices with some complexity could be built. These devices demonstrate the structural control necessary for fabricating viable tissue regeneration matrices. Fruitful tissue regeneration endeavors may be explored using reticulated matrices fabricated by 3D Printing.

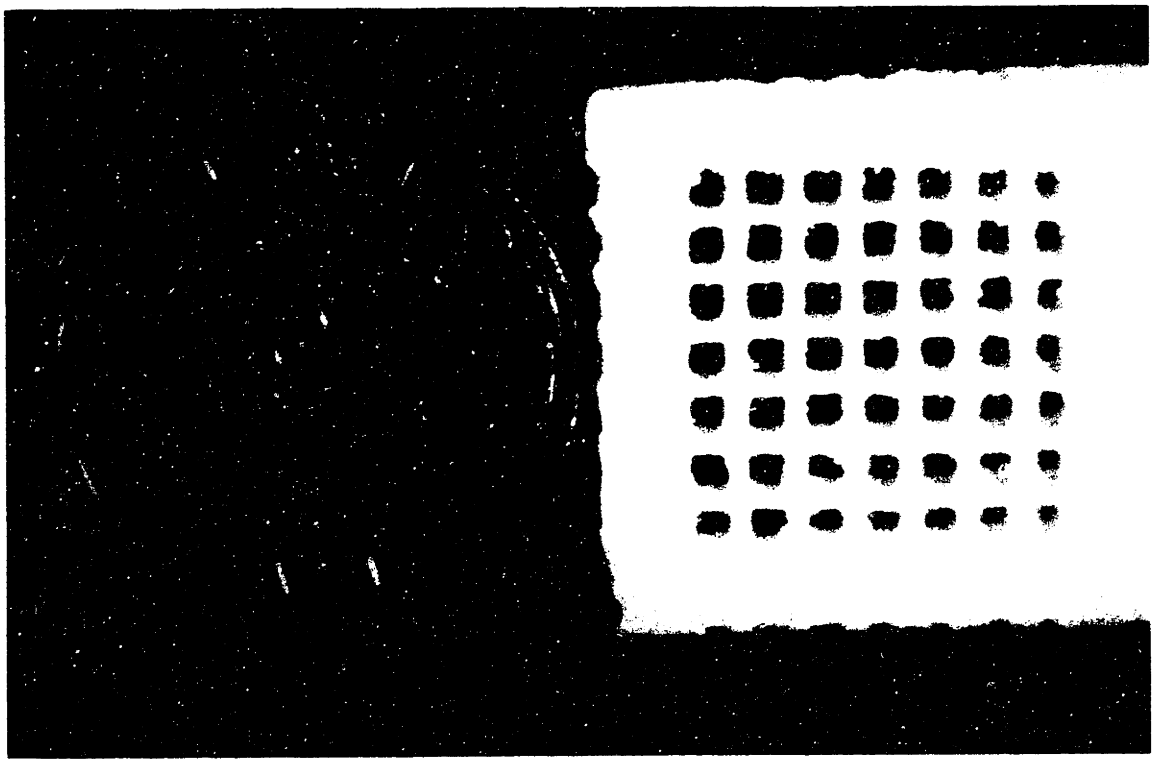

Figure 8.7 Cross section of PCL experimental device incorporating variable density within a single 3D object. Binder: 26.5 wt% acid-modified PCL in chloroform; Binder per unit line length: 3.33×10^{-4} cm^3/cm; Powder: PCL 75-150 μm;

9. CONCLUSION

This work demonstrates the viability of fabricating complex reticulated structures from biomedical polymeric materials by 3D Printing. A novel particle-to-particle bonding mechanism was successfully demonstrated and investigated. Line primitives as small as 200 μm were produced from PLA and PCL with this technique. Smaller feature sizes are foreseeable, given the proper printing conditions and initial powder sizes.

A theoretical line primitive feature size model was developed. This equation was used to determine which parameters control feature formation. Some of the dominant processes are unique for these materials and this type of binder-powder interaction. As in other 3D Printing applications, the amount of binder delivered to the powder bed directly impacts the size of features created. Powder bed saturation and polymer dissolution, in particular, directly impact the size and character of features created, as well. Problems with structural distortion encountered as a result of the current machine design limitations were overcome. These successes are encouraging for future development.

Prototype three dimensional devices were demonstrated. The structural features incorporated in the fabricated devices would be ideally suited for matrices for tissue regeneration. Such devices require a very specific reticulated structures for successful tissue replacement. Incorporation of a complex macroscopic shape, oriented channels, and microporosity within a single three dimensional device is virtually unobtainable by any other fabrication process. This work, while showing these features separately, demonstrates that this process is amenable to such complex fabrication.

This work represents a significant building block for improvements in the fabrication of tissue regeneration devices, as well as other fields that use complex

structured polymeric materials. Much untapped potential exists for constructing complex polymeric structures using the 3D Printing process.

Appendix A: Binder Droplet Diameter

As first described by Savart, a laminar-flow jet will break up into discrete droplets[17]. The surface energy of a liquid sphere is less than that for a cylinder of the same volume, so a cylindrical column of fluid is inherently unstable and will revert to the more stable droplet configuration. The individual droplets will be formed by disturbances that are created and propagate in the cylindrical jet. Rayleigh related the growth of those disturbances to the disturbance wavelength[18]. The disturbance with the largest growth factor will develop the most quickly and dominate the jet behavior. A single disturbance wavelength yields that growth factor. This wavelength is given by the Rayleigh equation

$$\lambda_m = 4.51 D_o \tag{A-1}$$

where λ_m = wavelength for maximum growth factor (cm)

D_o = orifice diameter (cm).

Several others have investigated the phenomenon of droplet formation since Rayleigh's work[19,20,21] and arrived at slightly different values for the constant in equation A-1. Nonetheless, the Rayleigh equation adequately describes the droplet formation wavelength for this examination.

The binder jet velocity is

$$v = \frac{F}{60(\rho_b)(A)} \tag{A-2}$$

where F = binder mass flow rate (g/min)

ρ_b = binder density (g/cm^3)

A = orifice area = $(\pi/4)D_o^2$.

A single droplet is formed whenever a disturbance wave reaches the point of droplet formation. The spontaneous (or natural) frequency of droplet formation is given by[22]

$$f_s = \frac{v}{\lambda_m} = \frac{v}{4.51\ D_o} \tag{A-3}$$

where f_s = droplet frequency (1/s)

v = binder jet velocity (cm/s).

Substituting the binder velocity given in equation A-2 into A-3 yields

$$f_s = \frac{F}{67.65\pi\ \rho_b (D_o)^3} \tag{A-4}$$

The volume of each droplet is determined from the ratio of the volumetric flow rate (mass flow rate divided by density) to the droplet frequency, as given in equation A-5:

$$V_{drop} = \frac{F}{\rho_b\ f_s} = 1.13\pi\ (D_o)^3 \tag{A-5}$$

where V_{drop} = drop volume (cm^3).

If each binder drop is assumed to be spherical, the drop volume is also given by

$$V_{drop} = \frac{4\pi}{3} R_d^3 = \frac{\pi}{6} D_d^3 \qquad \text{(A-6)}$$

where R_d = drop radius (cm)

D_d = drop diameter (cm).

After equating A-5 and A-6 and simplifying, the drop diameter is given by

$$D_d = 1.89\,(D_o) \qquad \text{(A-7)}$$

All of this work was done using a printhead with an orifice diameter of 45.7 μm. Considering only the 100% chloroform binders, the binder density is 1.473 g/cm^3. Two flow rates were examined: 1.4 and 2.3 g/min. The results for these conditions using the above equations are given below:

flow rate F	1.4 g/min	2.3 g/min
disturbance wavelength λ_m	206.1 μm	206.1 μm
binder velocity v	965.7 cm/s	1586.5 cm/s
drop frequency f_s	46,850 drops/s	76,970 drops/s
drop diameter D_d	86.4 μm	86.4 μm.

This type of analysis for polymeric solution binders is much more involved. The Rayleigh equation does not account for polymeric materials in a jet. The presence of very low concentrations (0.002-0.01 wt %) of a polymeric component in the jet solution decreases jet stability and significantly increases the separation length (jet length required to form drops)[23]. The introduction of the polymer component also serves to increase jet viscosity, as indicated in Table 3.4. High viscosity impacts drop formation from a jet. As Sweet observed, jet breakup is considerably different for high viscosity materials in that regular spacing of the drops may not occur[24]. Also, the disturbance growth factor introduced by Rayleigh to describe disturbance propagation in a jet begins to vary with viscosity at jet viscosities higher than 10 cP[19]. Thus, given the composition and viscosity of the polymeric solution binders, the disturbance wavelength, drop frequency, and drop diameter are much more difficult to determine.

Appendix B: Wet Bulb Temperature

The wet bulb temperature is the steady state evaporation temperature. The temperature of a drop decreases as the material evaporates. In turn, evaporation decreases. The drop is also heated by the surroundings, which increases the drop temperature and evaporation. Some steady state will be reached where the heating from the environment will balance the cooling due to evaporation. The wet bulb temperature is given by

$$T_{wb} = T_{\infty} - \frac{\Delta H_v \; M_s}{C_p \; Le^{2/3} \; M_{air}} \quad (X_A - X_{A\infty}) \qquad \text{(B-1)}$$

where T_{wb} = wet bulb temperature (°C)

T_{OO} = temperature at distance infinity (°C)

ΔH = enthalpy of vaporization (J/mol)

M_s= molecular weight of solvent (g/mol)

M_{air} = molecular weight of air (g/mol)

C_p= heat capacity (J/mol °C)

Le = Lewis # = α/D_{AB}
(ratio of thermal to mass diffusivity)

X_A = mole fraction of solvent on drop surface

X_{AOO} = mole fraction of solvent at distance infinity.

X_A is given by the relationship

$$X_A = \frac{P_{sat}}{P} \qquad \text{(B-2)}$$

where P_{sat} = partial pressure at saturation (mm Hg)

P = ambient pressure (mm Hg).

P_{sat} /temperature relations can be obtained from the well-known Antoine equation, which is of the form

$$\log_{10} P_{sat} = A - \frac{B}{T(^{o}C) + C} \qquad \text{(B-3)}$$

where A, B, C are material-specific constants.

Equations B-1 and B-3 must be solved simultaneously to determine the wet bulb temperature. For chloroform the above parameters have the following values:

ΔH = 29, 200 J/mol

M_s= 119.38 g/mol

C_p= 109.96 J/mol °C

A = 6.90328

B = 1163.03

C = 227.4.

For simplicity, the following approximations are made:

$X_{AOO} \sim 0$

Le = 1

M_{air} = 29 g/mol

T_{OO} = 25 °C.

As a result, the two equations to be solved simultaneously for this particular case are given by

$$T_{wb} = 25 - 1093.15(X_A) \quad [^{\circ}C] \tag{B-4}$$

$$\log_{10} P_{sat} = 6.90328 - \frac{1163.03}{T_{wb}(^{\circ}C) + 227.4} \tag{B-5}$$

The solution of B-4 and B-5 is

$T_{wb} = -14.5\ ^{\circ}C.$

Appendix C: Evaporation of Binder Drops During Flight

The change of the mass of a binder drop with time quantifies the amount of the binder that evaporates over time. The change in mass per time is easily converted to the change in the drop diameter with time

$$\frac{dm}{dt} = \rho_b \frac{dV}{dt} = \rho_b \frac{4}{3} \pi \frac{dR^3}{dt} = \rho_b \frac{\pi}{6} \frac{d D^3}{dt} = \rho_b \frac{\pi}{2} D^2 \frac{d D}{dt} \qquad \text{(C-1)}$$

where m = binder drop mass (g)

ρ_b = binder density (g/cm^3)

V = binder drop volume (cm^3)

R = binder drop radius (cm)

D = binder drop diameter (cm)

t = time (sec).

The evaporation of binder drops as they are delivered to the powder bed can be quanitified by doing a mass balance on the binder material in the drop. The mass balance on the chlorofrom drop is given by

$$\rho_b \frac{\pi}{2} D^2 \frac{d D}{dt} = - N_A M_s A \qquad \text{(C-2)}$$

where N_A = molar flux of solvent (mol/cm^2 sec)

M_s = binder solvent molecular weight (g/mol)

A = binder drop surface area (cm^2) = $4\pi(D/2)^2$.

The molar flux of solvent from a drop is defined as

$$N_A = k_m \overline{C} X_A \tag{C-3}$$

where k_m = mass transfer coefficient (cm/sec)

C = average concentration (mol/cm^3)

X_A = mole fraction of solvent on drop surface.

The mass transfer coefficient is also given as

$$k_m = \frac{Sh\ D_{AB}}{D} \tag{C-4}$$

where Sh = Sherwood number
(ratio of mass diffusivity to molecular diffusivity)

D_{AB} = diffusion coefficient (cm^2/sec).

Thus, the equation to be solved to determine the change in the diameter of a binder drop due to evaporation during delivery to the powder bed is given by

$$\frac{dD}{dt} = - \frac{Sh\ D_{AB}}{D} \overline{C} X_A\ M_s\ \frac{2}{\rho} \tag{C-5}$$

At time t = 0, the diameter is the initial drop diameter. As such, the initial condition associated with this equation is

$$D = D_i \quad @ \quad t=0 \tag{C-6}$$

The solution of Equation C-5 using this initial condition is

$$D = \left[D_i^2 - \frac{4\,Sh\,D_{AB}}{\rho} \overline{C}\, X_A\, M_s\, t \right]^{1/2} \quad . \tag{C-7}$$

For 100% chloroform drops printed in air at 25 °C,

$D_i = 86.4\ \mu m$ (as determined in Appendix A)

$\rho_b = 1.473\ g/cm^3$

$M_s = 119.38$ g/mol.

The variables D_{AB}, Sh, C, X_A and t must be determined to evaluate Equation C-7.

The diffusion coefficient D_{AB} of chloroform in air can be determined the Chapman-Enskog theory. This approach is the most common method for estimating gaseous diffusion and it is accurate to an average of about 8%. This theory yields the general diffusion coefficient equation

$$D_{AB} = \frac{(1.86 \times 10^{-3})\, T^{3/2} (1/M_1 + 1/M_2)^{1/2}}{P\, \sigma_{12}\, \Omega} \tag{C-8}$$

where M_1 = solute molecular weight (g/mol)

M_2 = surrounding gas molecular weight (g/mol)

T = temperature (°K)

P = pressure (atm)

σ_{12}, Ω = material-specific parameters.

For chloroform in air at 1 atm and 25 °C,

$P = 1$ atm

$T = 298$ K

$M_1 = 119.38$ g/mol

$M_2 = 29$ g/mol

$\sigma_{12} = 4.550$

$\Omega = 1.111$

Using these values for the parameters in Equation C-8, the diffusion coefficient for chloroform in air can be easily evaluated as

$D_{AB} = 0.08613$ cm^2/sec (at 25 °C and 1 atm).

The Sherwood number is often described by the relation

$$Sh = 2 + 0.6\, Re^{1/2} Sc^{1/3} \qquad \text{(C-9)}$$

where Re = Reynolds number = vD/ν
(ratio of inertial and viscous forces)

v = velocity (cm/sec)
ν = kinematic viscosity (cm^2/sec)

Sc = Schmidt number = ν/D_{AB}
(ratio of momentum and mass diffusivities)

For this experimental scenario with 86.4 μm chloroform drops travelling at a velocity (as determined in Appendix A) of 965.7 cm/sec,

Re = 2268

Sc = 0.04272
($\nu = 3.68$ cm^2/sec for chloroform at 25 °C).

As a result, the second term in Equation C-9 is

$$0.6\,Re^{1/2}\,Sc^{1/3} \sim 10.$$

The Sherwood number can then be approximated as 12 in order to simplify the diameter dependence in Equation C-7.

The average concentration (C) can be determined from the ideal gas law at 1 atm, 25 °C:

$$C = P/RT = 4.09 \times 10^{-5}\ mol/cm^3 \qquad (C\text{-}10)$$

where R = ideal gas constant = 82.05 cm^3 atm/mol K.

The mole fraction X_A can be determined from Equations B-2 and B-3 in Appendix B for given temperatures. For chloroform,

$X_A = 0.260$ (at 25 °C)

$X_A = 0.0363$ (at -14.5 °C).

The drop time of flight was determined in Appendix D. This parameter equals the amount of time available for solvent evaporation

$t = 8.37 \times 10^{-3}$ sec.

All of these parameter values can be applied to Equation C-7 to determine the size of a binder drop at the powder bed surface after evaporation. At 25 °C, the final drop diameter is

$D_{25} = 67\ \mu m$,

which corresponds to a 53% decrease in volume from the original (86.4 μm) size. If evaporation occurs at the wet bulb temperature, several of these parameters will be modestly different. If we approximate the material properties at the wet bulb temperature to be roughly the same as they are at room temperature, the wet bulb final drop diameter can easily be approximated with Equation C-7. At -14.5 °C, the drop diameter at the powder bed surface is

$$D_{-14.5} = 84\ \mu m,$$

which corresponds to an 8% decrease in volume.

Appendix D: Time to reach wet bulb temperature and drop time of flight

As mentioned in the text, solution of the time dependent heat and mass transfer equations is quite involved. Steady state evaporation temperature approximations simplify this calculation. In addition, the mass flux of binder that evaporates during delivery to the powder bed can be approximated as the ratio of the heating rate to the heat of vaporization or

$$N_A = \frac{m C_p \Delta T}{\lambda A t} \qquad \text{(D-1)}$$

where N_A = mass flux (g/cm^2 sec)

m = mass (g)

C_p = heat capacity (J/mol °C)

$\Delta T = T_o - T_{wb}$ (°C)

λ = latent heat of vaporization (J/mol)

A = drop surface area = πD^2 (cm^2)

t = time to reach T_{wb} (sec).

The time to reach the wet bulb temperature can be determined by rearranging Equation D-1

$$t = \frac{m C_p \Delta T}{\lambda A N_A} \qquad \text{(D-2)}$$

From the molar flux equations Appendix C (Equations C-3 and C-4), the mass flux is given by

$$N_A = \frac{Sh\ D_{AB}}{D} \bar{C}\ X_A\ M_s \qquad \text{(D-3)}$$

where Sh = Sherwood number

D_{AB} = diffusion coefficient (cm^2/sec)

C = average concentration (mol/cm^3)

X_A = mole fraction of solvent on drop surface

M_s = binder solvent molecular weight (g/mol)

D = binder drop diameter.

Equation D-2 can be rearranged using Equation D-3 and converting masses to diameters ($m = \pi D^3 \rho/6$) to yield

$$t = \frac{D^2 \rho\ C_p\ \Delta T}{6\lambda\ Sh\ D_{AB} \bar{C}\ X_A\ M_s} \qquad \text{(D-4)}$$

Sh, D_{AB}, C, X_A, and M_s are given in Appendix C. D was determined in Appendix A. ΔT, from the results in Appendix B, is 39.5 °C. The other parameters are

$\rho = 1.473\ g/cm^3$

$C_p = 109.96$ J/mol °C

$\lambda = 29{,}200$ J/mol.

The solution to Equation D-4 using these values gives a time to reach the wet bulb temperature of

$$t_{wb} = 2.08 \times 10^{-3} \text{ sec}$$

The drop time of flight is the distance travelled to the powder bed divided by the drop velocity or

$$t_{TOF} = x/v$$

where t_{TOF} = drop time of flight

x = distance from printhead to powder bed (cm)

v = drop velocity (cm/sec).

The distance to the powder bed from the printhead is 3 centimeters. The drop velocity was determined in Appendix A and is 358.56 cm/sec. The drop time of flight is

$$t_{TOF} = 8.37 \times 10^{-3} \text{ sec.}$$

The time to reach the wet bulb temperature is 25% of the time of flight time. The difference is not great enough to say that binder drop evaporation can be approximated as completely occurring at either room temperature or the wet bulb temperature.

REFERENCES

1. Vacanti, C.A., Cima, L.G., Ratkowski, D., Upton, J., and Vacanti, J.P., "Tissue engineering of new cartilage in the shape of a human ear using specially configured polymers seeded with chondrocytes", in Tissue-Inducing Biomaterials, L.G. Cima, Editor. 1992, Materials Research Society: Pittsburgh. p.323-330.

2. Mikos, A.G., Thorsen, A.J., Czerwonka, L.A., Bao, Y., Langer, R., Winslow, D.N., and Vacanti, J.P., "Preparation and characterization of poly(L-lactic acid) foams". Polymer, 1994. **35**: p 1068-1077.

3. Cima, L.G., Vacanti, J.P., Vacanti, C., Ingber, D., Mooney, D., and Langer, R., "Tissue engineering by cell transplantation using biodegradable polymer substrates". Journal of Biomechanical Engineering, 1991. **113**: p.143-151.

4. Mikos, A.G., Sarakinos, G., Leite, S.M., Vacanti, J.P., and Langer, R., "Laminated three-dimensional biodegradable foams for use in tissue engineering". Biomaterials, 1993. **14**: p. 323-330.

5. Ratner, B.D., "Biomedical Applications of Synthetic Polymers" in The Synthesis, Characterization, Reactions, and Applications of Polymer, vol. 7, S.L. Aggarwal, Editor, from Comprehensive Polymer Science, G.Allen, and J.C. Berington, Editors. 1989 Pergamon Press: Oxford, p 201-247.

6. Halberstadt, C., Anderson, P., Bartel, R., Cohen, R., and Naughton, G., "Physiological cultured skin substitutes for wound healing", in Tissue-Inducing Biomaterials, L.G. Cima, Editor. 1992, Materials Research Society: Pittsburgh. p.323-330.

7. Ito, K., Fulisato, T., and Ikada, Y., "Implantation of cell-seeded biodegradable polymers for tissue reconstruction" in Tissue-Inducing Biomaterials, L.G. Cima, Editor. 1992, Materials Research Society: p 359-365.

8. Hollinger, J.O., "Preliminary report on the osteogenic potential of a biodegradable copolymer of polylactide (PLA) and polyglycolide (PGA)". Journal of Biomedical Materials Research, 1983. **17**: p 71-82

9. Jacobs, P.F., Rapid Prototyping & Manufacturing: Fundamentals of Stereolithography. Society of Manufacturing Engineers, Dearborn, MI, 1992.

10. Burns, M. Automated fabrication: Improving productivity in manufacturing. Prentice Hall, Englewood Cliffs, NJ, 1993.

11. Lauder, A.J., M.S. thesis, Massachusetts Institute of Technology, 1992.

12. Sachs, E.M., Cima, M., Bredt, J., Curodeau, A., Fan, T., and Brancazio, D., "CAD-casting direct fabrication of ceramic shells and cores by three dimensional printing". Manufacturing Review, 1992. **5**: p. 117-126.

13. Sachs, E.M., Haggerty, J.S., Cima, M.J., and Williams, P.A., U.S. Patent #5,204055 1993.

14. Sachs, E.M., Cima, M., Williams, P., Brancazio, D., and Cornie, J., "Three dimensional printing: rapid tooling and prototypes directly from a CAD model". Journal of Engineering for Industry, 1992. **114**: p. 481-487.

15. Bredt, J., Ph.D. thesis, Massachusetts Institute of Technology, 1995.

16. Giordano, R.A., Wu, B.M., Borland, S.W., Cima, L.G., Sachs, E.M., and Cima, M.J., "Mechanical properties of dense polylactic acid structures fabricated by three dimensional printing". submitted to Biomaterials, 1994.

17. Savart, F., "Memoire sur la constitution des veines liquides lancees par des orifices circulaires en mince paroi" . Annals of Chimica Physica, 1833. **53**: p. 337-345.

18. Rayleigh, F.R.S., "On the instability of jets". Proceeding of the London Mathematical Society, 1878. **10** (4): p. 4-13.

19. Bruce, C.A., "Dependence of ink jet dynamics on fluid characteristics". IBM Journal of Research and Development, 1976. **20**: p. 258-270.

20. Richardson, E.G., "Mechanism of the disruption of liquid jets". Applied Scientific Research, Section A, 1954. **3**: p. 374-380.

21. Yuen, M., "Non-linear capillary instability of a liquid jet". Journal of Fluid Mechanics, 1968. **33**: p.151-159.

22. Heinzl, J. and Hertz, C.H., "Ink-Jet Printing". Advances in electronics and electron physics, 1985. **65:** p. 91-171.

23. Goldin, M., Yerushalmi, J., Pfeffer, R., and Shinnar, R., "Breakup of a laminar capillary jet of a viscoelastic fluid". Journal of Fluid Mechanics, 1969. **38**: p. 689-711.

24. Sweet, R.G., "High frequency recording with electrostatically deflected ink jets". Stanford Electron Laboratory Technical Report # 1722-1. Stanford University, 1964.

THESIS PROCESSING SLIP

FIXED FIELD: ill. _____ name _____

index _____ biblio _____

► COPIES: (Archives) Aero Dewey Eng Hum

Lindgren Music Rotch (Science)

TITLE VARIES: ► ☐ _____

NAME VARIES: ► ☒ William

IMPRINT: (COPYRIGHT) _____

► COLLATION: 141 l

► ADD. DEGREE: _____ ► DEPT.: _____

SUPERVISORS: _____

NOTES:

cat'r: date:

page: 3114

► DEPT: Chem. Eng.

► YEAR: 1995 ► DEGREE: M.S.

► NAME: BORLAND, Scott W.